Masters thesis

Topological Localized States in a Delayed Adler Equation

Submitted by

Florian Eckel

September 14, 2020

First examiner
PD. Dr. Svetlana V. Gurevich

Second examiner
Prof. Dr. Julien J. P. Javaloyes

Westfälische Wilhelms-Universität Münster
Fachbereich Physik
Institut für Theoretische Physik

Contents

1. Introduction

Localized structures (LSs) are objects which are densely concentrated on a background which might be homogenous or periodic in space or time [GA12]. They are widely observed in nature, science and engineering such as water waves [Her13], current densities in semiconductors [Nie+92], in chemical reactions [Kos+18], in neuronal activities [EB31] and in vegetation patterns [Mer+04]. LSs often appear in form of fronts or pulses, e.g. pulses in the intensity of light beams in optics [Sei+20].
Observations of LSs can be modelled by differential equations which describe the dynamics of the corresponding complex system. Despite other, partial differential equations (PDEs) and delayed differential equations (DDEs) are distinguished. Spatially extended systems are often described by PDEs, as the Turing model which explains different pattern formations on the skin of animals [Lep04]. DDEs, however, model systems with time delayed feedback, e.g. population models [Cla76]. Complex systems might also be modelled by a combination of these types of differential equations as in the reaction-diffusion system analyzed in [Gur13]. Besides the obvious differences between PDEs and DDEs, they are investigated in similar frameworks. Nevertheless, there is an important difference between them with respect to the symmetry. Since spatial systems often describe position space, they adapt the left-right and up-down symmetry, for example of a medium. In contrast to that, time does not necessarily possess a parity symmetry resulting in a symmetry breaking in several temporal systems. The parity symmetry might be broken due to an excitation which occurs for example as a response to a perturbation as observed in nervous systems, e.g. [EB31]. The symmetry breaking leads to a wider range of possible phenomena in temporal systems, e.g. depletion of the active material gain that only recovers on a given time scale as discussed in [Jav+16], making them very interesting. In this thesis an optical temporal system which produces LSs with a broken parity symmetry is analyzed.
LSs can be interpreted as dissipative solitons, which are observed in non-conservative systems, in the weak dissipative limit. Dissipative solitons obtain their stability from the balance of gain and loss – especially gain and loss of an electric field for optical systems as in [VT05] – and the balance between dispersion and nonlinearity. The stability of classical solitons, however, is determined by the balance between dispersion and nonlinearity only. The LSs in the system analyzed in this thesis are called kinks or Φ-bits. In contrast to other common LSs in optical systems, this study is not interested in LSs in the intensity which exist independent of each other, but in kinks that are intrinsically phase bits in the phase space. These LSs are experimentally observed in [Gar+15] and consist of 2π phase rotations. They obtain their stability, a certain robustness and formability from the topology of the phase space of the nonlinear system, especially the 2π-periodicity.
LSs in optics are already investigated with the motivation of an application as regenerative memories, e.g. [Rom+16], since delayed self-feedback allows the storage of infor-

mation in an optical cavity. Because optical communication networks already depend strongly on semiconductor devices, the existence of LSs in semiconductor lasers is of special interest. The additional robustness of the investigated kinks due to the topology of the phase space is an important property regarding possible applications in this field. A DDE, which describes the time evolution of the phase of an injection locked semiconductor laser with delayed self-feedback, is derived in [Gar+15]. This equation is called the Delayed Adler Equation (DAE). The steady states and periodic solutions consisting of LSs in the phase are analyzed in [Mun19] and [MJG20]. Especially the emergence of the periodic orbits from the steady states is investigated. This study is interested in the interaction between kinks in one cavity and in how the position of the kinks inside one cavity can be controlled, since it is a major requirement for possible applications in optical communication networks.
A reduced model, called the equation of motion (EOM), is based on the interactions between LSs. It is derived in [Mun19] and [MJG20] and describes the evolution of positions of LSs in a temporal cavity with less complex ordinary differential equations. Therefore, direct numerical simulations (DNSs) of the EOM are superior in terms of computational costs to DNSs of the DAE.
After an overview of the theoretical background, which is provided in chapter 2, this thesis is organized as follows: In chapter 3, a new way of determining the necessary values of the reduced model is investigated in order to reduce mismatches between simulations of the DAE and the EOM. The explicit model for periodic solutions containing two LSs and necessary properties are derived in section 3.1.1. An overview of the simulations used for the determination of the necessary values is given in section 3.1.2 and these values are determined in section 3.1.3. The output of DNSs of the EOM with these values are compared to DNSs of the DAE in section 3.1.4. In section 3.2 the distances, which are observed between the LSs after the transient, are investigated with respect to the delay time. Chapter 4 focuses on the control over the positions of the LSs in a cavity. Therefore, an additional periodic potential is added to the DAE. Synchronization between the periodic potential and the periodic solutions containing multiple 2π-rotations is observed experimentally in [Gar+17] for the corresponding PDE. Synchronization between LSs and an external periodic forcing is also found in other optical delayed systems, e.g. [Cam+16]. The theoretical and numerical analysis of the impact of the periodic potential on the periodic solutions of the DAE containing a LS is conducted in this chapter. Thus, the extended equation is presented in section 4.1. The impact of the periodic potential on the steady states which are calculated in [Mun19] and [MJG20] is explored in section 4.2. The conditions of the existence of LSs in the DAE with periodic potential are investigated in section 4.3. Section 4.4 discusses the phenomena of synchronization between one LS and the periodic potential at a specific parameter set while section 4.5 compares the impact of different parameter sets on the region of synchronization. The results of the periodic solutions containing one LS are extended to solutions containing two LSs in section 4.6. An overall conclusion and outlook is given in chapter 5.

2. Theoretical Background

This chapter contains a theoretical background on several topics necessary for this thesis. The given definitions are used throughout the thesis. The main equation of this study, the DAE reads

$$\frac{d\theta\left(t\right)}{dt} = \Delta - \sin\left(\theta\left(t\right)\right) + \chi \sin\left(\theta\left(t-\tau\right) - \theta\left(t\right) - \psi\right) \coloneqq f(\theta, \theta\left(t-\tau\right)) \tag{2.1}$$

and is derived in section 2.6.1. It is a scalar nonlinear DDE for the evolution of the phase $\theta(t)$ in time with the three control parameters detuning Δ, feedback strength χ and additional phase ψ, which is added to the feedback, and fixed single delay of length τ.

2.1. Differential Equations as Descriptions of the Dynamics of Complex Systems

Time evolutions of a wide variety of systems in nature, science and engineering are often described via (deterministic) differential equations, which define the dynamics of the corresponding systems. In most cases, it is defined by a set of differential equations and an initial condition. If, as in this thesis, the initial condition gives the initial state or states of a system at the starting point in time, it is an initial value problem (IVP). A differential equation involves a function an its derivatives. The highest derivative determines the order of the differential equation and the number of equations in a set defines the dimension of the system. However, for the sake of this thesis, considering a system with one dimension is sufficient, since the subject of this thesis is a one-dimensional delayed system with one delay term. The system is described by an IVP of a DDE. For a better understanding, first, ordinary differential equations (ODEs) and partial differential equations (PDEs) are introduced and next, DDEs are presented:

ODE An ODE of order N for an unknown quantity $z(t)$ in one independent variable t has the general form

$$f\left(z(t), \frac{dz(t)}{dt}, ..., \frac{d^{N-1}z(t)}{dt^{N-1}}, \frac{d^{N}z(t)}{dt^{N}}\right) = 0. \tag{2.2}$$

The initial condition $z(t_0)$ is the state of the system at a given time t_0. It is the only degree of freedom besides a change in any control parameters of the equation. Therefore, all information needed for the prediction of the dynamics of a system described by an IVP of an ODE rely on one initial value $z(t_0)$. Each of the derivatives $\frac{d^i z(t)}{dt^i}$ where $i = 1, ..., N$ depends on the independent variable t only. Usually, the time evolution of the dynamics of a system calculated via DNSs are visualized in a 2D plot of $z(t)$ against t. For further details on the analysis of ODEs see [Str07].

PDE A one-dimensional PDE of order N in time and order M in space for an unknown quantity $z(t,x)$ in multiple variables – here time t and position $x \in [0,L]$ in the (periodical) domain of length L – reads

$$f\left(t, x, z(t,x), \frac{\partial z(t,x)}{\partial t}, \frac{\partial z(t,x)}{\partial x}, \frac{\partial^2 z(t,x)}{\partial t^2}, \frac{\partial^2 z(t,x)}{\partial t \partial x}, \frac{\partial^2 z(t,x)}{\partial^2 x}, ..., \frac{\partial^N z(t,x)}{\partial t^N}, \frac{\partial^M z(t,x)}{\partial x^M}\right) = 0. \tag{2.3}$$

In contrast to an ODE, it contains the partial spatial derivatives up to order M and boundary conditions are necessary, e.g. periodic boundary conditions where $z(t, x = 0) = z(t, x = L)$. The initial condition $z(t_0, x)$ where $x \in [0, L]$ is again the state of the system at a given time t_0. However, a PDE has infinitely many degrees of freedom contrary to an ODE. Those arise from different values $z(t_0, x)$ at each of the positions $x \in [0, L]$ in the domain at the time t_0. Hence, the dynamics of a system described by an IVP of a PDE is defined by infinite number of values $z(t_0, x)$ on a domain $x \in [0, L]$. The calculated time evolution of such a system is often presented in a so-called space-time plot. It is a 2D color-plot with the time t and the position x as axes. The value of $z(t, x)$ is displayed with a color-scale. PDEs are further explained in [Tol20].

DDE In general, a DDE depends on states of the system at l previous times $t - \tau_1, ..., t - \tau_l$. It might also depend on the derivatives at those times. In this case, the type of equation is called a neutral DDE and reads

$$f\left(z(t), z(t-\tau_1), ..., z(t-\tau_l), \frac{dz(t)}{dt}, \frac{dz(t-\tau_1)}{dt}, ..., \frac{dz(t-\tau_l)}{dt}, ..., \frac{d^N z(t)}{dt^N}, \frac{d^N z(t-\tau_1)}{dt^N}, ..., \frac{d^N z(t-\tau_l)}{dt^N}\right) = 0. \tag{2.4}$$

An analysis of DDEs is given in [JQ13]. However, for the investigated system the general form reduces to a first order ($N = 1$) DDE depending on one previous state $z(t - \tau)$ for an unknown function without any spatial component $z(t)$, which may be written as

$$f\left(z(t), z(t-\tau), \frac{dz(t)}{dt}\right) = 0. \tag{2.5}$$

The main difference to the previously introduced kinds of differential equations is that a DDE does not solely depend on the present state – as an ODE or a PDE – but also on previous states at time $t-\tau$. The delay time is given by τ. Thus, $z(t)$ for $t \in]t_0 - \tau, t_0]$ is required for the calculation of an IVP of a DDE. Hence, the values at the time $\tilde{t} \in]t-\tau, t]$ need to be stored during the calculation leading to a temporal domain of length τ. Therefore, the initial condition has infinitely many degrees of freedom, as for the PDE. In fact, a spatial domain of length L used in a PDE has similarities to a temporal domain of length $\tilde{T}$ used in a DDE. Hence, the dynamics of a delayed system can be visualized in

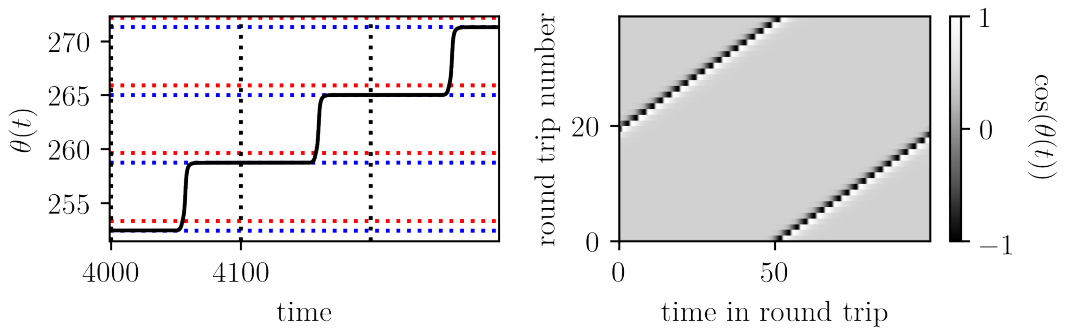

Figure 2.1: Time evolution of a stable solution containing one LS of the DAE, given in eq. (2.1), at the parameter set $\Delta = 1.2$, $\chi = 0.3$, $\psi = 1.4$, $\tau = 100$ and $\epsilon = 0$. (Left) An extract of the time trace and (right) the whole time evolution in the co-moving reference frame with respect to a round trip length of $\tilde{T} = \tau$ is shown. For a video which illustrates how the co-moving reference frame is obtained see `https://uni-muenster.sciebo.de/s/H8D4LXXKobFZpUt`. The blue and red lines highlight the stable and unstable, respectively. These are introduced in detail in section 2.6.2.

a so-called co-moving reference frame which is the equivalent representation to a space-time plot of a dynamics described by a PDE. The co-moving reference frame of the time evolution calculated in the interval $[t_0, t_{\text{end}}]$ is obtained by splitting up the calculated values in intervals of length $\tilde{T}$, also called the folding parameter, in time. $R \in \mathbb{N}$ intervals are obtained: $[t_0 + r\tilde{T}, t_0 + (r+1)\tilde{T}[$ for $r = 0, 1, ..., R-1$ and $[t_0 + R\tilde{T}, t_{\text{end}}]$ with $\frac{t_{\text{end}} - t_0}{\tilde{T}} - 1 < R \leq \frac{t_{\text{end}} - t_0}{\tilde{T}}$. The axes of the 2D color-plot are the interval number $r = 0, 1, ..., R$ also called the number of round trips and the time in a round trip $[0, \tilde{T}]$ which corresponds to the r-th interval. $z(t) = z(\text{div}(t - t_0, \tilde{T}), \text{mod}(t - t_0, \tilde{T}))$ is displayed via a color-scale. A video which shows the creation of a co-moving reference frame of a time series is provided at `https://uni-muenster.sciebo.de/s/H8D4LXXKobFZpUt`. The final frame of the video is presented in fig. 2.1. It shows the shape of the LSs observed in dynamics which are created by the DAE, which is derived in section 2.6.1. Such LSs are the main subject of this study. The co-moving reference frame indicates that the solution is not periodic with the period τ, which is the length of a round trip, since the LSs drifts. However, a period $\tilde{T} = T > \tau$ can be found such that $\tilde{T} = T$ corresponds to the period of this solution. In general, periodic solutions containing LSs of the investigated systems have a period $T > \tau$. Hence, $\tilde{T} = \tau$ is not necessarily required and $\tilde{T} \neq \tau$ might give a more useful representation.

2.2. Concept of Excitability

Excitability is observed in a variety of complex systems from solids [Pin18] to nerve systems [EB31]. In general, an excitation is a significant response of a system to a relatively small perturbation which overcomes a certain well-defined threshold. Therefore, it is often found as an amplification of a perturbation above a specific strength. A perturbation

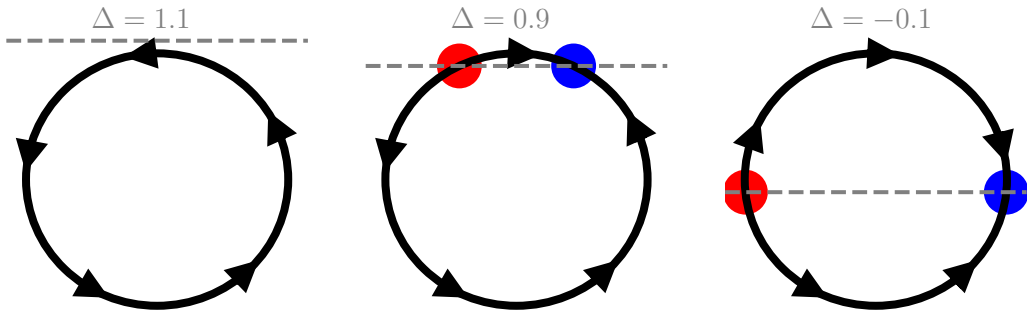

(a) $\Delta = 1.1$ **(b)** $\Delta = 0.9$ **(c)** $\Delta = -0.1$

Figure 2.2: Flow diagram of the phase θ given by eq. (2.6) for different values of Δ on a circle. The blue and the red dot illustrate stable and unstable fixed points, respectively. (a) corresponds to $\Delta = 1.1$ leading to no fixed points, while (b) and (c) represent $\Delta = 0.9$ and $\Delta = 0.1$ where fixed points exist.

below this threshold leads to a response of the system in the same order of magnitude as the perturbation. If the perturbation overcomes the threshold the system will be in its excited state before it returns to the original state. The time of the excitation is called refractory period. The system cannot be excited again by a perturbation above the threshold as long as the system is in its excited state. An example for an excitable system is given by systems described by the Adler Equation [Adl46]

$$\frac{d\theta}{dt} = \Delta - \sin(\theta)\,. \tag{2.6}$$

It describes the phase difference θ between two weakly coupled oscillators with a detuning Δ of the frequencies. In general, the phase evolution of multiple identical oscillators is described by the Kuramoto model [Kur75] which is given in eq. (2.7). Hence, eq. (2.6) can also be obtained from the Kuramoto model.
Steady states of the Adler equation are found for $\Delta \in [-1, 1]$ because values of θ exist which meet the condition $\frac{d\theta}{dt} = 0$. The steady states correspond to a solution where the phase difference between both oscillators is fixed. The flow diagram of the phase θ on a circle is illustrated in fig. 2.2. The circle already indicates the 2π-periodicity of the phase space. The stable and unstable steady states of the system are highlighted by blue and red dots, respectively. They are connected by two heteroclinic orbits if both steady states exists. The arrows indicate the direction that the phase θ is attracted to. A small perturbation of the stable steady state in one of the two directions leads to a direct return to the steady state. The system is not excited. In contrast to that, a perturbation which kicks the phase above the unstable steady state results in an orbit which exhibits the whole phase space. This orbit is the response of the system which is large compared to the perturbation needed for an excitation. The relaxation of the orbit takes significantly longer than a response of the perturbation below the threshold of excitation. Another

perturbation of the magnitude of the threshold, which is applied to the system during the refractory period, does not lead to another excitation of the system in general. The necessary threshold for a perturbation which results in an excitation corresponds to the distance between the stable and unstable steady state. It is smaller, the closer the fixed points are together. The steady states annihilate for the critical values $\Delta = \pm 1$ leading to a homoclinic orbit.

2.3. Arnold Tongue and Synchronization

The first mentioning of synchronization dates back to Huygens' in 1665 who observed synchronization between two clocks hanging on the wall [OM15]. Since then it has been widely observed and used in applications, for example in radio communication systems where a weak but precise signal stabilizes the frequency of a generator. The basic model where synchronization is observed is called the Kuramoto model [Kur75] which reads

$$\frac{d\theta_s}{dt} = \omega_s + \frac{\nu}{N} \sum_r \sin\left(\theta_r - \theta_s\right). \tag{2.7}$$

It describes the evolution of the phase θ of N equally coupled oscillators of intrinsic natural frequency ω. The coupling is described by the coupling constant ν. For $N = 1$, the Adler equation, given in eq. (2.6), is obtained. Synchronization is also observed in systems with external periodic forcing, which is used to control the dynamics of the systems, e.g. in the forced self-sustained Duffing oscillator [ZA14]. A detailed introduction to synchronization is provided in [PRK01].
This thesis analyzes the impact of an external periodic potential on the behavior of LSs which are observed in a system described by the DAE with periodic potential. In section 2.8 it is explained that a setup which is described by the investigated equation may also be regarded as multiple nested quasi-harmonic oscillators. Quasi-harmonic – also called quasilinear – means that the oscillation of the solution on the limit cycle or the attractor of the system is close to the form of a sine wave. At different stages of the nesting, the system corresponds to a quasilinear oscillator which exhibits periodical external forcing. Therefore, the general case of a periodical force applied to a quasilinear oscillator is introduced:
The harmonic oscillation of a quasilinear oscillator is given by

$$z(t) = Z_0 \sin\left(\omega_0 t + \phi_0\right) \tag{2.8}$$

with amplitude Z_0, natural frequency ω_0 and offset of the phase ϕ_0. The periodic potential

$$\varphi(t) = A \cos\left(\omega t\right) \tag{2.9}$$

with amplitude A and frequency ω leads to an external force that varies as $F(t) = A\omega \sin(\omega t) = \tilde{A} \sin(\omega t)$. The force does not change the amplitude Z_0 of the oscillation of the quasilinear oscillator, since the orbit corresponds to an attracting orbit where no point of the phase is exclusive. Thus, the systems response to small perturbations in change of the amplitude is the return of the amplitude to the attracting orbit. Therefore, the interest rests on the impact of the force on the phase which is 2π periodic. The phase space may be visualized by a circle which is a frame where the periodicity is implemented. The phase of positions z may be regarded as points on the circle and the phase of forces F as arrows from the origin to those phase points on the circle indicating the direction of the action. The phase of the force rotates with frequency ω in a resting frame. However, a rotating frame of frequency ω is advantageous for this problem and therefore used. In a rotating frame with frequency ω, the phase is constant. Thus, the force acts in a constant direction. In this rotating frame, however, the phase point of the oscillation rotates with a frequency $\omega_0 - \omega$. It can be found that the phase difference between the oscillation of the oscillator and the external force is defined as

$$\phi(t) = \omega_0 t + \phi_0 - \omega t = (\omega_0 - \omega)\, t + \phi_0. \tag{2.10}$$

The phase point of the oscillation rotates clockwise for $\omega_0 > \omega$ and counterclockwise for $\omega_0 < \omega$. Over time it can be found at every position of the circle as long as $\omega_0 \neq \omega$. For $\omega_0 = \omega$ it does not rotate and remains at a constant position.
As already determined, the force acts in a constant direction. An object which can move freely on a circle and on which a force in a constant direction is acting on may be found at rest at two positions of the circle, exactly where the direction of the force is orthogonal to the circle. Those two positions on the circle are identified as stable and unstable fixed points. The stable fixed point is at the position which is reobtained by the object after a perturbation. Therefore, the force drags the phase point towards the position which corresponds to the stable fixed point, independent of the position of the phase point on the circle.
The previously mentioned free object which moves on the circle is identified with the phase point of the oscillation. Additionally, it gets the property of the intrinsic oscillation of the frequency $\omega_0 - \omega$ resulting from the quasilinear oscillator. In contrast to the force which drags the object towards the stable fixed point, this oscillation drags the object around the circle for $\omega_0 \neq \omega$. This indicates two qualitatively different behaviors depending on which of the two impacts predominates.
If the force overbalances the intrinsic oscillation, the phase point of the oscillation in the rotating reference frame of frequency ω will remain at a constant position at the stable fixed point. Therefore, the frequency of this phase point corresponds to the frequency of this rotating frame ω and hence to the frequency of the force. Although, the intrinsic oscillation for the phase point given by the quasilinear oscillator is $\omega_0 \neq \omega$. The external periodic force locks the frequency of the oscillation and synchronizes the oscillation to

itself.
If the intrinsic oscillation outweighs the force, the phase point of the oscillation in the rotating reference frame of the frequency ω will move around the circle at a non uniform velocity. The velocity increases at the part of the circle where the force supports the direction of the motion and it decreases at the parts where it counteracts the intrinsic oscillation.
The impact of the force scales with its amplitude, whereas the impact of the intrinsic oscillation scales with the phase difference $\omega_0 - \omega$. The region of synchronization at a constant amplitude of the force depends on the detuning of the frequencies $\omega_0 - \omega$. If the detuning exceeds a certain threshold, no synchronization between external force and oscillation will be found. In general, the threshold increases for an increasing amplitude of the external periodic force. The region of synchronization in the plane of the amplitude A and the frequency ω of the external potential is called Arnold tongue.

2.4. Theoretical Analysis of DDEs

DDEs in general are introduced in section 2.1. In the following, the theoretical analysis of first order DDEs with one delay is explained. Therefore, eq. (2.5) is rewritten as

$$\frac{dz(t)}{dt} = f\left(z(t), z(t-\tau)\right). \tag{2.11}$$

2.4.1. Steady States

A steady state z_{st} is defined as a state of a system which remains stationary over time. Mathematically speaking, steady states match

$$z(t) = z_{st} \quad \forall t \tag{2.12}$$

This leads to the conditions

$$f(z_{st}, z_{st}) = 0 \tag{2.13}$$

and

$$z\left(t-\tau\right) = z(t) = z_{st} \quad \forall t \tag{2.14}$$

for the determination of steady states.

Linear Stability Analysis The stability of steady states is calculated via a linearization of the system. Therefore, the impact of a small perturbation $\varepsilon \ll 1$ on the steady state z_{st} is investigated. It is assumed that the perturbed steady state $z(t=0) = z_{st} + \varepsilon$

evolves as

$$z(t) = z_{st} + \varepsilon \exp(\lambda t). \tag{2.15}$$

This is a superposition of the non-evolving steady state and the exponentially growing perturbation with the exponent $\lambda \in \mathbb{C}$. Hence, the stability of the steady state is determined by λ, the so-called Lyapunov exponent. The perturbation decreases exponentially for $\Re(\lambda) < 0$, indicating a stable steady state. An exponentially growing perturbation as for $\Re(\lambda) > 0$ indicates an unstable steady state.
Inserting eq. (2.15) into eq. (2.11) and linearizing in ε leads to the eigenvalue problem

$$\lambda\varepsilon \exp(\lambda t) = \frac{\partial f\left(z(t), z(t-\tau)\right)}{\partial z(t)} \varepsilon \exp(\lambda t) + \frac{\partial f\left(z(t), z(t-\tau)\right)}{\partial z(t-\tau)} \varepsilon \exp\left(\lambda(t-\tau)\right). \tag{2.16}$$

The exponential growth rate λ is the eigenvalue of this problem. Rearranging the eigenvalue problem by introducing the constants A and B results in the so-called characteristic equation

$$\Leftrightarrow \lambda = A + B \exp\left(-\lambda\tau\right) \tag{2.17}$$

$$\text{where} \quad A = \left[\frac{\partial f\left(z(t), z(t-\tau)\right)}{\partial z(t)}\right]_{z_{st}} \tag{2.18}$$

$$\text{and} \quad B = \left[\frac{\partial f\left(z(t), z(t-\tau)\right)}{\partial z(t-\tau)}\right]_{z_{st}}. \tag{2.19}$$

Note that A and B are scalar numbers for a scalar DDE of first order. Equation (2.17) is not solvable analytically due to the transcendental character of this equation. Nevertheless, rewriting it results in a known structure:

$$\begin{aligned} \Leftrightarrow & \tau(\lambda - A) \exp\left(\lambda\tau\right) \exp\left(A - A\right) && = \tau B \\ \Leftrightarrow & h \exp\left(h\right) && = \tau B \exp\left(-A\right) \quad \text{where} \quad h = \tau(\lambda - A). \end{aligned} \tag{2.20}$$

These are implicit Lambert W functions which are defined as any function $W(H) = h$ which satisfies

$$W(H) \exp\left(W(H)\right) = H. \tag{2.21}$$

They are introduced in [YNU10]. It is a complex valued function with complex argument H. The inverse function $W^{-1}(h) = H$ reads

$$h \exp\left(h\right) = W^{-1}(h) \tag{2.22}$$

and is not injective. Therefore, $W(H)$ has multiple, in particular, infinitely many solutions. Each of the solutions is denoted as a branch $W_n(H)$ and cannot be presented in elemental functions. However, they can be calculated numerically. For a detailed

introduction see [YNU10].
Inserting the branches of the inverse Lambert W functions eq. (2.22) into eq. (2.20) leads to an infinite number of discrete solutions of the eigenvalue problem in eq. (2.17):

$$\lambda_n = \frac{1}{\tau}\left(A\tau + W_n\left(B\tau \exp\left(-A\tau\right)\right)\right). \tag{2.23}$$

The spectrum on which those eigenvalues lie is called pseudo-continuous spectrum.

Long Delay Limit Splitting up the complex eigenvalues into the form $\lambda = \frac{\alpha}{\tau} + i\beta$ which divides the real and the imaginary part $\frac{\alpha}{\tau} \in \mathbb{R}$ and $\beta \in \mathbb{R}$ respectively and inserting it into eq. (2.17) leads to an approximation of the eigenvalues for long delays:

$$\begin{aligned} B\exp\left(-\alpha - i\beta\right) &= \frac{\alpha}{\tau} + i\beta - A \quad \mid \text{multiply both sides with c.c.} \\ \Rightarrow |B|^2 \exp\left(-2\alpha\right) &= \frac{\alpha^2}{\tau^2} + \frac{\alpha}{\tau}\left(-i\beta - A^* + i\beta - A\right) + |\beta|^2 + |A|^2 - i\beta\left(A - A^*\right) \end{aligned} \tag{2.24}$$

Neglecting all terms scaling with $\frac{1}{\tau^2}$ and $\frac{1}{\tau}$ for the long delay limit gives a relation between the real and the imaginary part of eigenvalues:

$$\begin{aligned} \Rightarrow \alpha &= \frac{1}{2}\ln\left(\frac{|B|^2}{|A|^2 + |\beta|^2 - 2\beta\Im(A)}\right) \\ \Rightarrow \alpha &= \frac{1}{2}\ln\left(\frac{|B|^2}{|A|^2 + |\beta|^2}\right) \quad \text{since} \quad \Im(A) = 0 \quad \text{for real valued DDEs} \end{aligned} \tag{2.25}$$

The discrete eigenvalues λ_n given in eq. (2.23) converge with increasing τ to the long delay limit which is given in eq. (2.25) and corresponds to a pseudo-continuous spectrum in the complex-plane. It is effectively filled with discrete eigenvalues for $\tau \to \infty$.

2.4.2. Periodic Solutions

Periodic solutions of period T are solutions which satisfy

$$z(t) = z(t+T). \tag{2.26}$$

Although steady states are periodic solutions by definition, usually time dependent solutions are meant by this expression. Note that solutions which satisfy eq. (2.26), also meet the same condition of nT where $n \in \mathbb{N}_+$. The lowest value of T which matches eq. (2.26) is called minimal period or in a short form just period.

First Return map Periodic solutions and their periodicity may be found by so-called first return or Poincare maps [Str07]. First, it is assured that the solution has settled on an attractor for several delay times τ and is not in a transition period by integrating the system for a sufficiently long time. The (theoretically) continuous time series $z(t)$ is

discretized in time by the definition of an useful measure I_n at specific point $n = 1, ..., N$. The measure depends on the system. Commonly used measures I_n are the value of the n-th maximum in $z(t)$ or the value $z(nT)$ at the n-th period, if a possible period is already determined from the time series $z(t)$. The first return map is produced by plotting the value of the $(n+1)$-th measure I_{n+1} against the value of the n-th measure I_n. A sufficient number of those (I_n, I_{n+1})-pairs should be taken into account. Two qualitatively different kinds of visualizations may occur. A quasi-continuous spectrum or quasi-filled plane of points and a number of discrete points. The first representation indicates that the solution is not periodic with the given period T. The latter identifies a periodic solution of period T. The number of discrete points determines the period of the orbit. Two discrete points indicate a period-2 orbit of period T, which corresponds to an period-1 orbit of period $2T$.

Determination of Stability The stability of a periodic solution is determined by the Floquet-multipliers which are the eigenvalues of a so-called monodromy matrix. The underlying concept is the Floquet theory [Mar18] which does not completely exist for linear DDEs, but the characteristic properties are defined in a similar matter [Jau17]. The theory is introduced for linear periodic differential systems first and finally transferred to a linear DDE. The stability of periodic solutions is defined via the response of the system to a small perturbation of the periodic orbit similar to steady states. Thus, it is determined by the linearized DDE as the stability of a fixed point in a nonlinear system is determined by the linearized system.
Let the $n \times n$-matrix $A(t)$, which is periodic $A(t) = A(t+T)$ with period T, define a linear first order ODE that reads

$$\frac{dy(t)}{dt} = A(t)y(t). \tag{2.27}$$

The linearly independent solutions of this system are the column vectors of the matrix $S(t, t_0)$. Therefore, $S(t, t_0)$ is the principle matrix solution of the system. It satisfies

$$\frac{dS(t, t_0)}{dt} = A(t)S(t, t_0). \tag{2.28}$$

As the system, it is periodic with the same period $S(t+T, t_0+T) = S(t, t_0)$. At some point in time $t = t_0$, $S(t_0, t_0)$ corresponds to the unity matrix $\mathbb{1}$. The time evolution of an arbitrary solution may be written as a linear combination of the linearly independent solutions stored in the principle matrix leading to

$$y(t + t_0) = S(t + t_0, t_0)y(t_0). \tag{2.29}$$

The evolution over one period T is described by $S(T, t_0)$, since

$$y(T + t_0) = S(T + t_0, t_0)y(t_0). \tag{2.30}$$

The evolution of a periodic solution $y_p(t) = y_p(t+T)$ which is perturbed by $y_\epsilon(t_0)$ at any time t_0 evolves as

$$\begin{aligned} y(T+t_0) &= y_p(T+t_0) + y_\epsilon(T+t_0) \\ &= S(T+t_0,t_0)\left(y_p(t_0) + y_\epsilon(t_0)\right) \\ &= S(T+t_0,t_0)y_p(t_0) + S(T+t_0,t_0)y_\epsilon(t_0) \qquad (2.31) \\ \Leftrightarrow y_\epsilon(T+t_0) &= S(T+t_0,t_0)y_\epsilon(t_0) \qquad (2.32) \end{aligned}$$

The evolution of the perturbation is given by the eigenvalue problem in eq. (2.32). Any perturbation $y_\epsilon(t_0)$ will decrease over one period T if the absolute values of all eigenvalues $|\mu_i|$ of $S(T+t_0,t_0)$ lie inside the unit circle ($|\mu_i| < 1 \quad \forall i \in \{1,...,n\}$). If the absolute value of one eigenvalue exceeds 1 ($\exists i \in \{1,...,n\} : |\mu_i| > 1$), a perturbation which grows over one period exists. The matrix

$$M(t_0) = S(T+t_0,t_0) \qquad (2.33)$$

is called monodromy matrix and its eigenvalues μ_i are the corresponding Floquet-multipliers. Both, the monodromy matrix and the Floquet-multipliers, are independent of the choice of t_0. A Floquet-multiplier $\mu_i = 1$ is called trivial Floquet-multiplier and is disregarded for the determination of the stability as it corresponds to the eigenvector of the periodic orbit leading to $y_p(t) = S(T+t,t_0)y_p(t_0) = y_p(T+t)$.
However, the principle matrix can be represented in terms of the $n \times n$-matrices $Q(t_0)$ and $P(t,t_0) = P(t+T,t_0)$ which is T-periodic

$$S(t,t_0) = P(t,t_0)\exp\left((t-t_0)\,Q\left(t_0\right)\right). \qquad (2.34)$$

If t_0 is chosen such that $S(t_0,t_0) = \mathbb{1}$, it will lead to $P(T+t_0,t_0) = P(t_0,t_0) = \mathbb{1}$. Hence, the monodromy matrix may written as

$$M(t_0) = S(T+t_0,t_0) = \exp\left(TQ\left(t_0\right)\right). \qquad (2.35)$$

The previously mentioned conditions for the Floquet-multipliers μ_i are equivalent to $\Re(\lambda_i) < 0 \quad \forall i \in \{1,...,n\}$ for stable and $\exists i \in \{1,...,n\} : \Re(\lambda_i) > 0$ for unstable periodic solutions. λ_i are the eigenvalues of $Q(t_0)$ and called the Lyapunov exponents. Those conditions are similar to the conditions for stability of steady states in section 2.4.1.
The dynamics of the system which is investigated in this thesis is described by a one-dimensional DDE. However, it has infinitely many degrees of freedom as explained in section 2.1. The dynamics can also be described by an infinite dimensional nonlinear ODE where an infinitely small discretized state vector with $0 < \delta_i = i\delta_1 < \delta_{i+1} = (i+1)\,\delta_1 < \tau \quad \forall i \in \mathbb{N}_+$ reads $y(t) = \left(z(t), z\left(t-\delta_1\right), z\left(t-\delta_2\right), ..., z\left(t-\tau\right)\right)^T$. The information of the values between t and $t-\tau$ is then stored in the state vectors, e.g. the first feedback which is the initial condition $y(t_0)$. In theory, the monodromy matrix

of the corresponding system is infinite dimensional leading to infinitely many Floquet-multipliers.
The corresponding n-dimensional discretized ODE to eq. (2.11) is given by

$$\frac{dy_i(t)}{dt} = g_i(y(t)) = \begin{cases} f\left(z_1(t), z_n(t)\right) & i = 1 \\ f\left(z_i(t), z_{i-1}(t)\right) & \forall i : 2 \leq i \leq n \end{cases} \tag{2.36}$$

with the same nonlinear function f and the nonlinear functions g_i which are similar to the function f. However, the linearized ODE reads

$$\frac{dy(t)}{dt} = J_g(t)y(t) \quad \text{where} \quad J_g(t) = \left(\frac{\partial g_i}{\partial y_j}(t)\right)_{i,j=1,\ldots,n} \tag{2.37}$$

where $J_g(t)$ is the Jacobian matrix. Finally, the form of eq. (2.27) is obtained.
Practically, the stability of a known periodic solution which is produced by the initial condition $y(t_0)$ is calculated via the IVP. For this, the partial derivative with respect to the initial condition $y(t_0) = y_0$ is applied to eq. (2.37) leading to

$$\frac{d}{dt}\frac{\partial y(t)}{\partial y_0} = J_g(t)\frac{\partial y(t)}{\partial y_0}. \tag{2.38}$$

$\frac{\partial y(t)}{\partial y_0} = S(t, t_0)$ is identified by comparing eq. (2.38) to eq. (2.28). Moreover, $\frac{\partial y(t_0)}{\partial y_0} = S(t_0, t_0) = \mathbb{1}$ is obtained, since $y(t_0) = y_0$. Therefore, the definition of the monodromy matrix $M(t_0) = S(T + t_0, t_0)$ in eq. (2.33) indicates that the monodromy matrix is calculated by solving the IVP

$$\frac{dS(t, t_0)}{dt} = J_g(t)S(t, t_0) \quad \text{where} \quad S(t_0, t_0) = \mathbb{1}. \tag{2.39}$$

The calculation of the monodromy matrix and its eigenvalues, the Floquet-multipliers, is implemented in `DDE-BIFTOOL`. This continuation tool for DDEs is used in this study. It is briefly introduced in section 2.5.2.

Types of Instabilities As the stability of periodic orbits depends on the Floquet-multipliers being inside the unit circle, instabilities of periodic solutions are encountered if one or more Floquet-multipliers leave the unit circle. Three different kinds of instabilities are distinguished and an overview is illustrated in fig. 2.3.
If one Floquet-multiplier leaves the unit circle at $\mu = 1$, as visualized in fig. 2.3 (a), it will lead to either a fold bifurcation of periodic orbits, called fold, or a flip bifurcation. Those bifurcations are distinguished in the bifurcation diagram. A fold bifurcation corresponds to a turning point in the bifurcation diagram at which the stability of a branch changes. Contrary to that, a branch changing its stability without a turning point indicates a flip bifurcation.

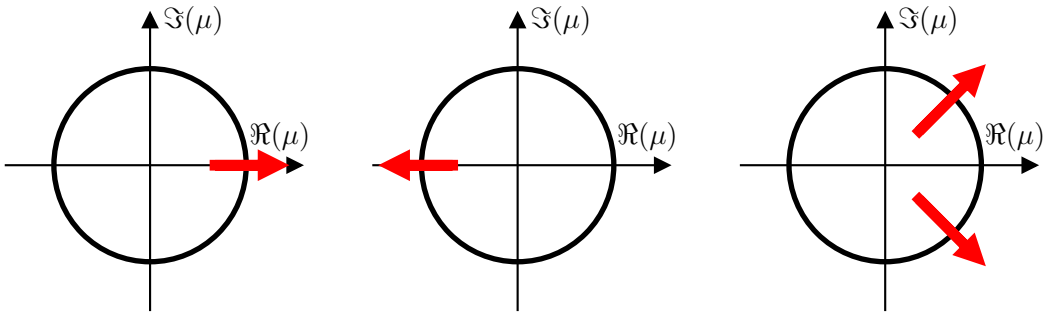

(a) Fold or flip bifurcation **(b)** Period doubling bifurcation **(c)** Torus bifurcation

Figure 2.3: Overview of different instabilities of a periodic solution with respect to Floquet-multipliers leaving the unit circle. (a) One Floquet-multiplier which is leaving the unit circle at $\mu = 1$ indicates a fold or a flip bifurcation. A fold bifurcation is found if no periodic solution emerges at the other side of the bifurcation point with respect to the continuation parameter. In contrast to that, a periodic solution exists at both sides of the bifurcation point at a flip bifurcation. (b) A period doubling bifurcation is indicated by one Floquet-multiplier leaving the unit circle at $\mu = -1$. (c) A pair of complex conjugated Floquet-multiplier leaving the unit circle leads to a torus bifurcation.

As the trivial Floquet-multiplier at $\mu = 1$ corresponds the periodic solution of period T, a Floquet-multiplier at $\mu = -1$ results in a periodic solution of doubled period $2T$ or a period-2 orbit of period T. That is the reason why the bifurcation, where a Floquet-multiplier leaves the unit circle at $\mu = -1$ as shown in fig. 2.3 (b), is called period doubling bifurcation. The Floquet-multiplier $\mu = -1$ results in a solution with doubled period because μ is an eigenvalue of the monodromy matrix. The matrix describes the time evolution over one period T. Hence, applying the monodromy matrix two times describes the time evolution over two periods $2T$, leading to the multiplication of the eigenvalues and resulting in $(-1)^2 = 1$. This indicates a periodic orbit as it is a trivial Floquet-multiplier of the squared monodromy matrix.
The behavior of the Floquet-multipliers of the third type of bifurcation is illustrated in fig. 2.3 (c). Two complex conjugated Floquet-multiplier leave the unit circle at the same point in parameter space resulting in a torus bifurcation. The name of the bifurcation is inherited from the arising attractor which forms a torus around the solution undergoing this bifurcation. The period of the oscillation on this attractor does not necessarily need to be connected to the period of the periodic orbit [Lan73]. In theory, a period doubling bifurcation is regarded as a special kind of torus bifurcation with a fixed ratio of the both periods leading to an attractor in a form of a Möbius strip.

2.5. Numerical Methods

Numerical methods are used for the investigation of DDEs since analytical methods have their limitations. Since the analyzed system is a continuous system, it needs to be discretized in order to apply numerical methods. A discretization is also performed in

section 2.4.2 to use the Floquet theory for the determination of the stability of periodic orbits of a DDE. As already mentioned before, the Floquet-multipliers are calculated with a numerical tool called `DDE-BIFTOOL` which makes a discretization necessary in any case. The theoretically infinite number of degrees of freedom of a DDE, as explained in section 2.1, is reduced to the number of points used for the sampling of one feedback of length τ.
Two different numerical tools are used throughout this study. Time series of the dynamics are calculated via DNSs. Continuations of periodic solutions and bifurcations are performed with a continuation tool for DDEs called `DDE-BIFTOOL`. The position of a LS in a periodic solution is defined via the maximum of the derivative of the profile due to the shape of a kink which is illustrated in fig. 2.1. The positions of kinks in periodic solutions obtained via DNSs or continuations are determined with the same subroutine in order to obtain comparability. For the evaluation of the derivative, a running average over a certain interval of the profile is used.

2.5.1. Direct Numerical Simulation – DNS

Two different schemes, a Runge-Kutta-4 (RK4) and a semi-implicit (SIMP) scheme of second order are implemented in C. A RK4 scheme is of fourth (error) order in general. However, when adding noise, it reduces to second or first order depending on the implementation. Noise of a small amplitude ξ might prevent the solution to follow strange attractors which might occur due to numerical properties. Both methods are similar in input and output arguments. The SIMP scheme is used for DNSs performed for this thesis, as its computational costs, in particular the run time, are lower. The scheme and its derivation is provided in appendix A.1.
The DNS is calculated on an equidistant mesh. However, the number of mesh points used for DNS can be chosen greater than the number of sample points of the final output. Different ways of defining the initial condition are used. The initial condition is either determined from analytics or a result of a previous time simulation is used. In the first case, it is given by a superposition of a constant, which corresponds to the stable steady state, and LSs proportional to $\arctan\left(\exp\left(\sqrt{a(t-t_0)}\right)\right)$ where a is a constant to tune the analytical LSs to resemble proper LSs of the system, $t \in [-\tau, 0]$ and t_0 is the time of the LS in the feedback. Moreover, a periodic solution containing a LS calculated by `DDE-BIFTOOL` is used as an initial condition especially in cases where the LS calculated from the given function does not survive several round trips.
Time evolutions of the positions of the LSs, which are described by the ODE given in eq. (2.73), are calculated with `scipy.integrate.odeint`, which is a subroutine provided in the Python-package `SciPy` for the integration of ODEs. For the website and the documentation see [The20].

2.5.2. Continuation Tool DDE-BIFTOOL

In contrast to the simulation of one specific initial condition via DNS, (path-)continuation follows different kinds of solutions through parameter space. While DNSs provide stable solutions only, unstable solutions can also be computed in continuation tools. In general, steady states, periodic solutions and bifurcation points can be continued.
Continuation in parameter space of a solution z_0 which is found at the parameter set ν_0 assumes that another solution z_1 exists at a slightly different parameter set $\nu_1 = \nu_0 + \delta\nu$. It is expected that the solution z_1 differs slightly from z_0 and that this difference can be predicted by the change in the parameter set $\delta\nu$. Different methods are known to predict the next solution as the tangent prediction and the pseudo-arclength prediction. The latter has the advantage that it does not fail at turning points like fold bifurcations. After the new solution was predicted it must be corrected, as it needs to meet eq. (2.5). For that, the Newton algorithm can be used, for example. This procedure is repeated and step by step more solutions are calculated. They form a branch of solutions $z_i(\nu_i)$. An introduction to numerical continuation methods is provided in [AG12].
Common continuation tools are `AUTO-07P` (see [KD20]) for ODEs and PDEs, `pde2path` (see [UWR12]) for PDEs and `DDE-BIFTOOL` (see [ELR02] and [ELS01]) for DDEs. The 3.3.1 version of `DDE-BIFTOOL` is used as a continuation tool in this study since a DDE is investigated. It can be obtained from `http://ddebiftool.sourceforge.net/` and the manual is provided in [Sie+14]. For the theoretical background for computation of normal form coefficients see [Jan10] and for additional information about the normal form implementation for Hopf-related cases see [Wag14] and [Bos16]. Moreover, the extension `ddebiftool_extra_psol` is added as it implements the continuation of periodic orbits and the corresponding fold, period doubling and torus bifurcations.
`DDE-BIFTOOL` uses a pseudo-arclength continuation which uses secant approximations for tangents for the control of the parameters [Sie+14]. The profile of periodic solutions is represented by a piecewise polynomial of degree d on an adaptive mesh with N points. Which leads to $dN+1$ stored points due to the border. In this thesis, $d = 5$ and $N = 100$ is used resulting in 501 points per profile of a periodic solution. The stability of a periodic solution is determined via the calculation of the monodromy matrix and its eigenvalues, the Floquet-multipliers. The calculation of the stability of a solution is not included in the continuation of a solution as it time consuming. Further methods are implemented to determine the stability of the solution in a branch after the continuation. Bifurcation points are detected as solutions where a Lyapunov exponent or a Floquet-multiplier of periodic solutions changes their stability.

2.6. Delayed Adler Equation – DAE

The DDE which is investigated in this thesis is the DAE. It describes the dynamics of the phase of an injection locked semiconductor laser with a delayed feedback loop as it is presented in fig. 2.4. The slave laser is locked by the master laser. The beam of the

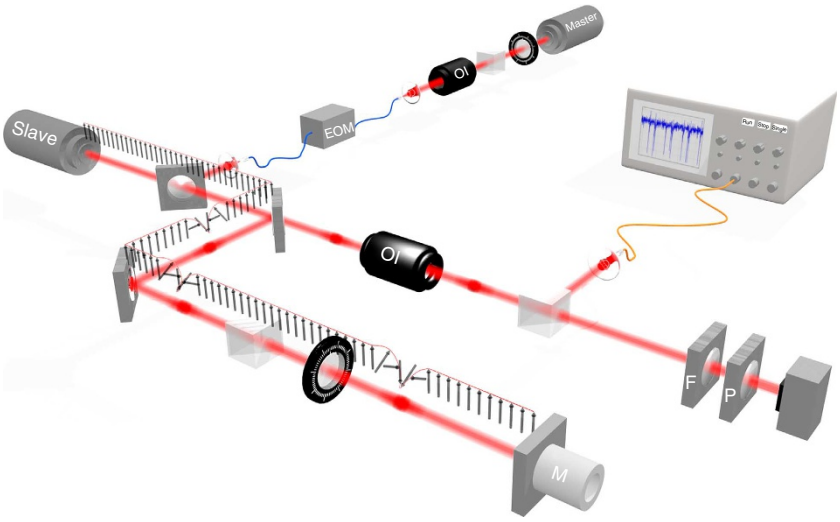

Figure 2.4: Experimental set-up of a semiconductor laser with coherent optical injection and delayed feedback loop [Gar+15]. The injection of the slave laser is produced by the master laser. The feedback loop returns the output of the slave laser to itself.

slave laser is split up into two parts. One is extracted to measure the phase in case of an experiment but has no further impact on the dynamics of the phase. The other part enters the feedback loop and is mirrored back to the slave laser after a specific delay.

2.6.1. Derivation from the Class A Laser Equation

In this section the DAE is derived from the class-A laser equation which is written in eq. (2.40). The derivation follows the derivation in the supplementary material of [Gar+15] and is provided since the theoretical investigation of the resulting equation is the main topic of this thesis.
The evolution of an optical field E in the shown experimental set-up illustrated in fig. 2.4 reads

$$\frac{dE}{dt} = (1 + i\alpha)\left(1 - |E|^2\right)E + Y + i\Delta E + \eta \exp\left(-i\Omega\right)E_\tau \tag{2.40}$$

with the linewidth enhancement factor α, the detuning Δ between the frequencies of the solitary laser and injected field, the field amplitude Y of the injection and the amplitude η and the phase Ω of the optical feedback $E_\tau = E(t - \tau)$ after the time delay τ. Note that the index τ denotes the delayed value of a variable. Rewriting the complex field as $E = \rho \exp\left(i\phi\right)$ results in a DDE for the amplitude ρ

$$\frac{d\rho}{dt} = \left(1 - \rho^2\right)\rho + Y\cos\left(\phi\right) + \eta\rho_\tau \cos\left(\Delta\phi - \Omega\right) \tag{2.41}$$

and the phase ϕ

$$\frac{d\phi}{dt} = \alpha\left(1-\rho^2\right) + \Delta + \frac{Y}{\rho}\sin\left(\phi\right) + \eta\frac{\rho_\tau}{\rho}\sin\left(\Delta\phi - \Omega\right). \tag{2.42}$$

A fast time-scale t_1 and a slow time-scale t_2 is introduced using a multiple time-scale expansion with a time separation factor ϵ:

$$\rho = 1 + \epsilon r\left(t_1, \epsilon t_2\right) + \mathcal{O}\left(\epsilon^2\right), \tag{2.43}$$

$$\phi = \phi\left(t_1, \epsilon t_2\right), \tag{2.44}$$

$$\frac{d}{dt} = \frac{\partial}{\partial t_1} + \epsilon\frac{\partial}{\partial t_2}. \tag{2.45}$$

Inserting the expansion in eq. (2.41) and eq. (2.42) and considering the first order in ϵ gives a set of equations:

$$\frac{\partial r}{\partial t_1} = -2r + Y\cos\left(\phi\right) + \eta\cos\left(\phi_\tau - \phi - \Omega\right) \tag{2.46}$$

$$\frac{\partial r}{\partial t_2} = 0 \tag{2.47}$$

$$\frac{\partial \phi}{\partial t_1} = 0 \tag{2.48}$$

$$\frac{\partial \phi}{\partial t_2} = -2\alpha r + \Delta - Y\sin\left(\phi\right) + \eta\sin\left(\phi_\tau - \phi - \Omega\right) \tag{2.49}$$

The amplitude is independent of the slow and the phase is independent of the fast time-scale in the first order in ϵ. The dynamics of the fast time-scale relaxes almost instantaneously to equilibrium with respect to the slow time-scale. Hence, the corresponding derivatives are set to $\frac{\partial r}{\partial t_1} = 0$, since the overall dynamics is governed by the motion of the slow time-scale. This technique is called adiabatic elimination [OP88] and results in the relation

$$2r = Y\cos\left(\phi\right) + \eta\cos\left(\phi_\tau - \phi - \Omega\right). \tag{2.50}$$

It is inserted in eq. (2.49) which leads to

$$\begin{aligned}\frac{1}{\sqrt{1+\alpha^2}}\frac{\partial \phi}{\partial t_2} = &-\frac{\alpha}{\sqrt{1+\alpha^2}}\left(Y\cos\left(\phi\right) + \eta\cos\left(\phi_\tau - \phi - \Omega\right)\right) \\ &+ \frac{\Delta}{\sqrt{1+\alpha^2}} - \frac{1}{\sqrt{1+\alpha^2}}\left(Y\sin\left(\phi\right) + \eta\sin\left(\phi_\tau - \phi - \Omega\right)\right).\end{aligned} \tag{2.51}$$

Defining $\sin\left(c\right) = \frac{\alpha}{\sqrt{1+\alpha^2}} < 1$ and $\cos\left(c\right) = \frac{1}{\sqrt{1+\alpha^2}} < 1$ gives $c = \arctan\left(\alpha\right)$. Additionally, rearranging eq. (2.51) by factorizing with respect to Y and η produces terms in the form

of $\sin(p)\cos(q) \pm \sin(q)\cos(p) = \sin(p \pm q)$ which lead to

$$\frac{1}{\sqrt{1+\alpha^2}}\frac{\partial\phi}{\partial t_2} = +\frac{\Delta}{\sqrt{1+\alpha^2}} - Y\sin(\phi + c) + \eta\sin(\phi_\tau - \phi - \Omega - c). \tag{2.52}$$

Finally, the time and the delay is rescaled by the factor $Y\sqrt{1+\alpha^2}$ and the detuning by $\frac{1}{Y\sqrt{1+\alpha^2}}$. Additionally, the phase $\theta = \phi + c = \phi + \arctan(\alpha)$, the feedback strength $\chi = \frac{\eta}{Y}$ and the feedback phase $\psi = \Omega + c = \phi + \arctan(\alpha)$ are redefined. The DAE

$$\frac{d\theta}{dt} = \Delta - \sin(\theta) + \chi\sin(\theta_\tau - \theta - \psi) := f(\theta, \theta_\tau) \tag{2.1 revisited}$$

is obtained. It is a scalar nonlinear DDE with the three control parameters detuning Δ, feedback strength χ and additional phase ψ, which is added to the feedback, and fixed single delay of length τ.

2.6.2. Analysis of Steady States

The previous theoretical study of the DAE investigated the steady states and their stability in [Mun19] which is published in [MJG20]. As the steady states build the background of periodic solutions containing LSs, the analysis is briefly reproduced. The theoretical background of the analysis is provided in section 2.4.1.
Applying the conditions for steady states given in eq. (2.13) and eq. (2.14) to eq. (2.1) leads to steady states for $\Delta - \chi\sin(\psi) \in [-1, 1]$:

$$\theta_s = \arcsin(\Delta - \chi\sin(\psi)) + 2\pi n \qquad n \in \mathbb{Z} \tag{2.53}$$

$$\theta_u = \pi - \arcsin(\Delta - \chi\sin(\psi)) + 2\pi n \qquad n \in \mathbb{Z}. \tag{2.54}$$

The steady states collide where $\theta_s = \theta_u$ leading to bifurcation points at the boundaries

$$\Delta_{sn}^{\pm} = \pm 1 + \chi\sin(\psi). \tag{2.55}$$

The stability of the steady states is determined by the Lyapunov exponents λ which have the form of eq. (2.17). Inserting eq. (2.1) into eq. (2.18) and eq. (2.19), respectively results in the coefficients

$$A = -\cos(\theta_{s,u}) - \chi\cos(\psi), \tag{2.56}$$

$$B = \chi\cos(\psi). \tag{2.57}$$

In case of no feedback $\chi = 0$, the DAE provided in eq. (2.1) reduces to the Adler Equation given in eq. (2.6) which is used for the explanation of excitability in section 2.2. The Lyapunov coefficients of the steady states reduce to

$$\lambda_{s,u} = -\cos(\theta_{s,u}). \tag{2.58}$$

Therefore, stable steady states $\theta_s \in [-\frac{\pi}{2} + 2\pi n, \frac{\pi}{2} + 2\pi n]$ and $\theta_u \in [\frac{\pi}{2} + 2\pi n, \frac{3\pi}{2} + 2\pi n]$ with $n \in \mathbb{Z}$ are identified as stable and unstable steady states, respectively. Thus, the bifurcation points where $\theta_s = \theta_u$ are identified as a saddle-node bifurcations for the Adler and for DAE. A schematic of the flow diagram for the Adler Equation with $|\Delta| < 1$ is given in fig. 2.2.
The stability of the steady states cannot be determined analytically in case of feedback $\chi \neq 0$. However, the relation eq. (2.25) which describes the quasi continuous spectrum is valid in the long delay limit. The maximum of the real part α of this equation is obtained for a vanishing imaginary part β. Thus, the instability of the steady states is obtained for $\alpha = 0$ and $\beta = 0$. The type of the occurring bifurcation corresponds to a saddle-node or a Andronov-Hopf bifurcation depending on the leading discrete eigenvalues λ which are real or a set of complex conjugates, respectively. The first kind results in the borders of stability given in eq. (2.55) and the latter kind in

$$\Delta_s^{\pm} = \pm\sqrt{1 - 4\chi^2 \cos^2(\psi)} + \chi \sin(\psi) \quad \cos(\psi) < 0 \tag{2.59}$$

$$\Delta_u^{\pm} = \pm\sqrt{1 - 4\chi^2 \cos^2(\psi)} + \chi \sin(\psi) \quad \cos(\psi) > 0. \tag{2.60}$$

2.6.3. Analysis of Periodic Solutions containing a LS

The DAE is especially interesting because of its capability to produce periodic solutions which contain LSs as they open a field of applications in optical communication networks. Those solutions are superpositions of the stable steady state as background and 2π-shifts corresponding to the kinks. Those kinds of solutions gain additional stability from the topology of the 2π-periodic phase space. While this thesis focuses on in the interaction between LSs in periodic solutions and the control of LSs in periodic solutions, an analysis of periodic solutions in the DAE in general is performed in [Mun19] and [MJG20]. The basic results are recalled as they are necessary for this work.
Two types of periodic solutions are produced by the DAE. Oscillating solutions are defined as non-constant periodic solutions which do not perform a 2π-shift. They do not contain a LS. Those solutions arise from the steady states via a Hopf bifurcation. Rotating solutions are periodic solutions containing at least one 2π-shift. This thesis concentrates on these kinds of solutions. A continuation of one branch of steady states, oscillating and rotating periodic solutions indicates that the rotating solutions emerge from the unstable steady states via a global bifurcation. The continued branches are shown in fig. 2.5. The scaling of the periods of the rotating solutions close to the global bifurcation suggests a connection via an homoclinic orbit. For a more detailed analysis of fig. 2.5 and the global bifurcation see [MJG20].
The analysis of the stability of periodic solutions in general is explained in section 2.4.2.

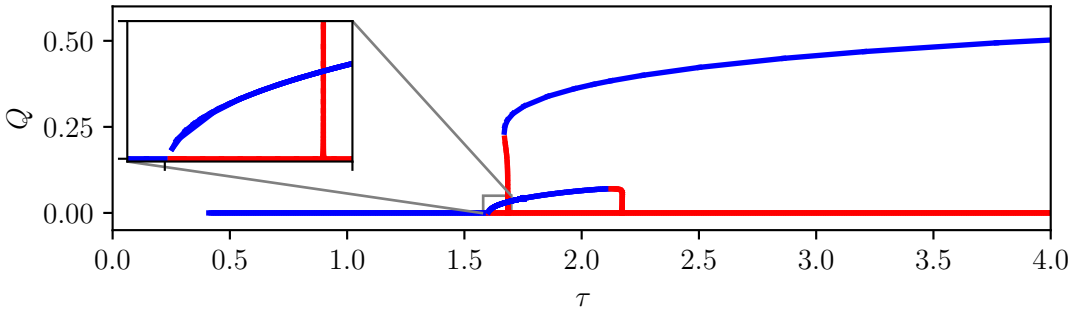

Figure 2.5: Continuation in τ of steady states, oscillating periodic solutions and rotating periodic solutions of eq. (2.1) for the parameter set: $\Delta = 0.7$, $\chi = 1.0$, $\psi = 2,84$. $Q = \frac{\delta\theta}{2\pi}\frac{\tau}{T}$ is chosen as a measure since it corresponds to the amplitude of the oscillation of the solution in one delay τ normalized with respect to one 2π-shift and to the period T. Blue lines and red lines correspond to stable and unstable solutions, respectively.

2.7. Interaction Between LSs Described by the Equation of Motion – EOM

The co-moving reference frame is explained in section 2.1 and an example is presented in fig. 2.1. It indicates that time evolutions, which contain LSs, are described well by the position (of the center) of the LSs $0 < x(r) < \tilde{T}$ in the round trip r in the representation of the co-moving reference frame with respect to a round trip length $\tilde{T}$. An ODE for the evolution of the positions $x(r)$ of the LSs of the DAE is derived in [Mun19] and [MJG20]. It is called the EOM for the system. Additionally, an EOM is derived the PDE that corresponds to the DAE in [Gar+15]. The derivation of the EOM for the DAE is revisited in the following, as it is investigated further in this thesis.

2.7.1. Ansatz for a Periodic Solution Containing LSs

Periodic solutions containing $i = 1, ..., n$ kinks are superpositions of the stable steady state θ_s and n stable orbits $\tilde{\theta}_{i,r} = \tilde{\theta}_{i,r}(t - x_i(r) - r\tilde{T})$ from 0 to 2π centered around $x_i(r)$. Hence, they are written as

$$\theta(t) = \theta_s + \tilde{\theta}_{LSs} = \theta_s + \sum_i \sum_r \tilde{\theta}_{i,r}(t - x_i(r) - r\tilde{T}) \tag{2.61}$$

where $\tilde{\theta}_{LSs}$ describes the 2π-shifts of the LSs. Inserting eq. (2.61) into eq. (2.1) leads to

$$\begin{aligned} \frac{d\left(\theta_s + \tilde{\theta}_{LSs}\right)(t)}{dt} &= \dot{\tilde{\theta}}_{LSs}(t) = F\left(\tilde{\theta}_{LSs}(t), \tilde{\theta}_{LSs}(t-\tau)\right) \\ &= \Delta - \sin\left(\theta_s + \tilde{\theta}_{LSs}(t)\right) + \chi \sin\left(\tilde{\theta}_{LSs}(t-\tau) - \tilde{\theta}_{LSs}(t) - \psi\right). \end{aligned} \tag{2.62}$$

In a sufficient distance to the LS, the shape of a kink leaving ($t < x_i(r) + r\tilde{T}$) and entering ($t > x_i(r) + r\tilde{T}$) the stable steady state can be approximated by a superposition

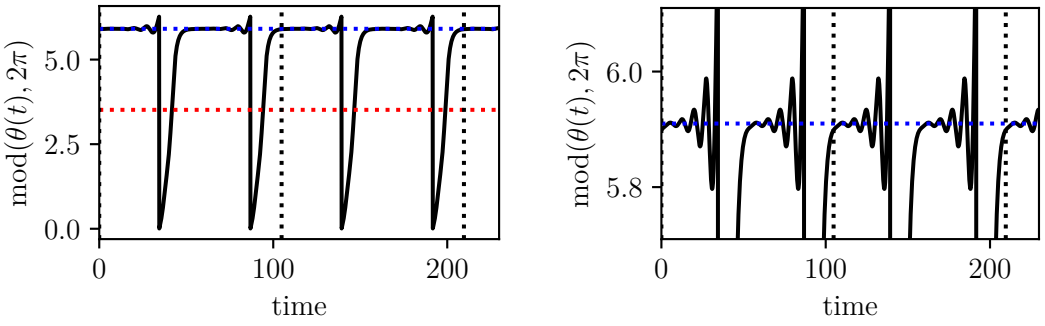

(a) time evolution **(b)** zoomed in view of (a)

Figure 2.6: Result of a DNS of the DAE after the transient for the parameter set: $\Delta = 0.49$, $\psi = 2.1$, $\chi = 0.99$, $\tau = 100$ and $\epsilon = 1 \times 10^{-8}$. (Black) Extracted part of the time evolution of $\mathrm{mod}\,(\theta(t), 2\pi)$ of a periodic solution which contains two kinks where (dotted-black) the end of each period of length $T \approx 104.80$ is marked. Blue and red dotted lines correspond to the stable and unstable steady state, respectively. The y-axis is rescaled in (b) to focus on the exponential tails of the LSs.

of exponential tails

$$\begin{aligned}&\tilde{\theta}_{i,r}(t - x_i(r) - r\tilde{T}) \\ &= \begin{cases} \quad \Re\left(\sum_j f_-^{(j)} \exp\left(\sigma_-^{(j)}\left(t - x_i(r) - r\tilde{T}\right)\right)\right) & \text{for} \quad t < x_i(r) + r\tilde{T} \\ 2\pi+ \quad \Re\left(\sum_j f_+^{(j)} \exp\left(\sigma_+^{(j)}\left(t - x_i(r) - r\tilde{T}\right)\right)\right) & \text{for} \quad t > x_i(r) + r\tilde{T} \end{cases}\end{aligned} \tag{2.63}$$

with eigenvalues $\sigma_\pm^{(j)} \in \mathbb{C}$ and corresponding eigenvectors $f_\pm^{(j)} \in \mathbb{C}$. Complex eigenvalues $\sigma_\pm^{(j)}$ lead to oscillating tails and real eigenvalues to monotonic tails. An example for the oscillating tails of the LSs is shown in fig. 2.6. Moreover, $f_\pm^{(j)} = 0 \quad \forall j : \Re\left(\sigma_\pm^{(j)}\right) \gtrless 0$ is required, since a LS is a bounded structure. Sufficiently far from the kink, the exponential tails in eq. (2.63) are characterized by the term with the highest negative (lowest positive) real part of the eigenvalue $\sigma_-^{(j)} = \sigma_-$ ($\sigma_+^{(j)} = \sigma_+$) and the corresponding eigenvector $f_-^{(j)} = f_-$ ($f_+^{(j)} = f_+$). Using this approximation eq. (2.63) reduces to

$$\begin{aligned}&\tilde{\theta}_{i,r}(t - x_i(r) - r\tilde{T}) \\ &= \begin{cases} \quad \Re\left(f_- \exp\left(\sigma_-\left(t - x_i(r) - r\tilde{T}\right)\right)\right) & \text{for} \quad t < x_i(r) + r\tilde{T} \\ 2\pi+ \quad \Re\left(f_+ \exp\left(\sigma_+\left(t - x_i(r) - r\tilde{T}\right)\right)\right) & \text{for} \quad t > x_i(r) + r\tilde{T}. \end{cases}\end{aligned} \tag{2.64}$$

2.7.2. Derivation of $\sigma_\pm$ via an Eigenvalue Problem

The impact of a LSs, which is sufficient far away, on $\theta(t)$ in eq. (2.61) is neglectable due to the exponential tails of the kinks. Hence, a periodic solution containing one LSs

$\tilde{\theta}_{LSs} = \tilde{\theta}$ has the form

$$\theta(t) = \theta_s + \tilde{\theta}(t-x) = \theta_s + \Re\left(f_\pm \exp\left(\sigma_\pm\left(t - x(r) - r\tilde{T}\right)\right)\right) \tag{2.65}$$

where $r \in \mathbb{N}$ is chosen such that $\left|t - x(r) - r\tilde{T}\right|$ is minimal. In the following, $r' \in \mathbb{N}$ is chosen similarly such that $\left|t - x(r') - r'\tilde{T} - \tau\right|$ is minimal. For $\tilde{T}$ close to T, r' is usually found to be $r-1$. The structure is similar to eq. (2.15) and therefore leads to a similar eigenvalue problem as in eq. (2.16)

$$\begin{aligned}\sigma_\pm f_\pm \exp\left(\sigma_\pm\left(t - x(r) - r\tilde{T}\right)\right) &= \frac{\partial F}{\partial\tilde{\theta}(t)}\left(\tilde{\theta}(t), \tilde{\theta}(t-\tau)\right) f_\pm \exp\left(\sigma_\pm\left(t - x(r) - r\tilde{T}\right)\right) \\ &+ \frac{\partial F}{\partial\tilde{\theta}(t-\tau)}\left(\tilde{\theta}(t), \tilde{\theta}(t-\tau)\right) f_\pm \exp\left(\sigma_\pm\left(t - x(r') - r'\tilde{T} - \tau\right)\right).\end{aligned} \tag{2.66}$$

This derivation focuses on periodic solutions $\theta(t)$. The period $T = \tau + s$ is defined via the drift of the solution s with respect to the delay τ. Hence, the term in brackets in the last exponent is written as $t - x(r') - r'\tilde{T} - \tau = t - x(r) - r\tilde{T} + x(r) - x(r') + (r-r')\tilde{T} + s - T$. $x(r) - x(r') + (r-r')\tilde{T}$ is identified as the period T, since $x(r) - x(r')$ corresponds to the mismatch between T and $\tilde{T}$. Therefore, the term in brackets in the last exponent reduces to $t - x(r) - r\tilde{T} + s$. Similarly to eq. (2.17), the final eigenvalue problem reads

$$\sigma_\pm = A + B\exp\left(\sigma_\pm s\right) \tag{2.67}$$

with the same constants A and B given in eq. (2.18) and eq. (2.19), respectively. Similarly to the calculation in section 2.6.2

$$\sigma_+ = \frac{1}{s}\left(As - W_0\left(-Bs\exp\left(As\right)\right)\right) \tag{2.68}$$

and

$$\sigma_- = \frac{1}{s}\left(As - W_{-1}\left(-Bs\exp\left(As\right)\right)\right) \tag{2.69}$$

are obtained. The eigenvalue problem and therefore $\sigma_\pm$ is independent of the choice of the folding parameter for the co-moving reference frame $\tilde{T}$, but on the actual period $T = \tau + s$. Note that the period T of a periodic solution containing LSs cannot be calculated analytically but with numerical methods as DNSs or `DDE-BIFTOOL` only.

2.7.3. Derivation of the Adjoint Problem Leading to the EOM

Periodic solutions containing two LSs may be written as $\tilde{\theta}_{LSs} = \tilde{\theta}_1 + \tilde{\theta}_2$. Each of the $i = 1, 2$ kinks is a solution of eq. (2.62) for a single LS, $\dot{\tilde{\theta}}_i(t) = F\left(\tilde{\theta}_i(t), \tilde{\theta}_i(t-\tau)\right)$. Hence,

the left hand side of eq. (2.62) reads

$$\begin{aligned}\frac{d\left(\theta_s+\tilde{\theta}_1(t-x_1)+\tilde{\theta}_2(t-x_2)\right)}{dt} &= (1-\dot{x}_1)\,\dot{\tilde{\theta}}_1(t)+(1-\dot{x}_2)\,\dot{\tilde{\theta}}_2(t)\\ &= -\dot{x}_1\dot{\tilde{\theta}}_1(t)-\dot{x}_2\dot{\tilde{\theta}}_2(t)+\dot{\tilde{\theta}}_1(t)\\ &\quad + F\left(\tilde{\theta}_2(t-x_2),\tilde{\theta}_2(t-\tau-x_2)\right). \end{aligned} \tag{2.70}$$

In the vicinity of the second LS the right hand side of eq. (2.62) is approximated around $F\left(\tilde{\theta}_2(t-x_2),\tilde{\theta}_2(t-\tau-x_2)\right)$:

$$\begin{aligned}&F\left(\tilde{\theta}_1(t-x_1)+\tilde{\theta}_2(t-x_2),\tilde{\theta}_1(t-x_1-\tau)+\tilde{\theta}_2(t-x_2-\tau)\right)\\ &\simeq F\left(\tilde{\theta}_2(t-x_2),\tilde{\theta}_2(t-\tau-x_2)\right)+\tilde{\theta}_1(t-x_1)\frac{\partial}{\partial\tilde{\theta}_{LSs}(t)}F\left(\tilde{\theta}_2(t-x_2),\tilde{\theta}_2(t-\tau-x_2)\right)\\ &+\tilde{\theta}_1(t-x_1-\tau)\frac{\partial}{\partial\tilde{\theta}_{LSs}(t-\tau)}F\left(\tilde{\theta}_2(t-x_2),\tilde{\theta}_2(t-\tau-x_2)\right). \end{aligned} \tag{2.71}$$

Combining eq. (2.70) and eq. (2.71) results in

$$\begin{aligned}-\dot{x}_1\dot{\tilde{\theta}}_1(t)-\dot{x}_2\dot{\tilde{\theta}}_2(t) =& -\dot{\tilde{\theta}}_1(t)+\tilde{\theta}_1(t-x_1)\frac{\partial}{\partial\tilde{\theta}_{LSs}(t)}F\left(\tilde{\theta}_2(t-x_2),\tilde{\theta}_2(t-\tau-x_2)\right)\\ &+\tilde{\theta}_1(t-x_1-\tau)\frac{\partial}{\partial\tilde{\theta}_{LSs}(t-\tau)}F\left(\tilde{\theta}_2(t-x_2),\tilde{\theta}_2(t-\tau-x_2)\right)\\ =&\tilde{\theta}_1(t-x_1)\left(-\sigma_\pm+\frac{\partial}{\partial\tilde{\theta}_{LSs}(t)}F\left(\tilde{\theta}_2(t-x_2),\tilde{\theta}_2(t-\tau-x_2)\right)\right)\\ &+\tilde{\theta}_1(t-x_1-\tau)\frac{\partial}{\partial\tilde{\theta}_{LSs}(t-\tau)}F\left(\tilde{\theta}_2(t-x_2),\tilde{\theta}_2(t-\tau-x_2)\right)\\ =&\Re\left(f_\pm\exp\left(\sigma_\pm\left(t-x_1(r)-r\tilde{T}\right)\right)\right.\\ &\left(-\sigma_\pm+\frac{\partial}{\partial\tilde{\theta}_{LSs}(t)}F\left(\tilde{\theta}_2(t-x_2),\tilde{\theta}_2(t-\tau-x_2)\right)\right)\\ &+f_\pm\exp\left(\sigma_\pm\left(t-x_1(r')-r'\tilde{T}-\tau\right)\right)\\ &\left.\frac{\partial}{\partial\tilde{\theta}_{LSs}(t-\tau)}F\left(\tilde{\theta}_2(t-x_2),\tilde{\theta}_2(t-\tau-x_2)\right)\right) \end{aligned} \tag{2.72}$$

since $\dot{\tilde{\theta}}_{i,r}(t)=\sigma_\pm\tilde{\theta}_{i,r}(t)$ is obtained from eq. (2.65). The following steps on projecting eq. (2.72) onto the neutral mode of the adjoint problem and simplifications which are performed in advance are explained in [MJG20].

2.7.4. General Form of the EOM

The adjoint problem leads to the EOM for a periodic solution containing two kinks [MJG20]. This result is generalized to a periodic solution containing $i=1,...,n$ sufficiently separated LSs. The time evolutions of the positions of the LSs are given by the

ODE

$$\dot{x}_i(r) = \Re\left(F_+ \exp\left(\sigma_+ D_-^{(i)}(r)\right) + F_- \exp\left(-\sigma_- D_+^{(i)}(r)\right)\right) \tag{2.73}$$

where $0 \leq D_+^{(i)}(r) = x_{\text{next}} - x_i(r) \leq T$ ($0 \leq D_-^{(i)}(r) = x_i(r) - x_{\text{previous}} \leq T$) is the distance from the i-th LSs $x_i(r)$ to the next $x_{\text{next}} = x_{(i \bmod n)+1}\,(r + ((i+1) > n)) + ((i+1) > n)\,\tilde{T}$ (previous $x_{\text{previous}} = x_{((i-2) \bmod n)+1}\,(r - ((i-1) < 1))$) LSs and $\sigma_\pm \in \mathbb{C}$ are constants given by the eigenvalue problem in eq. (2.67). The constants $F_\pm \in \mathbb{C}$ are defined as

$$F_\pm = \frac{\int_{-\infty}^{\infty} \dot{\tilde{\theta}}^\dagger(y) \exp(\sigma_\pm y) \left[\frac{\partial F}{\partial \tilde{\theta}}\left(\tilde{\theta}, \tilde{\theta}_\tau\right) - \sigma_\pm + \exp(\sigma_\pm s)\, \frac{\partial F}{\partial \tilde{\theta}_\tau}\left(\tilde{\theta}, \tilde{\theta}_\tau\right)\right] dy}{\int_{\infty}^{\infty} \dot{\tilde{\theta}}^\dagger(y) \dot{\tilde{\theta}}(y) dy} f_\pm. \tag{2.74}$$

The distances $D_\pm$ do not depend on the chosen folding parameter $\tilde{T}$.

2.8. The DAE with Periodic Potential Built Up Component by Component

The phenomenon of synchronization is explained in section 2.3 using the example of a quasilinear oscillator with additional external periodic forcing. The DAE with periodic potential may be regarded as multiple nested systems in which synchronization occurs. Therefore, the equation is built up term by term in the following.

The general Adler Equation without feedback ($\chi = 0$) and without potential ($A = 0$) written in eq. (2.6) describes the phase difference between two oscillators. In this study those oscillators correspond to the two lasers – master and slave laser in fig. 2.4. The master laser can be regarded as an external periodic force to the slave laser. Hence, the phase of the slave laser is locked for weak detuning $|\Delta| < 1$ to the phase of the master laser. In this case synchronization is observed, which corresponds to the fixed points in the flow diagram shown in fig. 2.2 that are given by eq. (2.53) and eq. (2.54) for $\chi = 0$. Additionally, this system is excitable as mentioned in section 2.2.

This locked system as a whole may be regarded as an emitting laser and therefore as an oscillator as well. It is extended by the feedback loop for $\chi \neq 0$. As the slave laser was previously fed with the beam of the master laser, this (locked) laser is fed with its own delayed beam. Since the system is similar to the previous system of slave and master laser, because it is an emitting laser with an additional input beam, the dynamics of the phase difference between the two beams in the system is again described by a modified Adler Equation. Hence, it can be regarded as a system of two nested Adler equations. A modification is necessary since the input beam is not coming from an external master laser, but is the delayed emitted beam returning from the feedback loop. However, the complete system so far can be described by the DAE eq. (2.1). The steady states of the general Adler equation still exist, but are modified as well which can be seen in eq. (2.53) and eq. (2.54) for $\chi \neq 0$. Additionally, periodic solutions with LSs occur. Those solutions are the result of periodic excitations of the system. As periodic objects,

they can be described by periodic motions as the result of an harmonic oscillator.
As a next step of the experimental investigation of a system which is described by the DAE [Gar+15], an additional periodic potential is introduced to the experimental setup [Gar+17]. This external periodic potential is meant to work on the periodic solutions containing a LS which can be described similarly to the solutions of an harmonic oscillator. Thus, again a system is created where synchronization can be observed. The setting may also be regarded as a stationary potential (with respect to its own period) which acts on a particle (here the LSs), since it is observed that the periodic potential acts as a master clock to the (multiple) LSs which are trapped in the potential.
The DAE with periodic potential is given in eq. (4.1). In general, the similarities between PDEs and DDEs which are mentioned in section 2.1 lead to a similar framework for the analysis of both kinds of differential equations. Additionally, a corresponding PDE to the DAE with periodic potential exists. It is investigated in [Gar+17]. Synchronization between the potential and a periodic solution of multiple LSs is observed experimentally and validated via DNSs.

3. Interaction of LSs in the DAE

Interactions between LSs of the DAE are experimentally observed in [Gar+15] and theoretically investigated with the model described by the EOM which is derived in section 2.7. The understanding, description and control of LSs and therefore of their interaction is important in order to use the advantages of topological LSs in applications in optical communication systems and optical memories. Especially the interaction of multiple LSs which are stored in one delay time τ is interesting for such applications. Hence, a new method to obtain the important values $F_\pm$ is investigated for solutions containing two LSs to improve the predictions about the dynamics made by the EOM. Additionally, the impact of the delay time τ on the difference between these two LSs is explored.

3.1. Simulations of the Dynamics via DNSs of the EOM

The output of the EOM is compared to results obtained with the DNSs of the DAE for different parameter sets in [Mun19] and [MJG20]. Both methods are compared using periodic solutions with two LSs. The coefficients $\sigma_\pm$ and $F_\pm$ are calculated using eq. (2.68), eq. (2.69) and eq. (2.74). The ODE given in eq. (2.73) is reduced to the term related to the smaller distance $\min\left(D_+^i, D_-^i\right)$.
For some parameter sets both methods lead to similar time evolutions which indicates that the dynamics of LSs might be obtainable via the EOM. Nevertheless, for other parameter sets a significant mismatch between both methods is reported, especially in the transients before converging to a final distance. The calculation of the dynamics of a periodic solution containing LSs via DNS of the ODE of the EOM (eq. (2.73)) reduces calculation time and memory costs significantly compared to the DNSs of the DAE (eq. (2.1)). All in all, it illustrates the EOM as a promising model for the calculation of dynamics of the DAE where further improvements need to be made. Therefore, this thesis focuses on options how the use of the equation of the motion may be implemented such that the mismatch to the dynamics calculated from the DAE reduces.
The parameters $\Delta = 0.49$, $\psi = 2.1$, $\chi = 0.99$ and $\tau = 100$ are chosen as this parameter set corresponds to one which was investigated in [Mun19] and [MJG20] for the comparison between the output of the EOM and the results of the DNSs of the DAE. The final distances which are obtained after hundreds of round trips with both models match for starting distances between 10 and 35. However, the evolutions over the round trips of those distances – until the final distance is reached – does not match. The mismatch is explained through the chosen parameter set which is in the vicinity of a period doubling regime for a periodic solution containing one kink. A precursor of the period-doubling instability is presented in fig. 3.1. According to [MJG20], the period-2 orbit modifies the interaction which leads to the mismatch in the transient. However, fig. 2.6 shows that periodic solutions containing two kinks do not show signs of a period-2 orbit. Therefore, the calculation of $F_\pm$ via eq. (2.74), which uses the periodic solution of the DAE

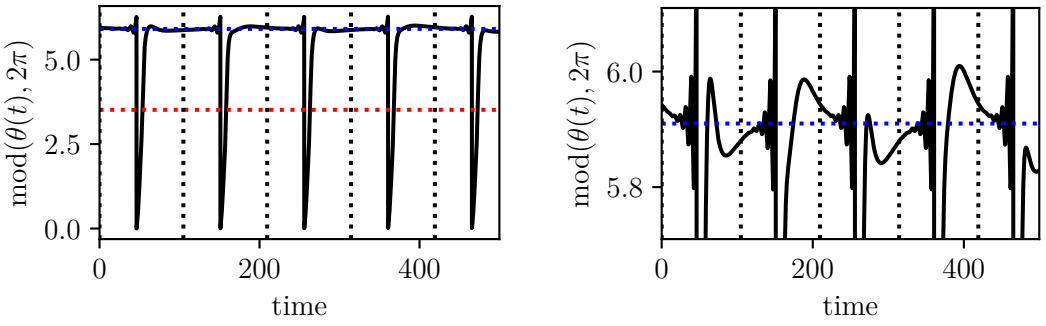

(a) time evolution **(b)** zoomed in view of (a)

Figure 3.1: Result of the DNSs of the DAE after the transient for the parameter set: $\Delta = 0.49$, $\psi = 2.1$, $\chi = 0.99$, $\tau = 100$ and $\epsilon = 1 \times 10^{-8}$. (Black) Part of the time evolution of mod $(\theta(t), 2\pi)$ of a periodic solution which contains one kink where (dotted-black) the end of each period of length $T \approx 104.80$ is marked. Blue and red dotted lines correspond to the stable and unstable steady state, respectively. The y-axis is rescaled in (b) to focus on the period-2 orbit of the solution.

containing one kink has a structural disadvantage. Instead of a calculation of $F_\pm$ via eq. (2.74) using an algorithm implemented in `DDE-BIFTOOL`, as in [Mun19] and [MJG20], this study fits those values from solutions which are obtained via DNSs of eq. (2.1).

3.1.1. Periodic Solutions Containing Two LSs

This thesis focuses on periodic solutions containing two LSs. Hence, eq. (2.73) reads

$$\dot{x}_1(r) = \Re\left(F_+ \exp\left(\sigma_+ D_-^{(1)}\right) + F_- \exp\left(-\sigma_- D_+^{(1)}\right)\right) \tag{3.1}$$

and

$$\dot{x}_2(r) = \Re\left(F_+ \exp\left(\sigma_+ D_-^{(2)}\right) + F_- \exp\left(-\sigma_- D_+^{(2)}\right)\right) \tag{3.2}$$

for two LSs. Moreover, the relations $D_+^{(i)}(r) + D_-^{(i)}(r) = T$ and $D_\pm^{(1,2)}(r) = D_\mp^{(2,1)}(r)$ apply $\forall r, i$. Additionally, the minimal distance between the LSs is defined as

$$\begin{aligned} 0 \leq D(r) &= \min\left(D_-^{(1,2)}(r), D_+^{(1,2)}(r)\right) \\ &= \min\left(|x_2(r) - x_1(r)|, T - |x_2(r) - x_1(r)|\right) \leq \frac{T}{2} \end{aligned} \tag{3.3}$$

and the sum of the positions of both LSs is inductively defined as

$$S(r) = \begin{cases} x_1(r) + x_2(r) + T & \text{if} \quad x_1(r) + x_2(r) - S(r-1) \approx -T \\ x_1(r) + x_2(r) - T & \text{if} \quad x_1(r) + x_2(r) - S(r-1) \approx T \\ x_1(r) + x_2(r) & \text{else.} \end{cases} \tag{3.4}$$

Despite the minimal and absolute value terms, eq. (3.3) still results in a continuous evolution of $D(r)$. The derivative of the minimal distance $\dot{D}(r)$ is given by

$$\begin{aligned}
\dot{D}(r) =& (\dot{x}_2(r) - \dot{x}_1(r)) \begin{cases} 1 & \text{for} \quad D = D_+^{(1)} \\ (-1) & \text{for} \quad D = D_-^{(1)} \end{cases} \\
=& \Re \left(F_+ \left(\exp\left(\sigma_+ D_+^{(1)}\right) - \exp\left(\sigma_+ D_-^{(1)}\right)\right)\right. \\
& \left. + F_- \left(\exp\left(-\sigma_- D_-^{(1)}\right) - \exp\left(-\sigma_- D_+^{(1)}\right)\right) \begin{cases} 1 & \text{for} \quad D = D_+^{(1)} \\ (-1) & \text{for} \quad D = D_-^{(1)} \end{cases} \right) \\
=& \Re \left(F_+ \begin{cases} \exp\left(\sigma_+ D_+^{(1)}\right) - \exp\left(\sigma_+ \left(T - D_+^{(1)}\right)\right) \\ \exp\left(\sigma_+ D_-^{(1)}\right) - \exp\left(\sigma_+ \left(T - D_-^{(1)}\right)\right) \end{cases} \right. \\
& \left. + F_- \begin{cases} \exp\left(-\sigma_- \left(T - D_+^{(1)}\right)\right) - \exp\left(-\sigma_- D_+^{(1)}\right) & \text{for} \quad D = D_+^{(1)} \\ \exp\left(-\sigma_- \left(T - D_-^{(1)}\right)\right) - \exp\left(-\sigma_- D_-^{(1)}\right) & \text{for} \quad D = D_-^{(1)} \end{cases} \right) \\
=& \Re \left(F_+ \left(\exp\left(\sigma_+ \left(T - D\right)\right) - \exp\left(\sigma_+ D\right)\right)\right. \\
& \left. + F_- \left(\exp\left(-\sigma_- \left(T - D\right)\right) - \exp\left(-\sigma_- D\right)\right)\right) \qquad (3.5) \\
=& \Im \left(2F_+ \exp\left(\sigma_+ \frac{T}{2}\right) \sinh\left(\sigma_+ \left(D - \frac{T}{2}\right)\right)\right. \\
& \left. + 2F_- \exp\left(-\sigma_- \frac{T}{2}\right) \sinh\left(\sigma_- \left(D - \frac{T}{2}\right)\right)\right). \qquad (3.6)
\end{aligned}$$

Theoretically, a distance is constant over round trips if $\dot{D} \stackrel{!}{=} 0$. Among others, this condition is fulfilled for $D - \frac{T}{2} = 0$ which is independent of $\sigma_\pm$ and $F_\pm$, as eq. (3.6) indicates. It corresponds to a periodic solution containing two LSs which are separated by $\frac{T}{2}$. Note that $\sigma_\pm \in \mathbb{C}$ and hence the sinh-functions in eq. (3.6) have complex arguments, in general.

Similarly to the $\dot{D}(r)$, $\dot{S}(r)$ is obtained. It reads

$$\begin{aligned}
\dot{S}(r) =& \Re \left(F_+ \left(\exp\left(\sigma_+ \left(T - D\right)\right) + \exp\left(\sigma_+ D\right)\right)\right. \\
& \left. + F_- \left(\exp\left(-\sigma_- \left(T - D\right)\right) + \exp\left(-\sigma_- D\right)\right)\right) \qquad (3.7) \\
=& \Re \left(2F_+ \exp\left(\sigma_+ \frac{T}{2}\right) \cosh\left(\sigma_+ \left(D - \frac{T}{2}\right)\right)\right. \\
& \left. + 2F_- \exp\left(-\sigma_- \frac{T}{2}\right) \cosh\left(\sigma_- \left(D - \frac{T}{2}\right)\right)\right) \qquad (3.8)
\end{aligned}$$

in the final forms. Equation (3.8) shows that $D = \frac{T}{2}$ does not lead to $\dot{S} = 0$ in general. An example of the evolution of $D(r)$ and $S(r)$ for a periodic solution that contains two LSs is given in fig. 3.2. The evolution is visualized in the co-moving reference frame with respect to two different folding parameters $\tilde{T}$. It shows that the evolution of $S(r)$ and hence also $\dot{S}(r)$ is dependent on the chosen folding parameter $\tilde{T}$. The minimal distance $D(r)$ between the kinks, however, is constant in both cases and therefore $\dot{D}(r) = 0$ is

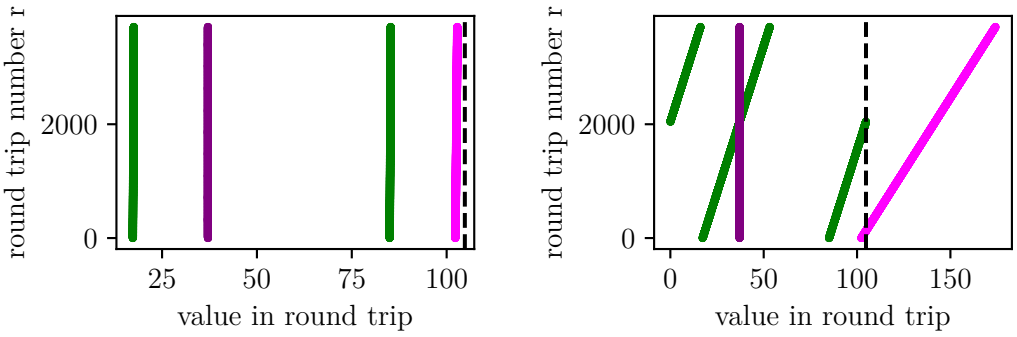

(a) $\tilde{T} = T \approx 104.80$ **(b)** $\tilde{T} \approx 104.79$

Figure 3.2: Example for the evolution of (green) the positions of the LSs $x_i(r)$, (purple) the distance between both kinks $D(r)$ defined in eq. (3.3) and (magenta) the sum of the positions of both LSs $S(r)$ given by eq. (3.4). (A) $\tilde{T} = T \approx 104.80$ and (b) $\tilde{T} \approx 104.79$ is chosen as the folding parameter for the co-moving reference frame. It is marked by the dotted black line. The example is extracted from the result of a DNS of the DAE for the parameter set: $\Delta = 0.49$, $\psi = 2.1$, $\chi = 0.99$, $\tau = 100$ and $\epsilon = 1 \times 10^{-8}$.

obtained in both cases. It indicates that $D(r)$ and especially $\dot{D}(r)$ is a more reliable parameter than $\dot{S}$ since it is less dependent on the folding parameter.

3.1.2. Overview of the Investigated Data

101 long time DNSs of periodic solutions containing initially two LSs at different distances are calculated until $t_{\text{end}} = 50000\tau$ for the parameters $\Delta = 0.49$, $\psi = 2.1$, $\chi = 0.99$, $\tau = 100$ and $\epsilon = 1 \times 10^{-8}$. The initial kinks are placed in such a way that $D_+^{(1)}(r = 0) = D_-^{(2)}(r = 0) = T - D_-^{(1)}(r = 0) = T - D_+^{(2)}(r = 0) \in [0, \tau = 100]$. The initial conditions are produced using the analytical ansatz which is described in section 2.5.1. 82 out of the 101 simulations lead to periodic solutions which contain two LSs. In the other 19 cases, the LSs are initially too close to each other such that they collide and one LS gets destroyed leading to a periodic solution with one kink. Since this study focuses on the interaction between LSs, the 82 simulations are further investigated.

The periods T of the periodic solutions are calculated for each simulation individually via auto-correlation of the last 500 delay times τ. The calculated periods of the 82 simulations lie inside the interval $[T_{\text{mean}} - 0.88 \times 10^{-4}, T_{\text{mean}} + 2.12 \times 10^{-4}]$. The mean period is $T_{\text{mean}} = 104.796184$ with a standard deviation of 1.37×10^{-4}. The period of all 19 periodic solutions containing one LS after a few round trips is $T_0 = T_{0_{\text{mean}}} = 104.786486 = T_{\text{mean}} - 96.98 \times 10^{-4}$ with a standard deviation of 0. The distances between the LSs $D(r)$ in eq. (3.3) and the sums of the positions of the LSs $S(r)$ in eq. (3.4) are determined using the individually calculated periods. The mean period of the 82 simulations leading to solutions, which contain two kinks, T_{mean}, is used for all other calculations and simulations. Therefore, $s = T_{\text{mean}} - \tau \approx 4.796184$ is

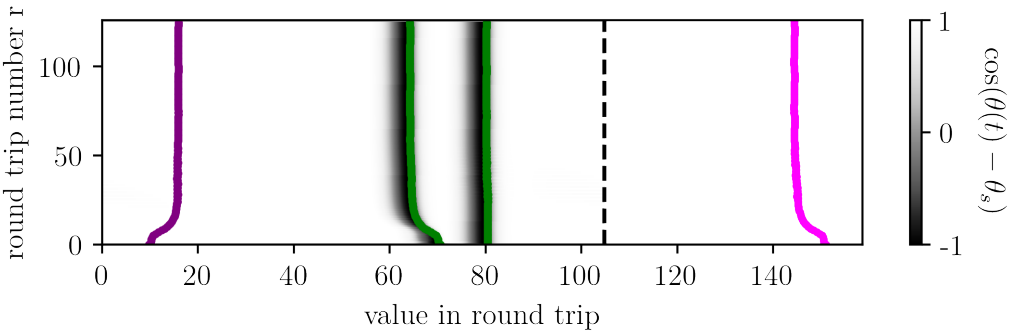

Figure 3.3: Result of (grey-scaled color-plot) a DNS of the DAE, (green) the calculated positions of the LSs $x_i(r)$, (purple) the distance between both LSs $D(r)$ and (magenta) the sum of the positions of both LSs $S(r)$ in the co-moving reference frame with respect to (dotted black) the period $T \approx 104.80$ for the parameter set: $\Delta = 0.49$, $\psi = 2.1$, $\chi = 0.99$, $\tau = 100$ and $\epsilon = 1 \times 10^{-8}$. The dynamics of the LSs is well described by the calculated positions of the LSs.

Table 3.1: Overview of the final distances obtained in the DNSs of the DAE. The mean value $D_{\text{mean}} = D_{\text{mean}}(r \to \infty)$, the standard deviation $D_{\text{std}} = D_{\text{std}}(r \to \infty)$, the difference to between the maximal and the mean value $D_{\text{max}} - D_{\text{mean}} = D_{\text{max}}(r \to \infty) - D_{\text{mean}}(r \to \infty)$ and the difference between the mean and the minimal value $D_{\text{mean}} - D_{\text{min}} = D_{\text{mean}}(r \to \infty) - D_{\text{min}}(r \to \infty)$ are provided.

D_{mean}	D_{std}	$D_{\text{max}} - D_{\text{mean}}$	$D_{\text{mean}} - D_{\text{min}}$
15.93	4.7×10^{-2}	6.7×10^{-2}	3.3×10^{-2}
22.50	1.3×10^{-3}	5.2×10^{-4}	3.4×10^{-3}
29.73	4.8×10^{-2}	6.5×10^{-2}	3.9×10^{-2}
37.10	2.0×10^{-3}	2.0×10^{-3}	2.0×10^{-3}
44.50	1.8×10^{-3}	1.8×10^{-3}	1.8×10^{-3}
52.40	3.5×10^{-7}	1.3×10^{-7}	9.2×10^{-7}

found. Inserting this and eqs. (2.56) and (2.57) with eq. (2.53) into eqs. (2.68) and (2.69) results in $\sigma_+ \approx (-0.48111 + 0i)$ and $\sigma_- \approx (0.15232 + 0.85797i)$, respectively. Thus, the imaginary part of F_+ has no impact on eqs. (3.1), (3.2) and (3.5) and therefore on the dynamics. Hence, it is set to 0 and $F_+ \in \mathbb{R}$ is obtained.

The positions of the LSs in the co-moving reference frame with respect to the period T of each solution are extracted and used for further investigations. One example is visualized in fig. 3.3. The dynamics of the LSs is well described by the calculated positions of the LSs in the co-moving reference frame. Additionally, the evolution of the distance between both LSs $D(r)$ and the sum of the positions of both LSs $S(r)$ is shown.

The evolution of the distances $D(r)$ of the 82 DNSs of the DAE is shown in fig. 3.4. The dynamics are resulting in specific final distances $D(r \to \infty)$ between the kinks. These are illustrated by the blue lines and an overview is provided in table 3.1. D_{std}, D_{max} and D_{min} are in an order of magnitude of expected numerical errors or lower and therefore not significant. The final distance $D_{\text{mean}} = 52.40 \pm 4.7 \times 10^{-2}$ is half of the

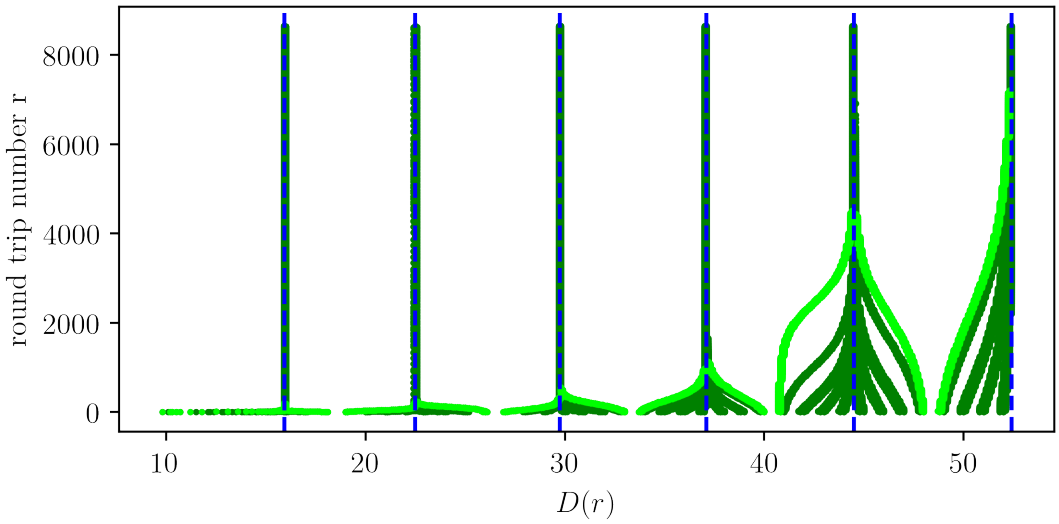

Figure 3.4: Evolutions of the distance $D(r)$ defined in eq. (3.3) of 82 simulations with initially different distances between the LSs. The simulations are calculated for the parameters $\Delta = 0.49$, $\psi = 2.1$, $\chi = 0.99$, $\tau = 100$ and $\epsilon = 1 \times 10^{-8}$. (Green) Evolution of the distances of all 82 DNSs of eq. (2.1), (lime) part of these which are used for the fitting of $F_{\pm}$ and (blue) final distances which are reached after several round trips. An overview of these distances is given in table 3.1.

mean period $T_{\text{mean}} = 104.796184 \pm 1.37 \times 10^{-4}$ as expected through eq. (3.6). Moreover, note that the final distances are not equidistantly separated, as $22.50 - 15.93 = 6.57$ and $52.40 - 44.50 = 7.9$. However, the difference between the final distances D_{mean} increases for increasing distances.

The dynamics of the distance $D(r)$ is approximated by the ODE given in eq. (3.5). Thus, the evolution of the distance at $r > r_0$ is determined by the distance $D_1(r_0)$ at $r = r_0$, as explained in section 2.1. However, it is independent of dynamics before r_0. The evolution of a distance $D_0(r_0) \neq D_1(r_0)$, which passes by the initial distance of D_1 at a later round trip $r_1 > r_0$ ($D_0(r_1) = D_1(r_0)$), is identical to the evolution of D_1 for $r > r_1$. Hence, the evolution D_0 contains all information of D_1 in addition to the information of the evolution for $r_0 < r < r_1$. Therefore, the information of the 82 evolutions shown in fig. 3.4 are included in eleven simulations which are highlighted in a lime color. These evolutions are used for the determination of $F_{\pm}$. Moreover, the lime color indicates which part of the dynamics are taken into account. In general, it is the first part until the final distance is reached, however, a minimum of $0 < r < 200$ round trips are considered. For the evaluation of the derivative $\dot{D}(r)$, a running average over 100 round trips of the difference $D(r)$ is used.

Figure 3.4 shows that the dynamics at higher distances take more round trips r to reach their corresponding final distances and is therefore slower. Hence, the impact of the interaction is decreasing for increasing distance.

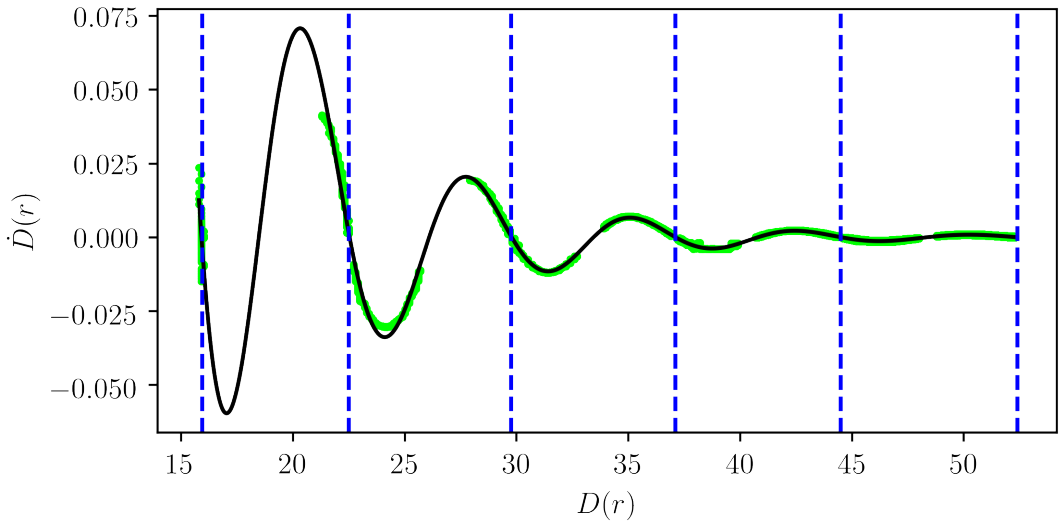

Figure 3.5: $\dot{D}$-D-plane of (lime) the in fig. 3.4 highlighted DNSs of the DAE for the parameters $\Delta = 0.49$, $\psi = 2.1$, $\chi = 0.99$, $\tau = 100$ and $\epsilon = 1 \times 10^{-8}$, (blue) the final distances, which are given in table 3.1, and (black) the fit of eq. (3.5) for $F_\pm$ through the data with $\sigma_+ \approx (-0.48111 + 0i)$ and $\sigma_- \approx (0.15232 + 0.85797i)$. The fitted parameters are $F_+ = 163.46 \pm 0.37$ and $F_- = ((-0.5638 \pm 0.0014) + (1.2880 \pm 0.0021)i)$.

3.1.3. Determination of $F_\pm$

As already mentioned previously, this study does not determine $F_\pm$ through eq. (2.74) as in [Mun19] and [MJG20], but through fitting the output of the DNSs of the DAE with eq. (3.5). Hence, the data of the highlighted simulations in fig. 3.4 is visualized in the $\dot{D}$-D-plane in fig. 3.5. $\dot{D}(r)$ oscillates with decreasing amplitude for increasing distances $D(r)$ again indicating a decreasing impact of the interaction for increasing distances. $\dot{D}(r) = 0$ is obtained at the distances, that correspond to the final distances, which are discussed with the help of fig. 3.4 and table 3.1. This behavior is expected through eq. (3.5). The fit of eq. (3.5) through the data with $\sigma_+ \approx (-0.48111 + 0i)$ and $\sigma_- \approx (0.15232 + 0.85797i)$ determines $F_+ = 163.46 \pm 0.37$ and $F_- = ((-0.5638 \pm 0.0014) + (1.2880 \pm 0.0021)i)$. The fit is in good agreement with the data, especially at the final distances where $\dot{D}(r) = 0$. The absolute values of the real parts of $\sigma_\pm$ indicate that the terms in eqs. (3.1) and (3.2) related to F_+ are dominant for short distances $D_-^{(1,2)} \ll \frac{T}{2}$ and terms related to F_- are dominant for greater distances $D_+^{(1,2)} \approx \frac{T}{2}$. Hence, the dynamics for small minimal distances $D(r) \ll \frac{T}{2}$ is dominated by one of the terms in eqs. (3.1) and (3.2) related to F_+ and dynamics for greater minimal distances $D(r) \approx \frac{T}{2}$ are dominated by both terms related to F_-. The order of magnitude of the absolute values of the fitted constants $F_\pm$ match to the previous observation that fast dynamics are found for smaller distances and the slower ones are observed for greater distances. The explained effect is illustrated in fig. 3.6. Additionally, it shows that the terms related to F_+ are dominant for $D(r) \lesssim 15$ and the terms related to F_-

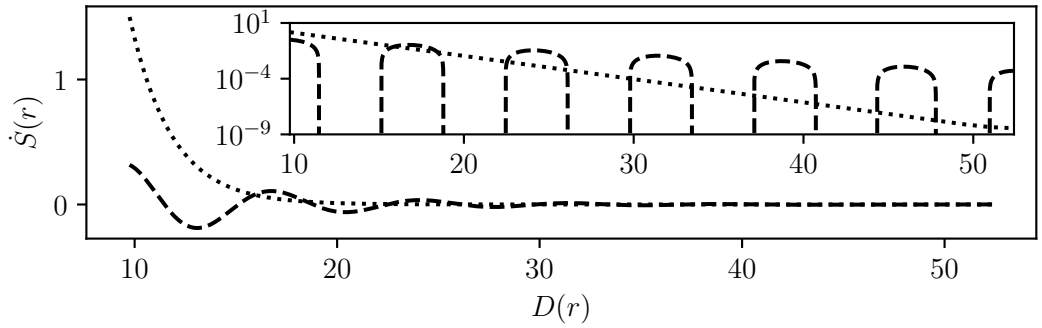

Figure 3.6: Through eq. (3.7) calculated values of $\dot{S}(r)$ by using $\sigma_+ \approx (-0.48111 + 0i)$ and $\sigma_- \approx (0.15232 + 0.85797i)$ and the values $F_+ \approx 163.46$ and $F_- \approx (-0.5638 + 1.2880i)$ fitted in fig. 3.5. The impact of both terms in eqs. (3.1) and (3.2) related to (dotted) F_+ and (dashed) F_- is compared by setting $F_- = 0$ and $F_+ = 0$, respectively.

are dominant for $D(r) \gtrsim 20$. Since the terms correspond to the interaction with the previous and the following kink, respectively, it also indicates that the interactions are not reciprocal. Note that fitting $F_\pm$ through $\dot{S}(r)$, which is given in eq. (3.7), is not leading to a result which describes the dynamics of the kinks as sufficient as fitting $\dot{D}(r)$. A possible reason for this is explained in section 3.1.1 by fig. 3.2: The higher dependency of $\dot{S}(r)$ on the folding parameter used for the co-moving reference frame compared to $\dot{D}(r)$.

3.1.4. Simulations of the EOM Compared to Simulations of the DAE

The results of the DNSs of the DAE (eq. (2.1)) and the EOM (eqs. (3.1) and (3.2)) with the fitted parameters, which are obtained in fig. 3.5 and $\sigma_+ \approx (-0.48111 + 0i)$ and $\sigma_- \approx (0.15232 + 0.85797i)$, are illustrated and compared in figs. 3.7 to 3.9. Figure 3.7 shows fig. 3.4 in addition to the results of the DNSs of the EOM. A zoomed in view of fig. 3.7(a) is provided in fig. 3.8. Figure 3.9 compares the results of the DNSs of the eleven initial conditions, which are used for the fit of $F_\pm$, in the co-moving reference frame. It shows that interactions are not reciprocal. Note that the individual calculated periods and the mean period of all 82 DNSs of the DAE, $T_{\text{mean}} = 104.796184$, are used as the folding parameter for the co-moving reference frame for the results of the DNSs of the DAE and the EOM, respectively leading to a small mismatch between the folding parameters.

In general, the results of the DNSs of the EOM are in good agreement to the DNSs of the DAE. They match especially well for greater distances $D(r) \gtrsim 30$, which is expected as the EOM is an approximation based on great distances between the kinks. Nevertheless, the qualitative behavior, as the overall evolutions of the distance and the final distances, of the dynamics is still well described for $D(r) \gtrsim 10$. However, fig. 3.9(a,b) indicates a mismatch between the folding parameters used for the co-moving reference frame. Since the EOM is a model which is meant to replace the numerically expensive simulations via

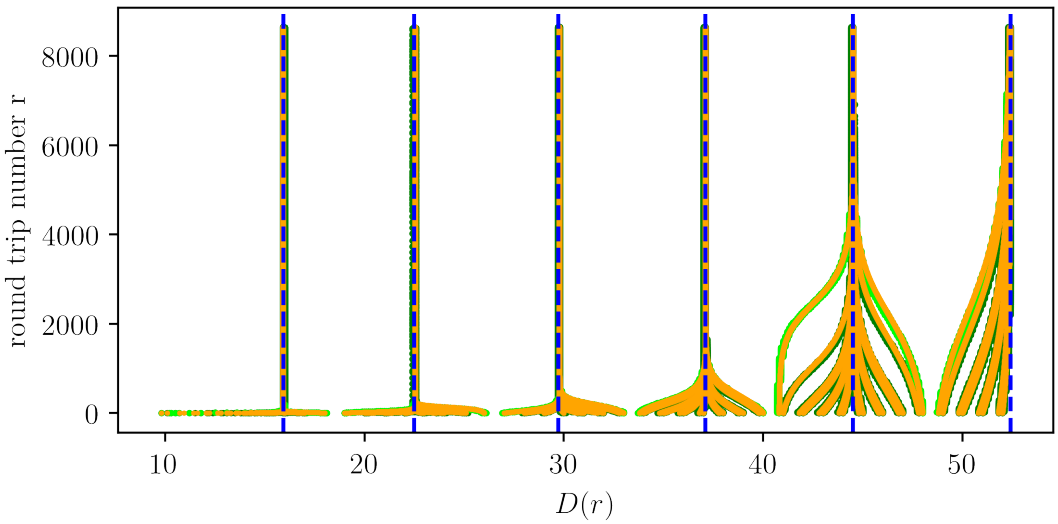

(a) similar initial distances for the DNSs of the DAE and the EOM

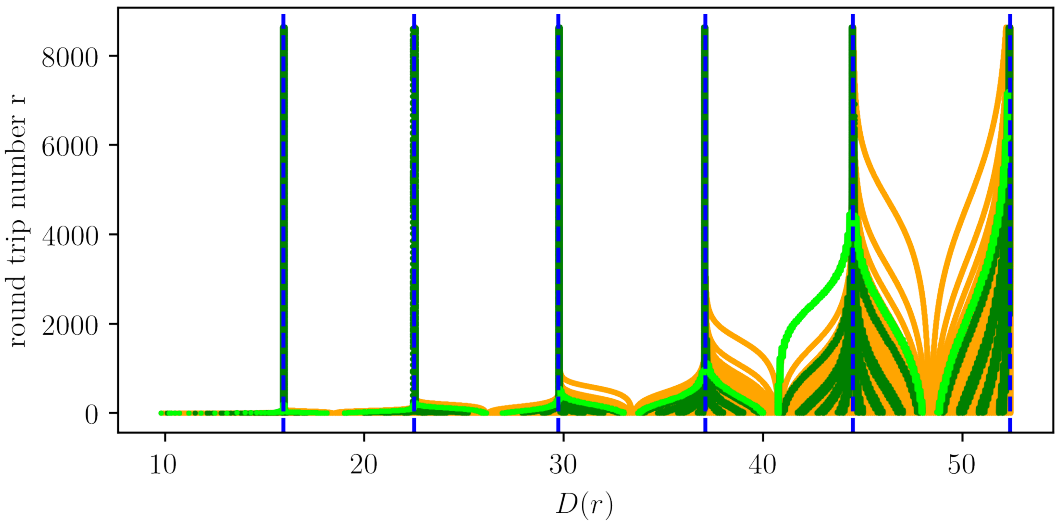

(b) additional DNSs of the EOM with different initial distances

Figure 3.7: Added results of (orange) the DNSs of eqs. (3.1) and (3.2) with $\sigma_+ \approx (-0.48111{+}0i)$ and $\sigma_- \approx (0.15232{+}0.85797i)$ and the in fig. 3.5 fitted values $F_+ \approx 163.46$ and $F_- \approx (-0.5638 + 1.2880i)$ to fig. 3.4 to obtain the evolutions of the distance $D(r)$ defined in eq. (3.3) of simulations with initially different distances between the LSs. The parameters are $\Delta = 0.49$, $\psi = 2.1$, $\chi = 0.99$, $\tau = 100$ and $\epsilon = 1 \times 10^{-8}$. (Green) Evolution of the distances of all 82 DNSs of eq. (2.1), (lime) part of these which are used for the fitting of $F_\pm$, (blue) final distances which are reached after several round trips. The DNSs of the EOM are started with (a) similar initial distances as the DNSs of the DAE and (b) additional initial distances for the visualization of the range of initial conditions approaching a specific final distance. A zoomed in view on the dynamics is presented in fig. 3.8.

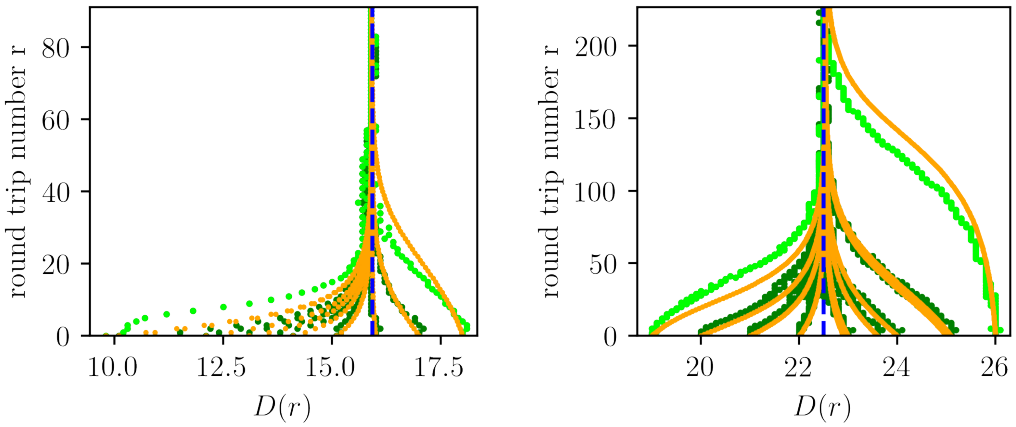

(a) $D(r \to \infty) \approx 15.93$

(b) $D(r \to \infty) \approx 22.50$

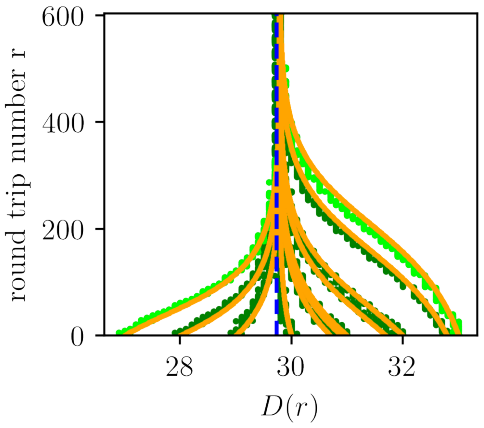

(c) $D(r \to \infty) \approx 29.73$

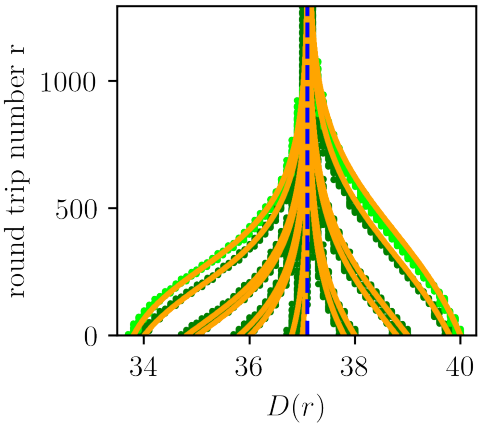

(d) $D(r \to \infty) \approx 37.10$

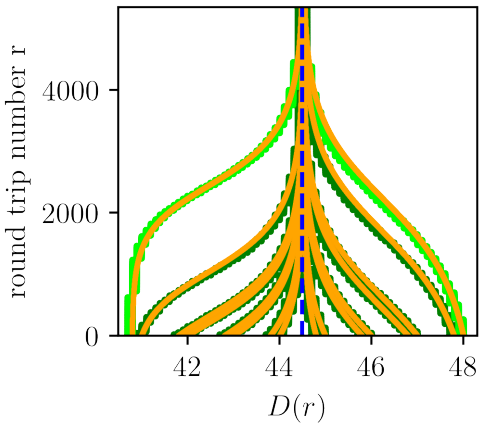

(e) $D(r \to \infty) \approx 44.50$

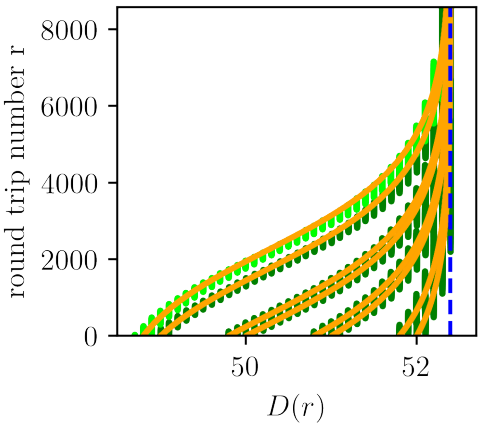

(f) $D(r \to \infty) \approx 52.40$

Figure 3.8: Zoomed in view of fig. 3.4(a) for a better comparison of the evolution of $D(r)$ calculated by the DNSs of the (orange) the EOM and (green) DAE. The part of the latter which is used for the fitting of $F_\pm$ is highlighted in lime and the final distances, which are reached after several round trips, are indicated by blue lines. For the different calculations the parameters $\Delta = 0.49$, $\psi = 2.1$, $\chi = 0.99$, $\tau = 100$ and $\epsilon = 1 \times 10^{-8}$ are used for the DAE and $\sigma_+ \approx (-0.48111 + 0i)$, $\sigma_- \approx (0.15232 + 0.85797i)$ and the in fig. 3.5 fitted values $F_+ \approx 163.46$ and $F_- \approx (-0.5638 + 1.2880i)$ are used for the EOM.

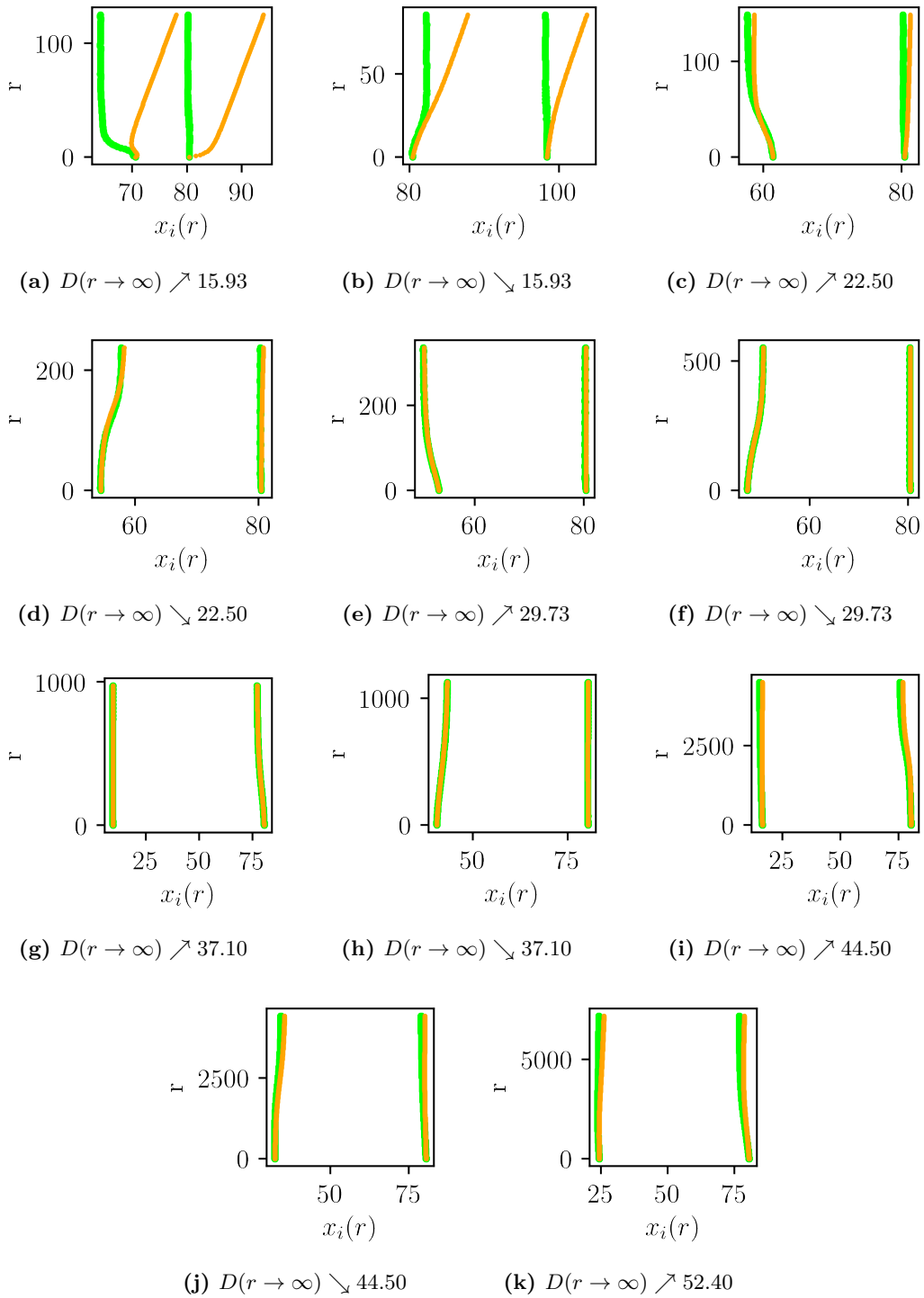

(a) $D(r \to \infty) \nearrow 15.93$ **(b)** $D(r \to \infty) \searrow 15.93$ **(c)** $D(r \to \infty) \nearrow 22.50$

(d) $D(r \to \infty) \searrow 22.50$ **(e)** $D(r \to \infty) \nearrow 29.73$ **(f)** $D(r \to \infty) \searrow 29.73$

(g) $D(r \to \infty) \nearrow 37.10$ **(h)** $D(r \to \infty) \searrow 37.10$ **(i)** $D(r \to \infty) \nearrow 44.50$

(j) $D(r \to \infty) \searrow 44.50$ **(k)** $D(r \to \infty) \nearrow 52.40$

Figure 3.9: Comparison of DNSs of (lime) the DAE which are used for the fit of $F_\pm$ and (orange) the EOM in the co-moving reference frame. The individually calculated period is used as the folding parameter for the first kind of DNSs and the mean period of all 82 DNSs of the DAE, $T_{\text{mean}} = 104.796184$, for the DNSs of the EOM. For the different calculations the parameters $\Delta = 0.49$, $\psi = 2.1$, $\chi = 0.99$, $\tau = 100$ and $\epsilon = 1 \times 10^{-8}$ are used for the DAE and $\sigma_+ \approx (-0.48111 + 0i)$, $\sigma_- \approx (0.15232 + 0.85797i)$ and the in fig. 3.5 fitted values $F_+ \approx 163.46$ and $F_- \approx (-0.5638 + 1.2880i)$ are used for the EOM.

the DAE, it is not reasonable to use the individual period obtained from the result of the corresponding DNS of the DAE, but the mean period T_{mean} for the DNSs of the EOM. Those periods differ up to the order 10^{-4} leading to a mismatch in the order 10^{-2} after 100 round trips in the co-moving reference frame. Hence, the mismatch in fig. 3.9(a,b) cannot be explained by the difference of the folding parameters, in contradiction to the mismatch in fig. 3.9(i-k). Nevertheless, it may be explained by the impact of the mismatch of the periods entering the DNSs of the EOM through the values of $\sigma_{\pm}$, which are determined by eqs. (2.68) and (2.69). Lower distances are not investigated as the results of DNSs of the DAE lead to a collision of the LSs for $D(r) \lesssim 10$.
All in all, the results show that the approximations made in the derivation of the EOM (section 2.7) are valid and that the model of the EOM describes the interaction between the LSs for the given parameter set ($\Delta = 0.49$, $\psi = 2.1$, $\chi = 0.99$, $\tau = 100$) well. The investigated method to determine $F_{\pm}$ via fitting the results of some DNSs of the DAE to eq. (3.5) leads to a significant improvement compared to the results obtained by calculating $F_{\pm}$ through eq. (2.74) in [Mun19] and [MJG20] for the investigated parameter set. An advantage of the method of fitting $F_{\pm}$ through eq. (3.5) instead of calculating it through eq. (2.74) is that a qualitative difference in the profiles of periodic solutions containing one and multiple LSs, as visualized by the comparison of figs. 2.6 and 3.1 due to the period doubling regime for the solution containing one kink, does not effect the fitting $F_{\pm}$.

3.2. Investigation of the Final Distances at Different Delay Times

The interaction between the LSs lead to final distances between the kinks which are presented in table 3.1 for the parameter set $\Delta = 0.49$, $\psi = 2.1$, $\chi = 0.99$ and $\tau = 100$. The dynamics of the LSs and their interaction is investigated by the EOM in section 3.1. The following investigation looks into the dependence of final distances on the delay time τ at the same parameter set.
Six long time DNSs of the DAE of initial conditions containing two kinks which end up in the six final differences given in table 3.1 are used to create six branches of periodic solutions containing two LSs with different distances. These branches are continued in τ and the distances between the LSs with respect to the continuation parameter τ is presented in fig. 3.10. The periodic solutions corrected by `DDE-BIFTOOL` at $\tau = 100$ have the same distances between the kinks as the solutions obtained by the DNSs of the DAE and the EOM. The distance between the kinks of one of the branches changes linearly with the delay time τ. This branch represents the solutions with a distance of $D(r \to \infty) = \frac{T}{2}$ which is analytically expected by eq. (3.6). Since the distance between the kinks is referred to as the minimal distance between the kinks by eq. (3.3) with $D(r \to \infty) \leq \frac{T}{2}$, no branches are found in the region $D(r \to \infty) > \frac{T}{2}$. Moreover, the stability of the branch at $D(r \to \infty) = \frac{T}{2}$ changes its stability at each point where it collides with the other branches. The Floquet-multipliers indicate a fold or flip bifurcation, but

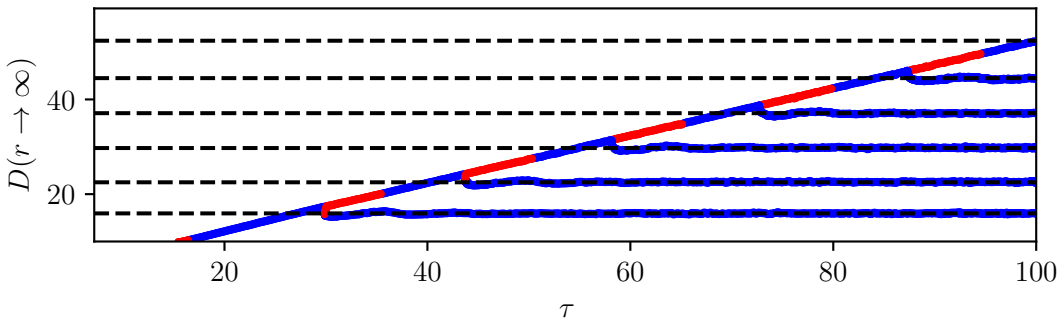

Figure 3.10: Continuation in τ of branches of periodic solutions containing two LSs at different distances $D(r \to \infty)$ for the parameters $\Delta = 0.49$, $\psi = 2.1$ and $\chi = 0.99$. (Blue) Stable and (red) unstable parts are distinguished. (Black) The final distances, that are obtained from the DNSs of the DAE and given in table 3.1, are shown for a comparison.

the bifurcation points are not investigated further. The distance between the kinks of these branches is constant in the delay time τ and they are stable. A small oscillation of the distance between the kinks is observed in each of these branches if it is close to the branch at $D(r \to \infty) = \frac{T}{2}$. In this case, the branch at $D(r \to \infty) = \frac{T}{2}$ is unstable. Figure 3.10 also indicates that the general observation, of one branch being at $D(r \to \infty) = \frac{T}{2}$ and additional ones existing well separated in the distance between the kinks with $D(r \to \infty) < \frac{T}{2}$, is independent of the delay time τ and continues for $\tau > 100$. Additional unstable branches might exist between – in terms of the distance $D(r \to \infty)$ – the displayed stable branches, but as the stable branches are of more interest for possible applications, these are not explored.

4. DAE with Periodic Potential

Synchronization between a periodic potential and multiple LSs in periodic solutions is observed experimentally for the corresponding PDE with periodic potential [Gar+17]. It is a promising property for applications in optical communication networks as it presents an opportunity to control the multiple LSs inside one domain. For such applications the impact of the potential on a LS in a periodic solution and the observed phenomena of synchronization needs to be understood. A detailed analysis from a theoretical and numerical point of view was not performed yet.
The following chapter investigates how the additional external periodic potential influences the dynamics of the system, especially of solutions containing one LS, from a theoretical and numerical point of view. The impact of the potential on the steady states is discussed. Additionally, the trapping of LSs by the potential, that is observed in [Gar+17], is explored in detail for periodic solutions which contain one kink. The conditions and borders of this kind of synchronization is analyzed. Moreover, the influence on the position of the LS with respect to the minima of the potential is examined as the periodic potential might be a tool to control the dynamics of LSs. Moreover, the investigation is extended to periodic solutions containing two LSs.

4.1. Extended Model Equation

The periodic potential is added to eq. (2.1) in a similar way as to the corresponding PDE in [Gar+17]. The DAE with periodic potential reads

$$\frac{d\theta}{dt} = \Delta - \sin\left(\theta + A\cos\left(\omega t\right)\right) + \chi \sin\left(\theta_\tau - \theta - \psi\right). \tag{4.1}$$

The periodic potential of amplitude A and frequency ω is given by $\varphi(t) = A\cos(\omega t)$ resulting in the period $T = \dfrac{2\pi}{\omega}$. The latter is used as the folding parameter $\tilde{T} = T$ for the visualization in the co-moving reference frame in the following. The other parameters correspond to the parameters in eq. (2.1) and are explained in section 2.6.1. The periodic potential vanishes for amplitude $A = 0$ and the DAE as written in eq. (2.1) is reobtained. The DAE with periodic potential is a non-autonomous DDE, since the potential depends directly on the independent variable t. The continuation tool `DDE-BIFTOOL`, however, requires the investigated system to be autonomous. Therefore, the DAE with periodic potential is written as an autonomous system using the variable $z = \omega t$. Additionally, the variable z_0 and an extra condition is introduced for the analysis of the system with `DDE-BIFTOOL` to obtain a stationary periodic potential. This means that the first value of the profile in each point of a branch corresponds to the value of the periodic potential

$\varphi = A$. All in all, the equivalent system used for the analysis with `DDE-BIFTOOL` reads

$$\begin{aligned} \frac{d\theta}{dt} &= \Delta - \sin\left(\theta + A\cos\left(z - z_0\right)\right) + \chi\sin\left(\theta_\tau - \theta - \psi\right) \\ \frac{dz}{dt} &= \omega \end{aligned} \tag{4.2}$$

where $z - z_0 \overset{!}{=} 0$ for the first value of the profile in each periodic solution.

4.2. From Steady States to Quasi-Steady-States

Equation (2.13) is a necessary condition for steady states which is not fulfilled for any set of parameters for the DAE with periodic potential, due to the continuous changing potential in time. However, if the phase θ changes fast compared to the potential φ, it is assumed that the system undergoes its changes in the phase θ due to the evolving potential φ by passing by the equilibrium states of the system for each value of the potential φ as in thermodynamics. Resulting in a phase $\theta(t)$ at time t which corresponds to a steady state of the same system, but with a potential of a constant value $\varphi(t) = \varphi_c =$ const. This state of the system will be called quasi-steady-state. The condition for the steady states in eq. (2.13) holds for each quasi-steady-state where the potential is set to a constant value $\varphi(t) = \varphi_c =$ const. For a vanishing potential of no amplitude A the quasi-steady-states correspond to the steady states of the DAE written in eq. (2.1). As long as the phase θ follows the relatively slow potential φ immediately, the system passes infinitely many of those quasi-steady-states. The parameter sets in this investigation hold the condition of a relatively slow potential which is called quasi-steady-state-limit. At a later point, the definition of a distance $0 \leq d \leq \pi$ between steady states $\theta_{s,u}$ determined in section 2.6.2 will turn out as a useful quantity. Hence, it is introduced as

$$\begin{aligned} d &= \min\left(\left|\theta_s - \theta_u\right|\right) \\ &= \begin{cases} \pi + 2\arcsin\left(\Delta - \chi\sin\left(\psi\right)\right) & \text{for} \quad \Delta - \chi\sin\left(\psi\right) \in [-1, 0] \\ \pi - 2\arcsin\left(\Delta - \chi\sin\left(\psi\right)\right) & \text{for} \quad \Delta - \chi\sin\left(\psi\right) \in [0, 1] \end{cases} \end{aligned} \tag{4.3}$$

4.2.1. Without Feedback $\chi = 0$

The periodic potential $\varphi(t)$ can be replaced by the constant value φ_c in the quasi-steady-state-limit. Applying eq. (2.13) as the condition for quasi-steady-states in this limit to the DAE with periodic potential for $\chi = 0$ and $\varphi(t) = \varphi_c =$ const leads to the quasi-steady-states

$$\theta_{qs} = \arcsin\left(\Delta\right) - \varphi_c + 2\pi n \qquad n \in \mathbb{Z} \tag{4.4}$$

$$\theta_{qu} = \pi - \arcsin\left(\Delta\right) - \varphi_c + 2\pi n \qquad n \in \mathbb{Z}. \tag{4.5}$$

The quasi-steady-states which are passed by the system in one period of the potential are obtained by inserting different values of $\varphi_c \in [-A, A]$ to the equations. For this

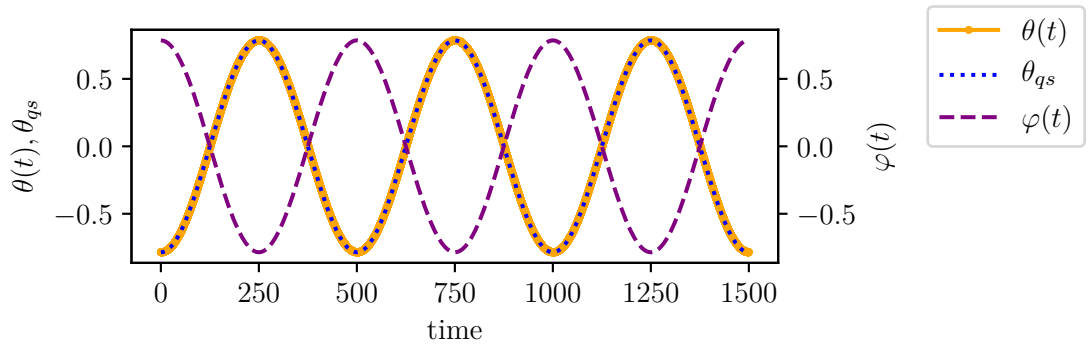

Figure 4.1: Result of a DNS for the parameter set: $\Delta = 0$, $\chi = 0$, $\psi = 0$, $\tau = 50$, $\epsilon = 1 \times 10^{-8}$, $A = \frac{\pi}{4}$ and $\omega = \frac{2\pi}{500}$. Time evolution of (orange) the phase $\theta(t)$, (blue) the quasi-steady-state θ_{qs} and (purple) the potential $\varphi(t)$ of the last three calculated periods. $\theta(t)$ oscillates with amplitude A and frequency ω in antiphase to the periodic potential $\varphi(t)$ around the corresponding stable steady state $\theta_s = 0$. $\theta(t)$ is sufficiently well described by the stable quasi-steady-state θ_{qs} given by eq. (4.4) at the corresponding time. This parameter set is clearly in the quasi-steady-state limit.

reason the quasi-steady-states θ_{qs} and θ_{qu} oscillate with amplitude A and frequency ω in antiphase to the periodic potential around the corresponding steady state θ_s or θ_u obtained with eq. (2.53) or eq. (2.54) (without periodic potential), respectively. The results of the DNS presented in fig. 4.1 show that the oscillation of $\theta(t)$ follows the quasi-steady-state θ_{qs}. Therefore, a period $T = 500$ of the potential is in the quasi-steady-state limit. The shorter the period of the potential T becomes, the faster evolves the potential. Hence, the phase $\theta(t)$ follows the quasi-steady-states with an increasing delay and decreasing amplitude for decreasing periods T. At one point the approximation that the system passes its equilibrium states holds no longer because the phase $\theta(t)$ does not evolve fast enough anymore. The system is not in quasi-steady-state limit beyond that point.

A tiny delay between θ_{qs} and $\theta(t)$ is indicated in fig. 4.2. Nevertheless, $\theta(t)$ is still sufficiently well described by the stable quasi-steady-state θ_{qs} for $T = 50$. This value for the period is mainly used in the following results, where the approximation that $\theta(t)$ follows the states of θ_{qs}, given by eq. (4.4), applies.

The increasing delay between $\theta(t)$ and θ_{qs} is illustrated in fig. 4.3 for the period of the potential $T = 1$. $\theta(t)$ and the quasi-steady-states are oscillating with the frequency ω of the potential. However, the oscillation of $\theta(t)$ is almost $\frac{\pi}{2}$ behind the oscillation of the quasi-steady-states and its amplitude is smaller. Therefore, an approximation of the oscillation of $\theta(t)$ through the stable quasi-stable-state is not useful for periods of the potential of the magnitude $T \approx 1$ or less.

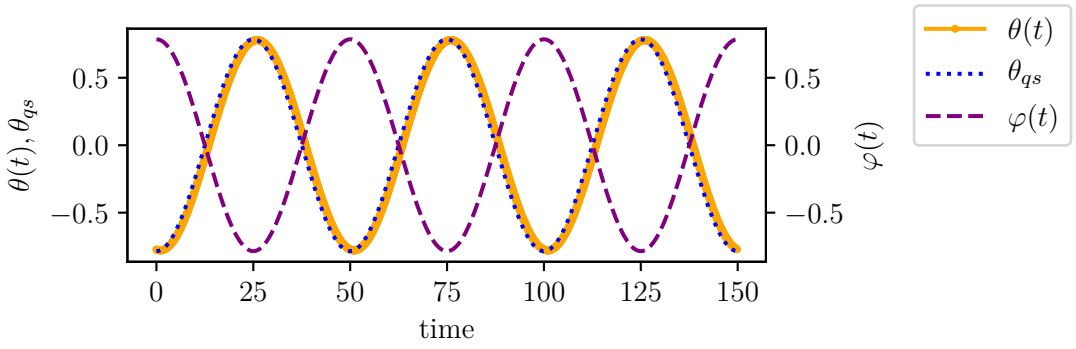

(a) time evolution

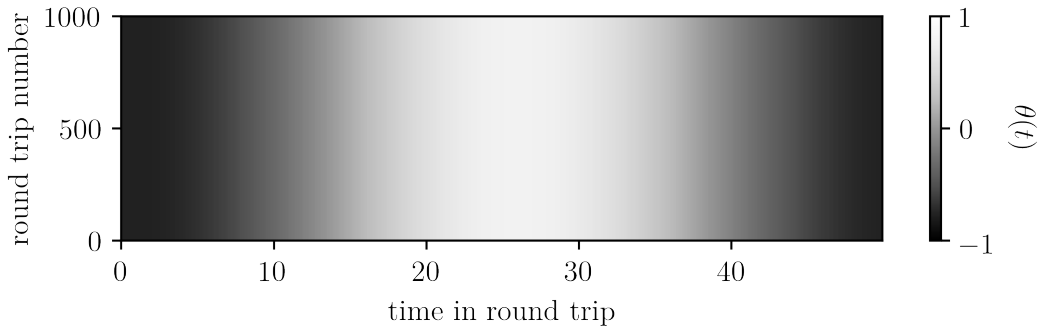

(b) co-moving reference frame

Figure 4.2: Result of a DNS for the parameter set: $\Delta = 0$, $\chi = 0$, $\psi = 0$, $\tau = 50$, $\epsilon = 1 \times 10^{-8}$, $A = \frac{\pi}{4}$ and $\omega = \frac{2\pi}{\tau} = \frac{2\pi}{50}$. (a) Time evolution of (orange) the phase $\theta(t)$, (blue) the quasi-steady-state θ_{qs} and (purple) the potential $\varphi(t)$ of the last three calculated periods. (b) Co-moving reference frame with respect to the period $T = 50$. Note that $\theta(t)$ is plotted as the grey scale instead of $\cos(\theta)$. $\theta(t)$ oscillates with amplitude A and frequency ω in antiphase to the periodic potential $\varphi(t)$ around the corresponding stable steady state $\theta_s = 0$. Despite a tiny delay between $\theta(t)$ and θ_{qs}, $\theta(t)$ is still sufficiently well described by the stable quasi-steady-state θ_{qs} given by eq. (4.4) at the corresponding time. This parameter set is close to the edge of the quasi-steady-state limit.

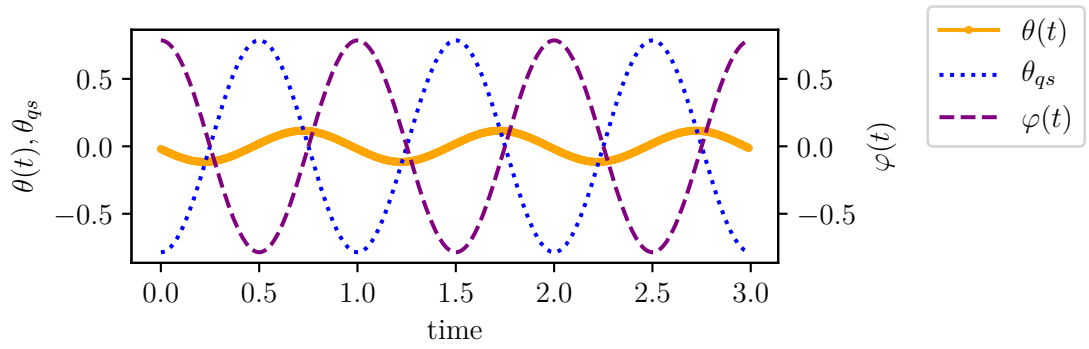

Figure 4.3: Result of a DNS for the parameter set: $\Delta = 0$, $\chi = 0$, $\psi = 0$, $\tau = 50$, $\epsilon = 1 \times 10^{-8}$, $A = \frac{\pi}{4}$ and $\omega = \frac{2\pi}{1}$. Time evolution of (orange) the phase $\theta(t)$, (blue) the quasi-steady-state θ_{qs} and (purple) the potential $\varphi(t)$ of the last three calculated periods. $\theta(t)$ oscillates with amplitude A and frequency ω but not antiphase to the periodic potential $\varphi(t)$ around the corresponding stable steady state $\theta_s = 0$. $\theta(t)$ is not described by the stable quasi-steady-state θ_{qs} given by eq. (4.4) at the corresponding time. This parameter set is not in the quasi-steady-state limit.

4.2.2. With Feedback $\chi \neq 0$

Similar to the previous calculations for $\chi = 0$, eq. (2.13) is applied as the condition for quasi-steady-states in the quasi-steady-state limit ($\varphi(t) = \varphi_c = \text{const}$) to the DAE with periodic potential. Additionally, $\theta(t-\tau)$ can be approximated by $\theta(t)$ for $nT \approx \tau$ where $n \in \mathbb{N}$. This results in the quasi-steady-states

$$\theta_{qs} = \quad + \arcsin\left(\Delta - \chi \sin\left(\psi\right)\right) - \varphi_c + 2\pi n = \theta_s - \varphi_c \qquad n \in \mathbb{Z} \tag{4.6}$$

$$\theta_{qu} = \pi - \arcsin\left(\Delta - \chi \sin\left(\psi\right)\right) - \varphi_c + 2\pi n = \theta_u - \varphi_c \qquad n \in \mathbb{Z}. \tag{4.7}$$

Figure 4.4 illustrates the results of a DNS for the same parameter set as fig. 4.2 but with feedback $\chi = 1$.

Nevertheless, the results are similar. $\theta(t)$ follows the states of θ_{qs} given by eq. (4.6). The distance $d_q = \min\left(|\theta_{qs} - \theta_{qu}|\right) = \min\left(|\theta_s - \varphi_c - \theta_u + \varphi_c|\right) = \min\left(|\theta_s - \theta_u|\right) = d$ between the quasi-steady-states is identical to the distance between the steady states which is defined in eq. (4.3), because the quasi-steady-states are parallel to each other for different values of φ_c. This is also shown in fig. 4.4. The stability of the quasi-steady-states is calculated in the following section.

4.2.3. Stability of Quasi-Steady-States

Since the quasi-steady-states are calculated similarly to steady states with the approximations of the quasi-steady-state limit, their stability is investigated by a linear stability analysis as well. Therefore, the stability of the quasi-steady-states is determined by λ

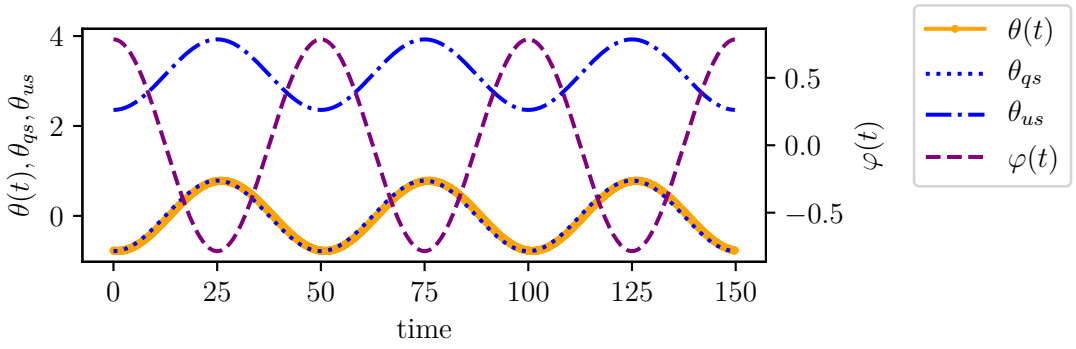

(a) time evolution

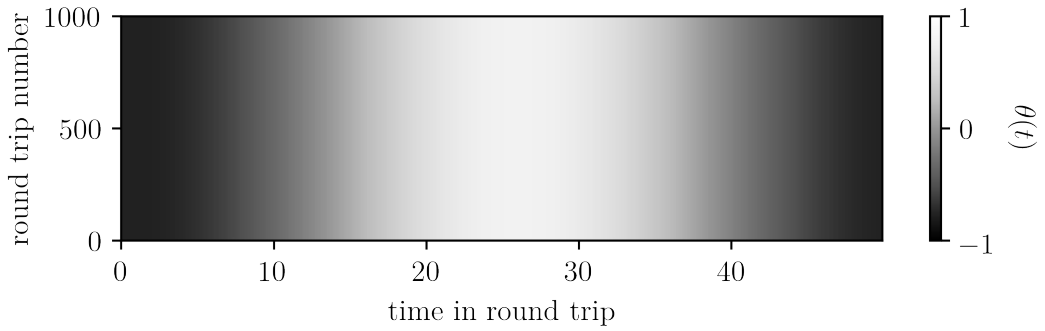

(b) co-moving reference frame

Figure 4.4: Result of a DNS for the parameter set: $\Delta = 0$, $\chi = 1$, $\psi = 0$, $\tau = 50$, $\epsilon = 1 \times 10^{-8}$, $A = \frac{\pi}{4}$ and $\omega = \frac{2\pi}{\tau}$. (a) Time evolution of (orange) the phase $\theta(t)$, (blue) the quasi-steady-state (dashed) θ_{qs} and (dashdotted) θ_{qu} and (purple) the potential $\varphi(t)$ of the last three calculated periods. (b) Co-moving reference frame with respect to the period $T = 50$. Note that $\theta(t)$ is plotted as the grey scale instead of $\cos(\theta)$. $\theta(t)$ oscillates with amplitude A and frequency ω in antiphase to the periodic potential $\varphi(t)$ around the corresponding stable steady state $\theta_s = 0$. Despite a tiny delay between $\theta(t)$ and θ_{qs}, $\theta(t)$ is still sufficiently well described by the stable quasi-steady-state θ_{qs} given by eq. (4.6) at the corresponding time. This parameter set is close to the edge of the quasi-steady-state limit.

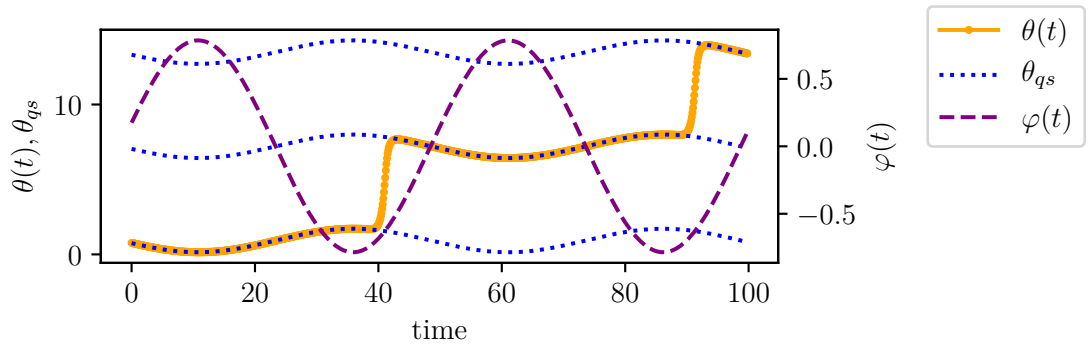

Figure 4.5: Result of a DNS for the parameter set: $\Delta = 0.8$, $\chi = 3.5$, $\psi = 0$, $\tau = 50$, $\epsilon = 0$, $A = \frac{\pi}{4}$ and $\omega = 0.12502$. A 1-kink-solution is used as initial condition. Time evolution of (orange) the phase $\theta(t)$, (blue) the quasi-steady-state θ_{qs} and (purple) the potential $\varphi(t)$ of the last two calculated periods. $\theta(t)$ can be split up into a background and a 2π-shift. The background oscillates accordingly to the stable quasi-steady-state θ_{qs} given by eq. (4.6). The 2π-shift is a LS – also called kink – which exists on the background. Each of the plotted θ_{qs} at a given time corresponds to the same value due to the 2π-periodicity of the phase space.

which is defined in eq. (2.17) via the constants

$$A = -\cos(\theta_{qs,qu} + \theta_c) - \chi\cos(\psi) = -\cos(\theta_{s,u}) - \chi\cos(\psi)\,, \tag{4.8}$$

$$B = \chi\cos(\psi)\,. \tag{4.9}$$

They are obtained by applying eq. (2.18) and eq. (2.19), respectively to eq. (4.1) where the potential is approximated by a constant $\varphi(t) = \varphi_c$ in the quasi-steady-state limit. The constants A and B are identical to the constants determined for the steady states in eq. (2.56) and eq. (2.57), respectively. Hence, the stability of the quasi-stable-states $\theta_{qs,qu}$ corresponds to the stability of the steady states $\theta_{s,u}$. This fits to the previous shown results that $\theta(t)$ is following θ_{qs}.
The oscillation of $\theta(t)$ accordingly to stable quasi-steady-state θ_{qs} builds the background for the kink solutions of the DAE with periodic potential especially for lower amplitudes A. An example is illustrated in fig. 4.5. $\theta(t)$ is a superposition of the stable quasi-steady-state θ_{qs} and a repeating 2π-shift. The oscillation described by the stable quasi-steady-state may be regarded as the background on which the kink exists. This raises the question on conditions for the existence of kink solutions on the oscillating background which is the topic of the following section.

4.3. Conditions for the Existence of Kinks

As mentioned in the beginning of this chapter, this thesis analyzes the dynamics of kinks produced by the DAE with a periodic potential. Conditions for the existence of stable 1-kink-solutions which have the same period $T = \frac{2\pi}{\omega} \approx \tau$ as the potential are

investigated. 1-kink-solutions are solutions which contain one 2π-shift in a time domain of the approximated length τ or mathematically, solutions which meet the condition $|\theta(t-\tau-\delta)-\theta(t)| = 2\pi$ where $|\delta| \ll 1$. The parameter sets used for the investigation of the DAE with periodic potential are in the region $T \approx \tau = 50$ where the approximations of the quasi-steady-state limit hold and where the background follows the stable quasi-steady-state θ_{qs}, as observed in section 4.2.1.
The main question for the existence of a kink is whether the kink survives several round trips. In other words, does a 2π-shift which comes from the feedback loop produce another 2π-shift also known as another excitation of the system. Therefore, it is assumed that the feedback loop is a superposition of one 2π-shift and the oscillating background. As explained in section 2.2, the perturbation of a system needs to cross a well-defined threshold to excite the system. In the investigated system an excitation is a 2π-shift in the phase $\theta(t)$ and the threshold is a perturbation which kicks the phase $\theta(t)$ just further than the unstable steady (quasi-steady-)state. The phase $\theta(t)$ follows the stable quasi-steady-state θ_{qs} as observed in the previous section. For that reason, the threshold is a perturbation which kicks the phase $\theta(t) = \theta_{qs}$ by the value of the distance d_q between the stable and unstable quasi-steady-state. Thus, the constant distance $d_s = d$ which is calculated in eq. (4.3) is taken as a measure for the threshold at a given parameter set. The reason for the perturbation of the phase $\theta(t)$ which excites the system is the kink that is returning from the feedback loop. Its impact on the dynamics is described by the feedback term $\chi \sin(\theta_\tau - \theta - \psi)$. The assumption $\theta(t) \approx \theta(t-\tau)$ for $nT \approx \tau$ where $n \in \mathbb{N}$ made previously to obtain the quasi-steady-states holds, except from the point when $\theta(t-\tau)$ describes the returning LS, because $\theta(t-\tau)$ maps the whole phase space $[0, 2\pi]$ in a relatively short time compared to time delay τ. The argument of $\sin(\theta_\tau - \theta - \psi)$ also maps almost the whole phase space as a result. To sum up, $\sin(\theta_\tau - \theta - \psi)$ is almost constant expect when a kink is returning and it maps almost the whole interval $[-1, 1]$. This is independent of any parameter, in particular of ψ. The value of $\sin(\theta_\tau - \theta - \psi)$ is amplified by χ resulting the impact of a returning kink to scale with χ. For this reason, χ is a measure of the perturbation produced by a returning kink.
All in all, two measures are obtained. d for the threshold of the strength of the perturbation needed for the creation of a LS and χ as the strength of the perturbation produced by a returning kink. The greater the distance d, the greater the feedback strength χ needs to be in order for a kink to produce another kink and therefore survive. Note that the creation of a kink by a returning kink is also highly dependent on the profile of the returning kink. This must be taken into account when initial conditions are set for DNSs.
The dependency of the survival of a kink on the feedback strength d for a given parameter set and similar initial conditions is illustrated in fig. 4.6. The initial 2π-shift perturbs the phase $\theta(t)$, but not strong enough to produce another 2π-shift in fig. 4.6 (a) and (b). This perturbation fades away in a few round trips taking more time for higher feeback strength χ. The kink dies for $\chi = 1.5$ and $\chi = 2.0$. In fig. 4.6 (c) each from

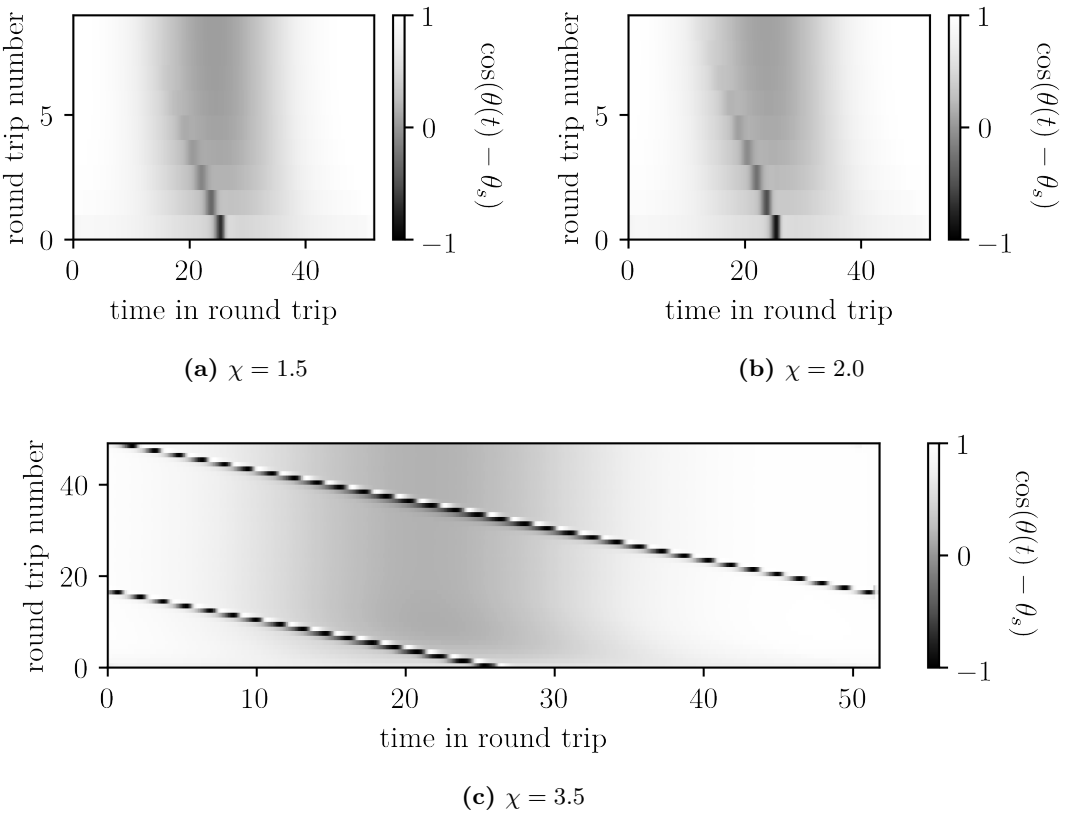

(a) $\chi = 1.5$

(b) $\chi = 2.0$

(c) $\chi = 3.5$

Figure 4.6: Result of a DNS with an initial condition which contains one 2π-shift for the parameter set: $\Delta = 0.1$, $\psi = 0$, $\tau = 50$, $\epsilon = 0$, $A = \frac{\pi}{4}$ and $\omega = 0.121$. Note that a 2π-shift in the co-moving reference frame corresponds to passage from grey to grey via black and white. (a), (b) The 2π-shift in the initial condition is not producing a 2π-shift in the first round trip but a perturbation which decreases with every round trip until fades away. This process takes a few more round trips in (b) compared to (a). (c) The 2π-shift in the initial condition excites the system and is therefore producing another 2π-shift which excites the system again leading to a surviving kink.

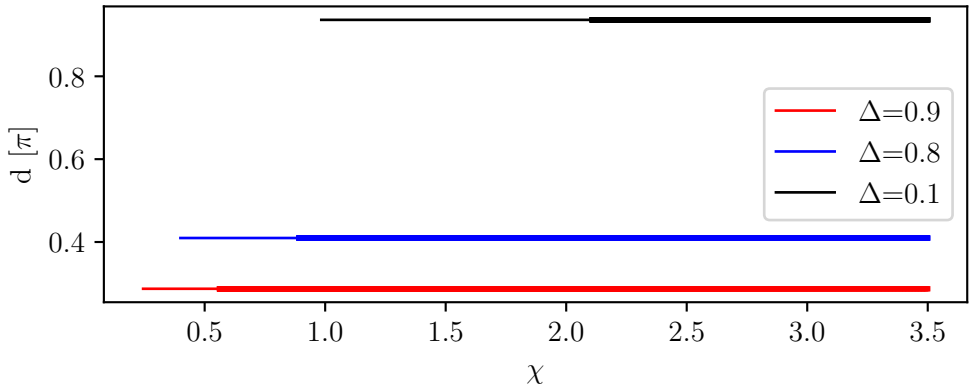

Figure 4.7: Bifurcation diagram of a two parameter continuation in χ and ω (and z_0) of a fold bifurcation of a periodic 1-kink-solution for the parameter set: $\psi = 0$, $\tau = 50$ and $A = \frac{\pi}{4}$. These fold bifurcation are introduced in detail in section 4.4.2. Thick lines correspond to a bifurcation between a stable and unstable solution and thin lines to a bifurcation between two unstable solutions indicating the feedback strength χ which is necessary to obtain a stable periodic 1-kink-solution at the given detuning Δ which corresponds to the distance of the quasi-steady-states d given by eq. (4.3).

the feedback loop returning kink perturbs the system above the necessary threshold and creates another 2π-shift. Hence, the kink survives.
Different parameter sets with surviving kinks are observed in the results of DNSs. The obtained 1-kink-solutions are then further investigated using `DDE-BIFTOOL` as explained in detail in the following sections. Fold bifurcations between stable and unstable periodic 1-kink-solutions are found. Those bifurcations are continued in χ and ω. The results are visualized in fig. 4.7. The thick lines correspond to bifurcations between a stable and an unstable periodic 1-kink-solution and the thin lines to a bifurcations between two unstable periodic 1-kink-solutions. The transition points between the thin and thick lines indicate the feedback strength χ which is necessary to obtain a stable solution with a surviving kink. The results shown in fig. 4.7 support the previously mentioned dependency of the survival of a kink on the values for the feedback strength χ and the distance between the quasi-steady-states d. The greater the distance d the greater the necessary feedback strength χ for the creation of a 2π-shift by a returning kink from the feedback loop.

4.4. Region of Synchronization and Arnold Tongue

The previous sections explain the modifications of the background of kink solutions and conditions for the existence of kink solutions due to the additional periodic potential. The following section focuses on the dynamics of 1-kink-solutions inside the periodic potential. As an example the parameter set $\Delta = 0.8$, $\chi = 3.5$, $\psi = 0$, $\tau = 50$ is used. Different parameter sets are investigated afterwards.

4.4.1. Synchronization of 1-Kink-Solutions and Periodic Potential

The results of the DNSs at different values of ω at $A = \frac{\pi}{4}$ illustrated in fig. 4.8 indicate qualitatively different types of 1-kink-solutions in a periodic potential. The length of each round trip corresponds to the period of the periodic potential T leading to a stationary potential. As a result, the oscillation of the background is stationary as well as it follows the quasi-steady-states which is explained in section 4.2. The simulations in (a) and (d) represent solutions of a kink which travels with respect to the potential. This is a qualitative difference to the simulations (b) and (c) which display stationary kinks with respect to the potential. The kinks in the latter two simulations are travelling to a specific position inside the potential in the beginning of the time evolution and remain at that position. They are trapped inside the potential. The simulation at the same parameter set but without periodic potential is illustrated in fig. 4.9. The initial frequency of this periodic solution is found at $\omega_0 \approx 0.125015$ which is greater than the frequencies in fig. 4.8 (a) and (b) but less than the frequencies in (c) and (d). In fact, these frequencies are symmetrically distributed around ω_0. The kinks in the solutions with a potential of a frequency which differs by $|\omega - \omega_0| \approx 5 \times 10^{-6}$ are trapped in the potential. The kinks in the other solutions where the frequency of the potential differs by $|\omega - \omega_0| \approx 15 \times 10^{-6}$ are not trapped. The periodic potential seems to synchronize the frequency of the 1-kink-solution to its own frequency ω if the frequency of the potential is in a certain interval close to the frequency ω_0. Hence, the condition for synchronization may be written as

$$\omega \in [\omega_0 - \delta_-, \omega_0 + \delta_+] \tag{4.10}$$

where δ_- and δ_+ are constants determined later. The borders of the phenomena of synchronization between 1-kink-solutions and the periodic potential are further investigated in the following section. The position of the kink with respect to the potential in the synchronized cases seem to depend on ω since the kink is at the left side of the minimum of the potential in fig. 4.8 (b) and at the right side in fig. 4.8 (c). The position of the kinks with respect to the potential is also discussed in the next sections.
Furthermore, it is found that kinks of solutions with a frequency $\omega < \omega_0 - \delta_-$ of the potential are travelling to left and kinks of solutions with a frequency $\omega > \omega_0 + \delta_+$ are travelling to the right. The velocity of the kinks with respect to the stationary potential is not constant. However, the kinks move faster once they are close to the maximum of the potential. This can also be seen in fig. 4.8. Moreover, the number of round trips a kink needs until it travelled trough a potential depends on the difference between the frequency of the potential and the border of the interval $[\omega_0 - \delta_-, \omega_0 + \delta_+]$. The greater the distance the less round trips are necessary for the kink to pass a potential. This is shown by the comparison of fig. 4.8 (a) and (d) to fig. 4.10 (a) and (b).

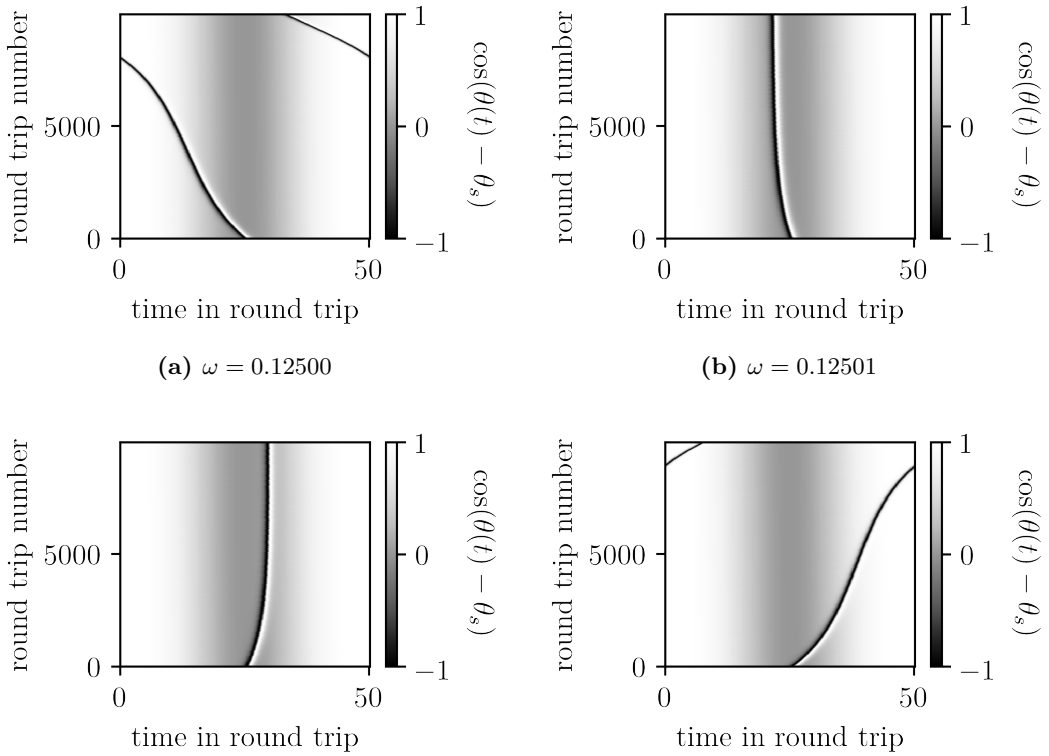

(a) $\omega = 0.12500$ **(b)** $\omega = 0.12501$

(c) $\omega = 0.12502$ **(d)** $\omega = 0.12503$

Figure 4.8: Results of a DNS with an initial condition which contains one 2π-shift for the parameter set: $\Delta = 0.8$, $\chi = 3.5$, $\psi = 0$, $\tau = 50$, $\epsilon = 0$ and $A = \frac{\pi}{4}$. The length of each round trip corresponds to the period of the periodic potential T. Thus, the potential and the oscillation of the background corresponding to the stable quasi-steady-state θ_{qs} are stationary in those figures and the position of the kink is regarded with respect to those. The kinks are travelling (a) to the left and (d) to the right from one potential minima to the next. The kinks are not trapped inside one potential minima. The kinks are moving to a specific position (b) at the left and (c) at the right side of one minima of the potential in the beginning of the time evolution and remain at that position. Those kinks are trapped inside the potential. The last part of the time evolution of (c) is also illustrated in fig. 4.5.

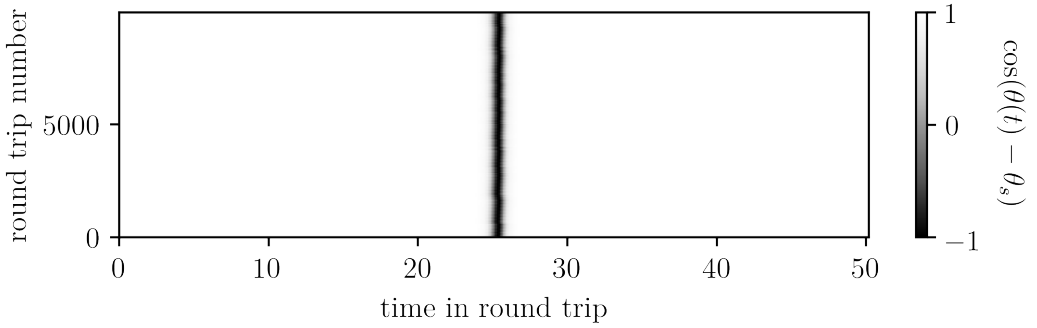

Figure 4.9: Result of a DNS with an initial condition which contains one 2π-shift for the parameter set: $\Delta = 0.8$, $\chi = 3.5$, $\psi = 0$, $\tau = 50$, $\epsilon = 0$ and $A = 0$. The parameters are identical to those in fig. 4.8, but the amplitude of the periodic potential is 0. The period $T \approx 50.2594$ of this solution is calculated via an autocorrelation and it corresponds to a frequency $\omega_0 \approx 0.125015077$.

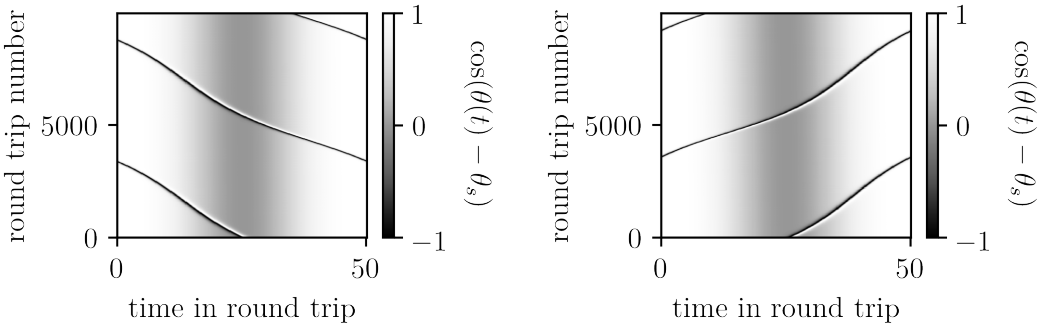

(a) $\omega = 0.12499$ **(b)** $\omega = 0.12504$

Figure 4.10: Results of a DNS with an initial condition which contains one 2π-shift for the parameter set: $\Delta = 0.8$, $\chi = 3.5$, $\psi = 0$, $\tau = 50$, $\epsilon = 0$ and $A = \frac{\pi}{4}$. The length of each round trip corresponds to the period of the periodic potential T. Thus, the potential and the oscillation of the background corresponding to the stable quasi-steady-state θ_{qs} are stationary in those figures. The position of the kink is regarded with respect to the potential. The kinks are travelling (a) to the left and (b) to the right from one potential minima to the next. The kinks are not trapped inside one potential minima.

4.4.2. Borders of Synchronization between 1-Kink-Solutions and Periodic Potential at Constant Amplitude

The phenomena of synchronization between 1-kink-solutions and the periodic potential is observed in the results of the DNSs in the previous section. Those results indicate that this phenomena is highly dependent on the frequency of the periodic potential. A condition for the synchronization at $A = \frac{\pi}{4}$ is given by eq. (4.10). The main interest is to find the edges of the synchronization region. The synchronized and therefore periodic 1-kink-solutions from the direct numerics are imported into `DDE-BIFTOOL` and a branch of periodic solutions is created. This branch is continued in the parameter ω with `DDE-BIFTOOL` by using the DAE in the form given in eq. (4.2). In the following, the position of a kink is defined with respect to the maxima of the periodic potential. Additionally, a relative mesh with respect to the period of the potential T is used since the frequency ω is varied throughout the investigation. Hence, the values of the position of LSs lie in the interval $[0, 1]$.

The result of the continuation is shown in fig. 4.11. The position of the kink is plotted against the continuation parameter ω in the upper figure. Note that the axis 'position of the kink' is periodic, i.e. the positions at 0 and 1 coincide. Two different – a stable and an unstable – periodic 1-kink-solutions exist at values for ω between $\omega_{\min} = \omega_1 \approx 0.125005$ and $\omega_{\max} = \omega_3 \approx 0.125025$ leading to $\delta_- = \omega_0 - \omega_{\min} \approx 1 \times 10^{-5}$ and $\delta_+ = \omega_{\max} - \omega_0 \approx 1 \times 10^{-5}$ from eq. (4.10). Especially $\delta_- \approx \delta_+$ is obtained indicating that the region of synchronization is symmetrical in ω. However, this symmetry is broken in the general case which is discussed later. The position of the kink depends on the value of ω. It seems like a continuous change in ω leads to a continuous change of the position of the kink for both solutions. The position of the kink of the stable solution is closer to the minimum of the periodic potential (at 0.5) than the position of the kink of the unstable solution. The stable and the unstable solution meet at the bifurcation points at $\omega_{\min}$ and $\omega_{\max}$. One of the calculated Floquet-multipliers leave the unit circle at 1 indicating a fold bifurcation of periodic solutions.

The bottom figure in fig. 4.11 illustrates four profiles θ of the 1-kink-solutions calculated by the continuation. The time axis is chosen relative to the period T such that the periodic potential looks identical for the different solutions. The black lines indicate the calculated position of the kink in the profile and corresponds to the position of the kink in the upper figure. The profiles look very similar. The background oscillates accordingly to the stable quasi-steady-state as explained in section 4.2. The LS exists on that background. The profiles differ in the position of the kink. There is no further noticeable qualitative difference between the stable (solution 2) and the unstable solution (solution 4) besides the position of the kink and their stability. As already mentioned, the kink in the stable solution is closer to the minimum of the potential. The parameter sets of the solution 2 and 4 correspond to the parameter sets of the results of the DNS which are presented in fig. 4.8(c) and fig. 4.5. Since DNSs end on stable attractors

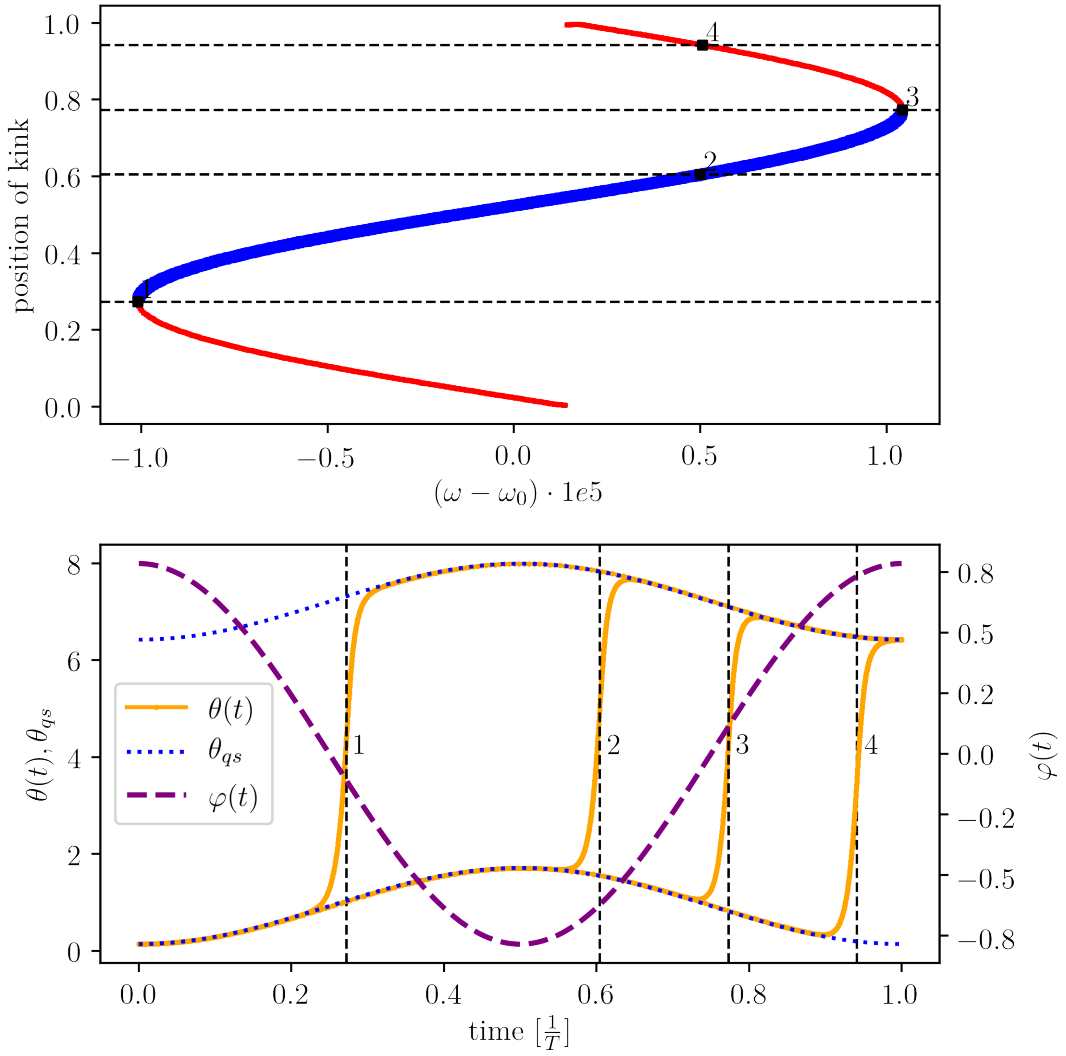

Figure 4.11: Continuation in ω (and z_0) of periodic 1-kink-solutions for the parameter set: $\Delta = 0.8$, $\chi = 3.5$, $\psi = 0$, $\tau = 50$ and $A = \frac{\pi}{4}$. The upper figure illustrates the position of the kinks versus the continuation parameter ω. The thin red lines correspond to an unstable and the thick blue lines to a stable solution. $\omega_0 \approx 0.125015$ is chosen as an offset. The profiles of the phase θ of four different periodic solutions at $\omega_1 \approx 0.1250049071$, $\omega_{2,4} \approx 0.12502$ and $\omega_3 \approx 0.1250254253$ are shown in the bottom figure as examples. The dotted black lines in both figures correspond to the position of the kink at the corresponding periodic 1-kink-solution. The periodic solution 2 corresponds to the results presented in fig. 4.8(c) and fig. 4.5 which are calculated via DNS.

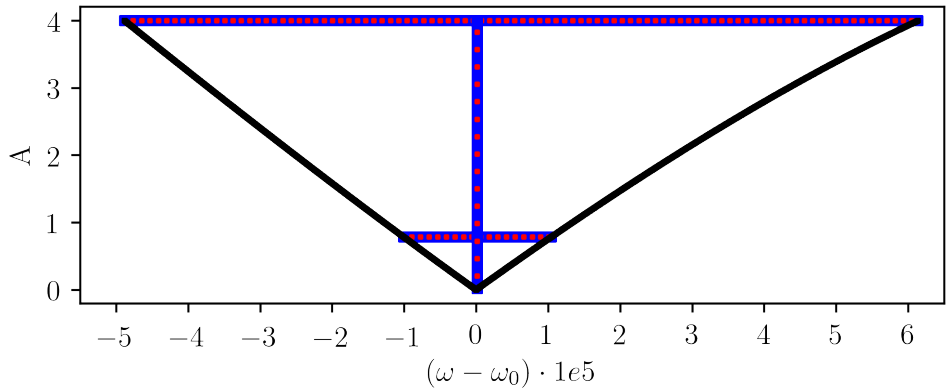

Figure 4.12: Continuation in the $A-\omega-$plane of (black) fold bifurcations of periodic solutions and (blue and red corresponding to their stability) periodic 1-kink-solutions continued in ω (and z_0) at $A = \frac{\pi}{4}$ and $A = 4$ and in A (and z_0) at $\omega \approx 0.125015$ for the parameter set: $\Delta = 0.8$, $\chi = 3.5$, $\psi = 0$ and $\tau = 50$. The offset $\omega_0 \approx 0.125015$ is chosen. Synchronized solutions exist between the fold bifurcations. This region is called Arnold tongue.

only, those previous results should correspond to solution 2. Comparing the position of the kink at 0.6 to fig. 4.8(c) and the whole profile to fig. 4.5 actually shows that those solutions correspond to each other. This supports the previous results and that both numerical methods are initialized correctly.

4.4.3. Borders of Synchronization between 1-Kink-Solutions and Periodic Potential

In the previous section, the region of synchronization at $A = \frac{\pi}{4}$ is investigated. The region of synchronization in the $A-\omega-$plane is obtained as a next step. Hence, the fold bifurcations, which are found at $\omega_{\min}$ and $\omega_{\max}$, are used to set up a branch of fold bifurcations of periodic solutions at both values. Those branches are continued in the $A-\omega-$plane. Additionally, branches of periodic 1-kink-solutions are continued in ω at $A = 4$ and in A at $\omega \approx 0.125015$. All branches are shown in fig. 4.12. Synchronized 1-kink-solutions exist between the two fold bifurcations. Thus, those span a region of synchronization between the periodic potential and the 1-kink-solution. Such a region is called Arnold tongue. The theoretical background of the Arnold tongue is explained in section 2.3. The tongue is getting smaller for decreasing amplitude A until both fold bifurcations approximately meet at $A = 0$ and $\omega_0 \approx 0.125015$, which is the frequency of the 1-kink-solution not influenced by a potential. The corresponding result of the DNS is illustrated in fig. 4.9. The results of the continuation and the direct numerical integration fit to each other. As expected by Arnold tongues found in of other systems such as mechanics [PRK01], a dependency of the width of the tongue in ω on the amplitude of the potential A is found. This leads to the updated condition for synchronization

$$\omega \in [\omega_0 - \delta_-, \omega_0 + \delta_+] \quad \text{where} \quad \delta_- = \delta_-(A) \neq \delta_+ = \delta_+(A) \tag{4.11}$$

where the constants δ_- and δ_+ depend on the amplitude. The width of the Arnold tongue at a given amplitude A is given by

$$w(A) = \delta_-(A) + \delta_+(A). \tag{4.12}$$

For the investigated parameter set $w(A_1) > w(A_2)$ is obtained for $A_1 > A_2$ which is convenient with respect to the mechanical picture of a particle in a potential. The stronger the potential the broader the region of synchronization. Hence, in this case the stronger the potential the wider the interval $[\omega_0 - \delta_-, \omega_0 + \delta_+]$ where the potential synchronizes the frequency of the 1-kink-solution to its own.
The offset $\omega_0 = 0.125015$ in fig. 4.12 is chosen to point out the broken left-right-symmetry of the Arnold tongue in ω resulting in $\delta_-(A) \neq \delta_+(A)$. Usually, Arnold tongues are symmetrical with respect to the frequency of the potential [PRK01]. A first hypothesis is that the symmetry breaking occurs due to the temporal aspect of the system because of the time delay which also leads to a symmetry breaking in the profile of the phase θ of a kink.
Figure 4.12 indicates that a stable and an unstable solution exists inside the Arnold tongue for this parameter set. For a better visualization, a 3D-plot showing the axis A, ω and the position of the kink of the already displayed branches is presented in fig. 4.13. Additionally, the A-position-plane of the same branches is illustrated in fig. 4.14. Note that the axis 'position of the kink' is periodic, i.e. the positions at 0 and 1 coincide in both figures.
Those figures show that two periodic 1-kink-solutions coexist inside the Arnold tongue. The branch of periodic solutions continued in ω at $A = 4$ is very similar in the position$-$ $\omega-$plane to the branch at $A = \frac{\pi}{4}$ which is already discussed previously. This leads to the hypothesis that the stability and the position of the kink of a 1-kink-solution at an arbitrary $0 < A < 4$ and $\omega_0 - \delta_-(A) < \omega < \omega_0 + \delta_+(A)$ could be obtained by interpolation out of the presented figures.
Especially fig. 4.14 illustrates that the position of the kink is independent of the amplitude of the potential A if ω does correspond to value such that the parameter set is not in the vicinity of a fold bifurcation. In particular, the position of the kink at the fold bifurcation is constant in A. Therefore, an experimental scan through the Arnold tongue from $\omega < \omega_0 - \delta_-(A)$ to $\omega > \omega_0 + \delta_+(A)$ at any $0 < A < 4$ will lead to the following result. For $\omega < \omega_0 - \delta_-(A)$ the 1-kink-solution travels to the left. A synchronized 1-kink-solution is obtained for $\omega_0 - \delta_-(A) < \omega < \omega_0 + \delta_+(A)$ and the position of the kink changes from approximately 0.3 to approximately 0.8. After leaving the tongue for $\omega > \omega_0 + \delta_+(A)$ a 1-kink-solution which travels to the right is obtained. This behavior is independent of the amplitude. Hence, the impact of a variation in ω on the position of the kink depends on the width of the tongue $w(A)$ at the specific amplitude A. This results in increasing changes of the position of the kink the lower the amplitude A for a fixed variation in ω.

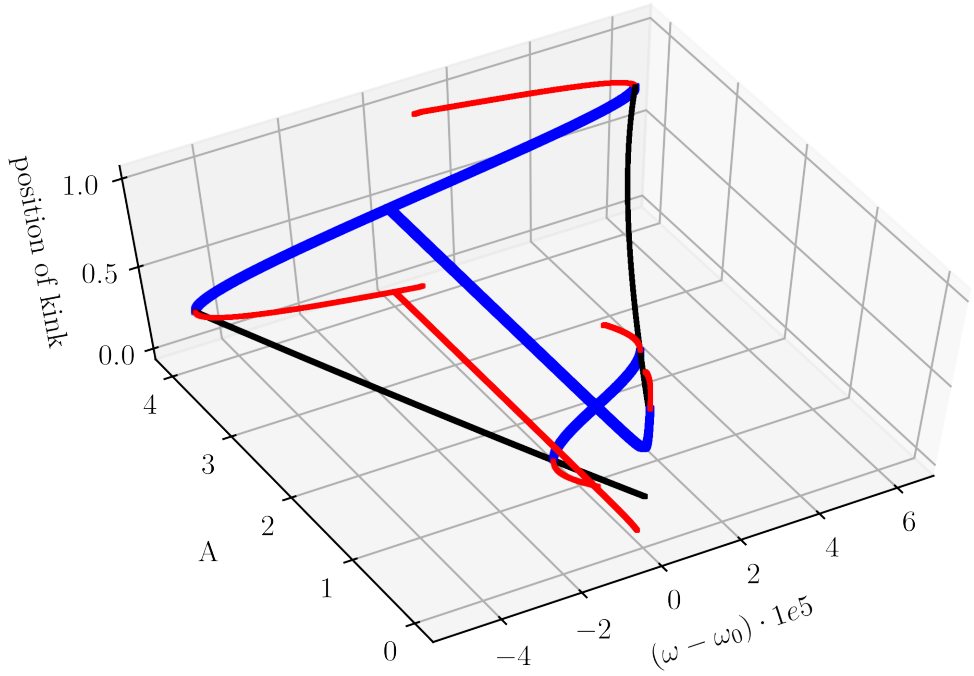

(a)

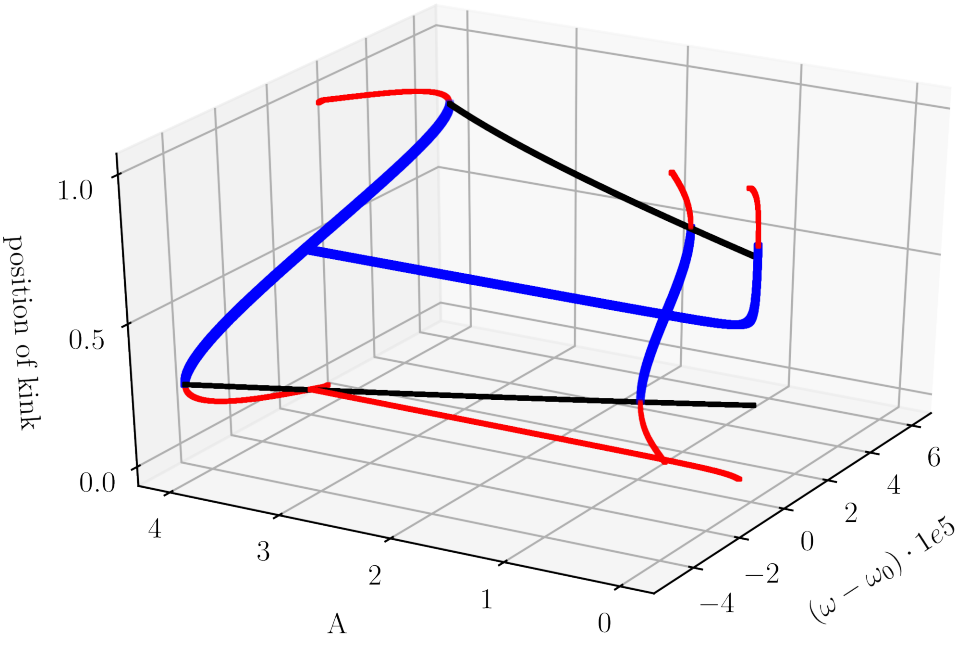

(b)

Figure 4.13: Continuation in the A-ω-position-space at different angles of (black) fold bifurcations of periodic solutions and (blue and red corresponding to their stability) in ω (and z_0) at $A = 4$ and in A (and z_0) at $\omega \approx 0.125015$ of 1-kink-solutions for the parameter set: $\Delta = 0.8$, $\chi = 3.5$, $\psi = 0$ and $\tau = 50$. The offset $\omega_0 \approx 0.125015$ is chosen. Note that the axis 'position of the kink' is periodic, i.e. the positions at 0 and 1 coincide.

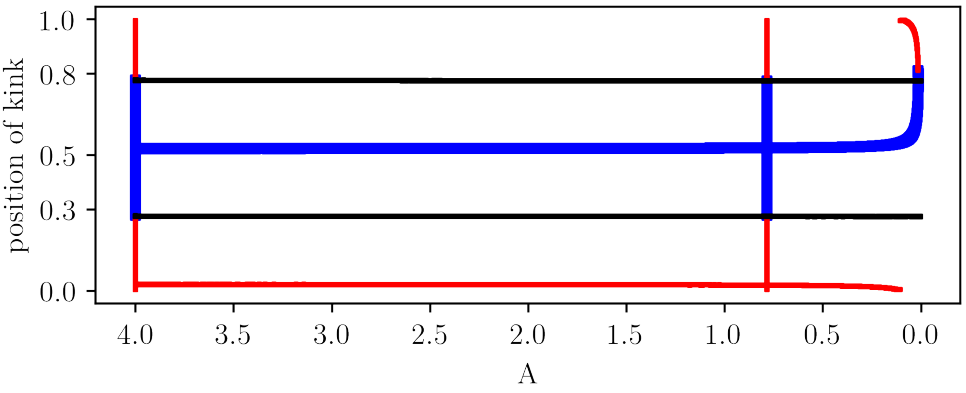

Figure 4.14: Continuation in the A-position-plane of (black) fold bifurcations of periodic solutions and (blue and red corresponding to their stability) in ω (and z_0) at $A = 4$ and in A (and z_0) at $\omega \approx 0.125015$ of 1-kink-solutions for the parameter set: $\Delta = 0.8$, $\chi = 3.5$, $\psi = 0$ and $\tau = 50$. The position of the kink does not depend on the amplitude. Note that the axis 'position of the kink' is periodic, i.e. the positions at 0 and 1 coincide.

The position of the kink is dependent on A for values of ω that correspond to values such that the parameter set is in the vicinity of a fold bifurcation. This is visualized in figs. 4.13 and 4.14 where A is close to 0. The position of the kink which is continued in A changes to the corresponding value of the fold bifurcation for A close to 0. The mismatch between the bifurcation point in that branch and the branch of the fold bifurcation occurs due to numerical effects in the region for low amplitude $A \approx 0$.

4.5. Arnold Tongues at Different Parameter Sets

The Arnold tongue at the parameter set $\Delta = 0.8$, $\chi = 3.5$, $\psi = 0$ and $\tau = 50$ is analyzed in detail in the previous section. Further Arnold tongues are calculated for different parameter sets. No Arnold tongue is obtained for $\Delta = 0.1$; $\chi = 2.0$ and $\Delta = 0.1$; $\chi = 1.0$ because a stable 1-kink-solutions cannot be obtained for those parameter sets as explained in section 4.3. An overview is given in fig. 4.15. All Arnold tongues show a similar overall structure. The tongues are bounded in ω by fold bifurcations. The overall shape of the tongues is triangular. The tongues are not symmetrical in ω. Two different 1-kink-solutions coexist inside the tongues. These effects are discussed in the previous section at the Arnold tongue at the parameter set $\Delta = 0.8$, $\chi = 3.5$, $\psi = 0$ and $\tau = 50$. The offsets in the frequency ω_0 are chosen as the frequency where the fold bifurcations meet at $A = 0$. Additionally, two more effects are found in some of the Arnold tongues – an open Arnold tongue and a period doubling bifurcation inside the tongue. Both of them are analyzed in the following sections. An additional section is dedicated to the Arnold tongues at $\chi = 1.0$ because the period doubling bifurcation reaches the region for small amplitudes. This is noticeable since low amplitudes $A \lesssim 0.5$ can be produced in experiments. Thus, the period doubling bifurcation may be observable in experiments. The offsets in the frequency ω_0, the width of the tongues at $A = \frac{\pi}{4}$ and $A = 4$ and the

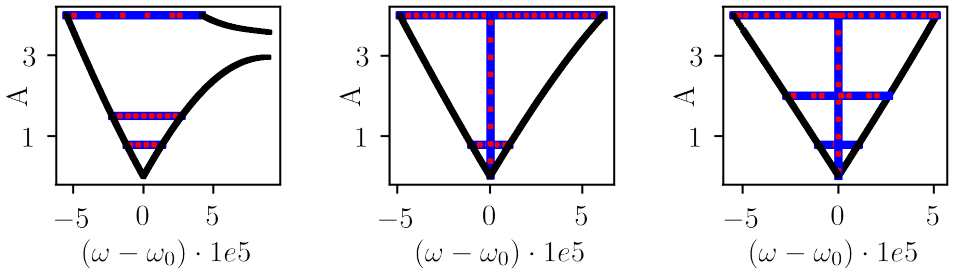

(a) $\Delta = 0.9$; $\chi = 3.5$

(b) $\Delta = 0.8$; $\chi = 3.5$

(c) $\Delta = 0.1$; $\chi = 3.5$

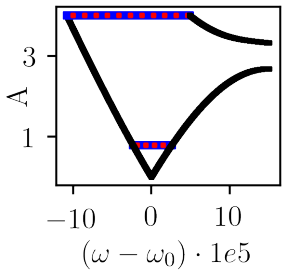

(d) $\Delta = 0.9$; $\chi = 2.5$

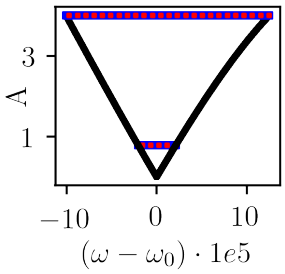

(e) $\Delta = 0.8$; $\chi = 2.5$

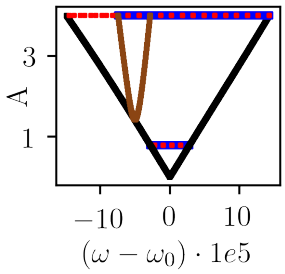

(f) $\Delta = 0.1$; $\chi = 2.5$

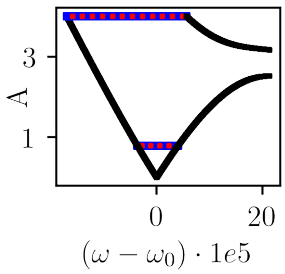

(g) $\Delta = 0.9$; $\chi = 2.0$

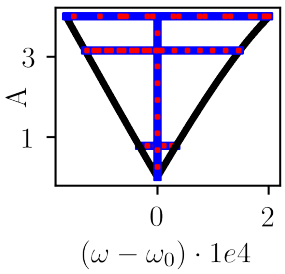

(h) $\Delta = 0.8$; $\chi = 2.0$

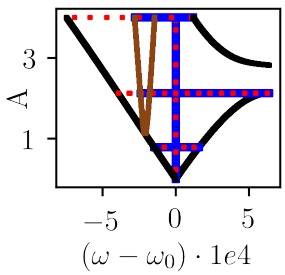

(i) $\Delta = 0.9$; $\chi = 1.0$

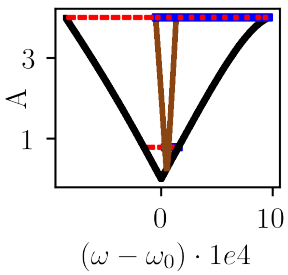

(j) $\Delta = 0.8$; $\chi = 1.0$

Figure 4.15: Overview of Arnold tongues at different parameters at constant $\psi = 0$ and $\tau = 50$. The chosen offset ω_0 for each parameter set is given in table 4.1. Black lines represent fold bifurcations of periodic orbits and brown lines period doubling bifurcations. Blue and red lines indicate periodic solutions which are stable or unstable respectively.

Table 4.1: Overview of the properties of the different Arnold tongues at $\psi = 0$ and $\tau = 50$ which are shown in fig. 4.15. The width $w(A)$ which is defined in eq. (4.12) is determined at $A = \frac{\pi}{4}$ and $A = 4$. ω_0 corresponds to the point where the fold bifurcations meet at $A = 0$. The distance d between the stable and unstable quasi-steady-state is also listed.

Δ	χ	ω_0	$w(A = \frac{\pi}{4})$	$w(A = 4)$	$d[\pi]$
0.9	3.5	0.12506297	2.55×10^{-5}	9.68×10^{-5}	0.29
0.9	2.5	0.12483139	4.93×10^{-5}	1.57×10^{-4}	0.29
0.9	2.0	0.12462802	7.66×10^{-5}	2.27×10^{-4}	0.29
0.9	1.0	0.12357699	3.06×10^{-4}	8.67×10^{-4}	0.29
0.8	3.5	0.12501495	2.05×10^{-5}	1.10×10^{-4}	0.41
0.8	2.5	0.12474644	4.16×10^{-5}	2.26×10^{-4}	0.41
0.8	2.0	0.12450264	6.71×10^{-5}	3.66×10^{-4}	0.41
0.8	1.0	0.12311966	3.10×10^{-4}	1.83×10^{-3}	0.41
0.1	3.5	0.12470192	2.10×10^{-5}	1.06×10^{-4}	0.94
0.1	2.5	0.12408709	5.60×10^{-5}	2.92×10^{-4}	0.94

distance between the quasi-steady-states are given in table 4.1. Several dependencies of those properties of the Arnold tongues on the parameters Δ and χ are deduced. The offset frequency ω_0 decreases as Δ and χ are decreased. The corresponding period is given by $T_0 = \frac{2\pi}{\omega_0}$. The period T_0 is the period which is expected for a 1-kink-solution at the given parameter set without periodic potential ($A = 0$). Therefore, the results indicate an increasing period T_0 of a 1-kink-solution without periodic potential for decreasing Δ and decreasing χ. This is also found in a previous work on the DAE without periodic potential [Mun19] for decreasing Δ.

The width of the tongues cannot be compared under the same conditions because some of the tongues are open to the right side. However, comparing the width for an amplitude which is lower than the occurrence of this effect is suitable. Thus $w(A = \frac{\pi}{4})$ is used. It shows a wider tongue at $A = \frac{\pi}{4}$ for lower feedback strengths χ. No robust statement of the dependency of $w(A = \frac{\pi}{4})$ on Δ can be given on the basis of the results. The impact of a change in the detuning Δ, however, is smaller than the impact of a change in the feedback strength χ.

4.5.1. Open Arnold Tongues

In the detailed discussion of the Arnold tongue at $\Delta = 0.8$, $\chi = 3.5$, $\psi = 0$ and $\tau = 50$ in section 4.4.3, $w(A_1) > w(A_2)$ is obtained for $A_1 > A_2$. It is also valid for those Arnold tongues in fig. 4.15 which are not open at the right side of the tongue. But it does not apply for the tongues which are open at their right side. The Arnold tongues in fig. 4.15(a,d,g,i) show this phenomena. All of them are tongues at $\Delta = 0.9$. No parameter set is found where the tongue opens up at its left side. The presented Arnold

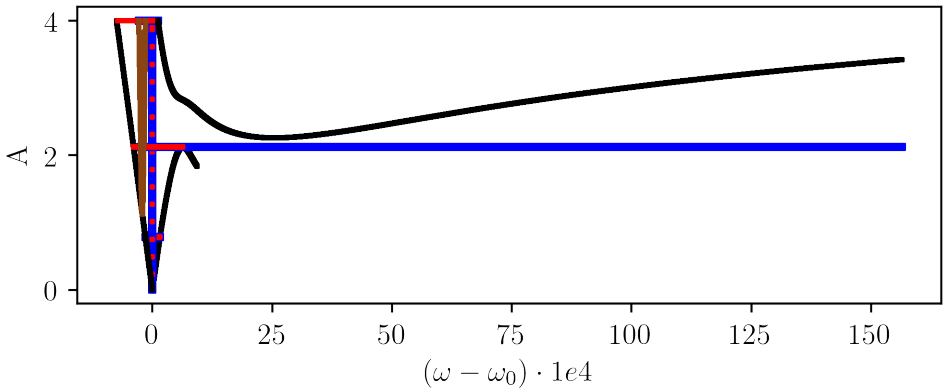

Figure 4.16: Continuation in the $A-\omega-$plane of (black) fold bifurcations of periodic solutions, (brown) period doubling bifurcations and (blue and red corresponding to their stability) periodic 1-kink-solutions continued in ω (and z_0) at $A = \frac{\pi}{4}$, $A \approx 2.123$ and $A = 4$ and in A (and z_0) at $\omega \approx 0.1235770$ for the parameter set: $\Delta = 0.9$, $\chi = 1.0$, $\psi = 0$ and $\tau = 50$. The offset $\omega_0 \approx 0.12357699$ is chosen. The Arnold tongue corresponds to the tongue shown in fig. 4.15 (i). The attention is turned to the opening at the right side of the tongue. The fold bifurcation at lower potential A and the unstable part of the 1-kink-solution at $A \approx 2.123$ are not be continued further because the continuation in `DDE-BIFTOOL` got stuck.

tongues at $\Delta = 0.9$ indicate a dependency of the amplitude at which the tongues open up on the feedback strength χ. The lower the feedback strength χ the lower the value for the amplitude where the tongue opens up. The opening of the Arnold tongue at $\Delta = 0.9$, $\chi = 1.0$, $\psi = 0$ and $\tau = 50$ is investigated further in the following.
The Arnold tongue is illustrated at a scale which turns the attention to the opening of the tongue at the right side in fig. 4.16. The Arnold tongue opens up to a relatively large region of synchronization compared to the tongue itself at the right side around the value $A \approx 2.123$ of the potential. However, the dependency of the width $w(A_1) > w(A_2)$ of the tongue on the amplitude is observed for amplitudes below the threshold $A_{\text{hill}} > A_1 > A_2$. The branch of periodic solutions at $A \approx 2.123$ shows that stable periodic 1-kink-solutions exist for parameter sets inside this larger region of synchronization especially for $\omega \gg \omega_0 + \delta_+(A < A_{\text{hill}})$ with $A_{\text{hill}} \approx 2.122$. The position of the kinks along and some profiles of the solutions of the branch are illustrated in fig. 4.17. The solutions 1 and 2 lie inside the Arnold tongue. The figure indicates that the profile $\theta(t)$ – especially the position of the kinks – looks similar to the previously investigated branches of periodic solutions inside the Arnold tongue (figs. 4.11 and 4.13). At first, two different solutions with different positions of the kink coexist at each value of ω. The change of stability of the solutions inside the tongue instead of the change at $\omega = \omega_0 - \delta(A \approx 2.123)$ is resulting from the period doubling bifurcation which is discussed in the following section. Additionally, the position of the kink is close to the minimum of the potential for the stable solutions. Secondly, it exists a solution for any position of the kink inside the potential and this solution depends on ω. Third, the positions of the kink at the fold

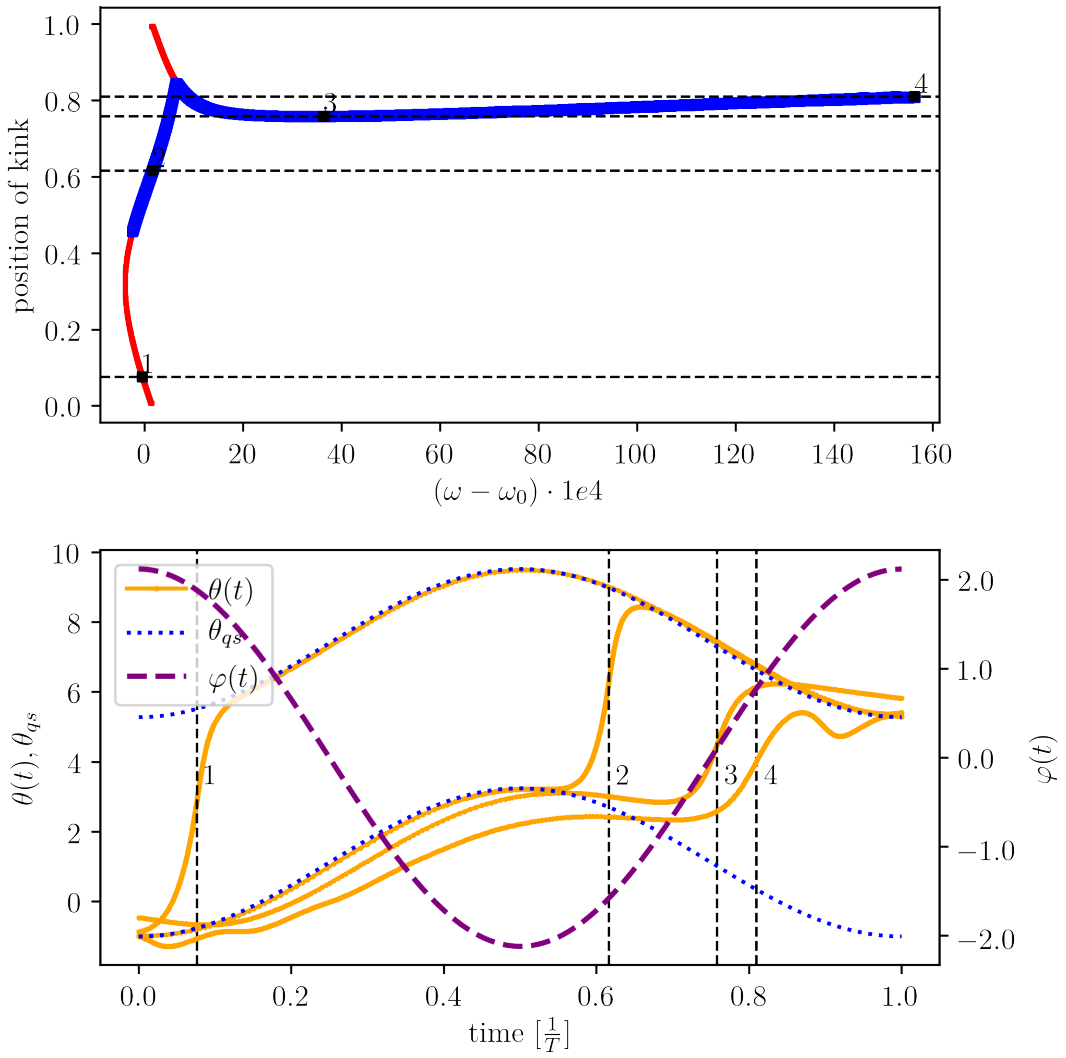

Figure 4.17: Continuation in ω (and z_0) of periodic 1-kink-solutions for the parameter set: $\Delta = 0.9$, $\chi = 1.0$, $\psi = 0$, $\tau = 50$ and $A \approx 2.123$. The upper figure illustrates the position of the kinks versus the continuation parameter ω. The thin red lines correspond to an unstable and the thick blue lines to a stable solution. $\omega_0 \approx 0.12357699$ is chosen as an offset. The profiles of the phase θ of four different periodic solutions are shown in the bottom figure as examples. The dotted black lines in both figures correspond to the position of the kink at the corresponding periodic 1-kink-solution. Note that the axis 'position of the kink' is periodic, i.e. the positions at 0 and 1 coincide.

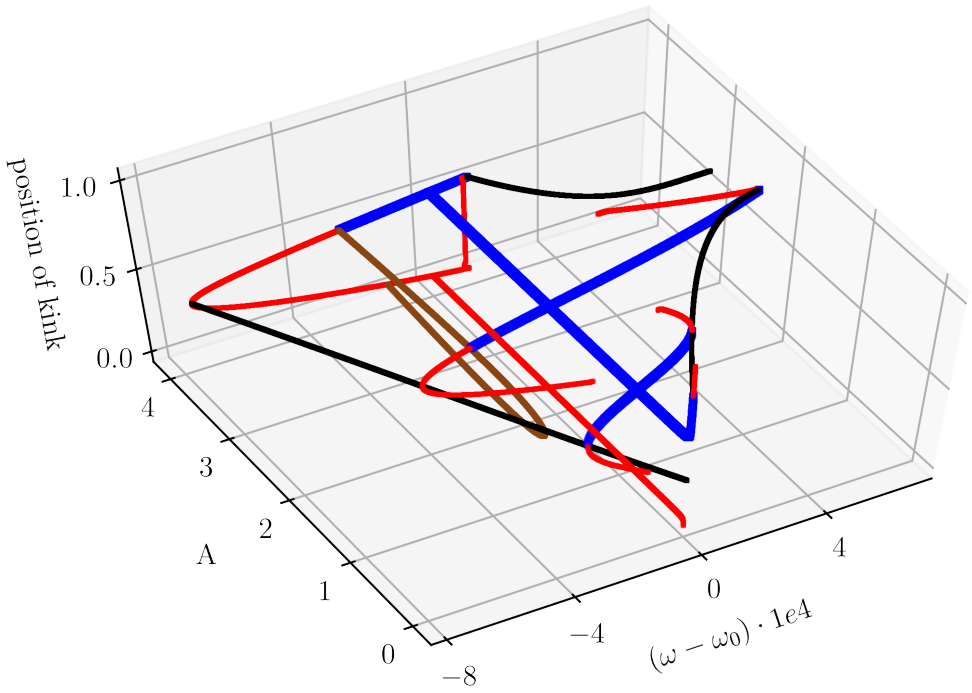

Figure 4.18: Continuation in the A-ω-position-space of (black) fold bifurcations of periodic solutions, (brown) period doubling bifurcations and (blue and red corresponding to their stability) periodic 1-kink-solutions continued in ω (and z_0) at $A = \frac{\pi}{4}$, $A \approx 2.123$ and $A = 4$ and in A (and z_0) at $\omega \approx 0.1235770$ for the parameter set: $\Delta = 0.9$, $\chi = 1.0$, $\psi = 0$ and $\tau = 50$. The offset $\omega_0 \approx 0.12408709$ is chosen. The Arnold tongue corresponds to the tongue shown in fig. 4.15 (i).

bifurcation are approximately 0.3 and approximately 0.8. And finally, the background oscillation of solutions follow the stable quasi-steady-state θ_{qs}.

The solutions 3 and 4 lie in the region where the Arnold tongue opens up to its right side. Both of them are stable solutions as indicated by the blue lines. The transition in the branch between the periodic solution inside the Arnold tongue and the additional synchronized region is clearly visible at the bump of the axis 'position of the kink'. Note that it is not determined whether the unstable part of the branch is connected to the stable part of the branch at this point. The continuation of the unstable part with `DDE-BIFTOOL` got stuck at this point which is the reason why the branch ends in the figure. The position of the kink in the opened up synchronized region is almost constant around 0.8 in the frequency ω, in contrast to the position of the kink inside the Arnold tongue. Moreover, the periodic solutions differ stronger in their profiles $\theta(t)$ for increasing ω. The stable quasi-steady-state does not describe the oscillation of the background well for the solutions 3 and 4. Further, an additional little dip occurs in the profile of solution 4.

Figures 4.18 and 4.19 indicate differences between the Arnold tongue at a lower $A < A_{\text{hill}}$ and at a higher amplitude $A > A_{\text{hill}}$ than the amplitude of the opening of the tongue.

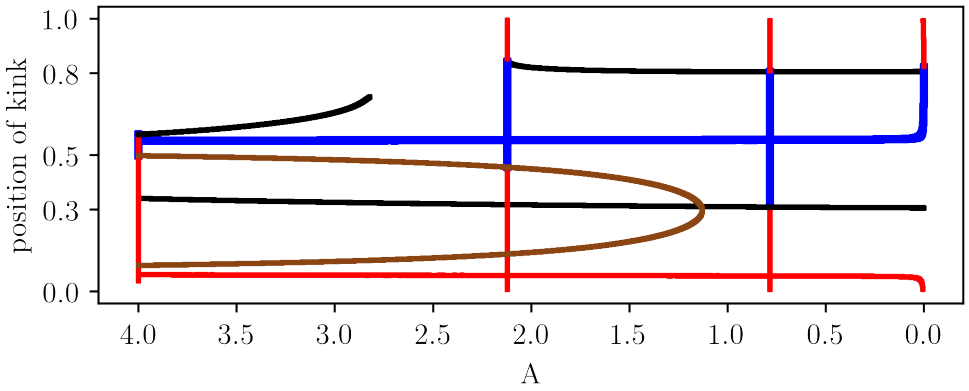

Figure 4.19: Continuation in the A-position-plane of (black) fold bifurcations of periodic solutions, (brown) period doubling bifurcations and (blue and red corresponding to their stability) periodic 1-kink-solutions continued in ω (and z_0) at $A = \frac{\pi}{4}$, $A \approx 2.123$ and $A = 4$ and in A (and z_0) at $\omega \approx 0.1235770$ for the parameter set: $\Delta = 0.9$, $\chi = 1.0$, $\psi = 0$ and $\tau = 50$. Note that the axis 'position of the kink' is periodic, i.e. the positions at 0 and 1 coincide.

The tongue looks similar to the previously discussed tongue at $\Delta = 0.8$, $\chi = 3.5$, $\psi = 0$ and $\tau = 50$ for amplitudes below the opening of the tongue besides the period doubling bifurcation. The fold bifurcations are the borders of the tongue in ω and they occur at a constant position of the kink at approximately 0.3 and approximately 0.8 in A. The properties of the periodic branches inside the tongue are mentioned in the analysis of the branch of periodic solutions at $A \approx 2.123$. Additionally, those observations are made in a region around the fold bifurcation at $\omega_0 - \delta_-(A > A_{\text{hill}})$ for amplitudes above the opening of the tongue. The position of the kink at the fold bifurcation at $\omega_0 + \delta_+(A)$, however, is increasing for a decreasing amplitude A above the opening of the tongue. Moreover, the position of the kink of a periodic solution drops to 0 at the fold bifurcation. Therefore, no solution exists where the kink is at a greater position than at the fold bifurcation for $A > A_{\text{hill}}$.

4.5.2. Period Doubling Bifurcation Inside the Arnold Tongue

A period doubling bifurcation inside the Arnold tongue is found and continued for the parameters $\Delta = 0.1$ and $\chi = 2.5$, $\Delta = 0.8$ and $\chi = 1.0$ and $\Delta = 0.9$, $\chi = 1.0$ which are presented in fig. 4.15(f,j,i), respectively. All three Arnold tongues look similar with respect to the period doubling bifurcation. Therefore, the period doubling bifurcation is analyzed for the parameter set $\Delta = 0.9$, $\chi = 1.0$ which is already used for the investigation of the opening of the tongue. A 3D-plot of the Arnold tongue is presented in fig. 4.18.

The branches of periodic 1-kink-solutions continued in ω at $A \approx 2.123$ and $A = 4$ intersect two times with the branch of the period doubling bifurcation. The general bifurcations along such branches inside the Arnold tongue can be summarized. Starting at

a stable periodic 1-kink-solution inside the tongue for decreasing ω, the first encountered bifurcation is the period doubling bifurcation. The branches change their stability inside the Arnold tongue $\omega_0 - \delta_-(A) < \omega < \omega_0 + \delta_+(A)$ because one Floquet-multiplier leaves the unit circle at -1. The fold bifurcation at $\omega_0 - \delta_-(A)$ is reached if ω is decreased further. Another Floquet-multiplier leaves the unit circle at 1. Increasing ω and following the branch further, a period doubling bifurcation is met and one Floquet-multipler enters the unit circle at -1. More Floquet-multipliers first leave and then reenter the unit circle via multiple fold and some torus bifurcations, if the branch is followed further until a periodic solution with one unstable Floquet-multiplier is obtained again. Finally, the unstable solution becomes stable through the fold bifurcation at $\omega_0 + \delta_+(A)$. This thesis focuses on the Arnold tongue and the transitions between stable and unstable solutions inside the tongue. Hence, the other fold and torus bifurcations are not investigated further.

The branch of the period doubling bifurcation meets the branch of the fold bifurcation at $\omega_0 - \delta_-(A \approx 1.2)$. No period doubling bifurcation is found below that amplitude. The branches of periodic solutions continued in ω inside the tongue are similar to the branch shown in fig. 4.11. The branch of periodic solutions emerges at both sides with respect to the axis 'position of the kink' from the fold bifurcation for increasing amplitude A. The part of the branch which is at the side of the fold bifurcation where the stable solutions exist connects stable and unstable solutions inside the Arnold tongue. The other part connects unstable and unstable solutions inside the Arnold tongue. This first one splits the region inside the Arnold tongue in the $A - \omega-$plane into two parts. A region where a stable solutions exist, close to the fold bifurcation at $\omega_0 + \delta_+(A)$, and a region where no stable solutions exist, close to the fold bifurcation at $\omega_0 - \delta_-(A)$.

The part of the branch which connects the stable and unstable solutions is investigated further using DNSs. The periodic doubling bifurcation at $A = 4$ is found at $\omega_{\mathrm{PD}}(A = 4) = 0.1232953648 = \omega_0 - 2.8163 \times 10^{-4}$. A stable periodic 1-kink-solution is obtained by a DNS close to the period doubling bifurcation in the region where stable 1-kink-solutions exist. Multiple long time calculations are performed while ω is decreased in small steps at a constant value of A such that the period doubling bifurcation at $\omega_{\mathrm{PD}}(A = 4)$ is crossed while the last calculated round trip of the previous calculation is used as initial round trip for the next calculation. Two results – one at each side of the bifurcation – are shown in fig. 4.20 as an example. The solution at the stable side of the bifurcation which is illustrated in fig. 4.20(a) corresponds to the kind of solution which is investigated in the last sections with a period $T \approx \tau = 50$. The solution of this period changes its stability at the bifurcation point as obtained through the continuation in `DDE-BIFTOOL`. However, unstable solutions are not found by long time DNSs with little noise. Thus, fig. 4.20(b) corresponds to a stable solution at the other side of the bifurcation which was called the unstable side of the period doubling bifurcation. More precisely, this side must be called the unstable side of the period doubling bifurcation for solutions of period $T \approx \tau = 50$. The stable solution which is calculated by a DNS

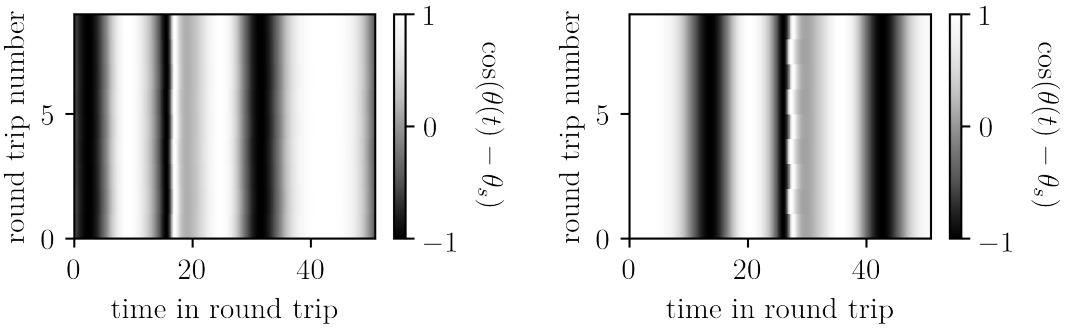

(a) $\omega = \omega_{\mathrm{PD}}(A = 4) + 0.46 \times 10^{-5}$ **(b)** $\omega = \omega_{\mathrm{PD}}(A = 4) - 9.54 \times 10^{-5}$

Figure 4.20: Last round trips of long time DNSs (a) at the stable and (b) unstable side of the period doubling bifurcation at $\omega_{\mathrm{PD}}(A = 4) = 0.1232953648 = \omega_0 - 2.8163 \times 10^{-4}$ for the parameter set: $\Delta = 0.9$, $\chi = 1.0$, $\psi = 0$, $\tau = 50$, $\epsilon = 1 \times 10^{-7}$ and $A = 4$. The doubled period in (b) with respect to (a) is clearly visible at $t \approx 24$.

seems to have a period of $T \approx 2\tau = 100$. The periodicity is checked by the creation of a first return map.

The concept of a first return map is explained in section 2.4.2. The measure I_n is defined as

$$I_n = \int_0^1 dx \cos\left(\theta\left(x\right)\right) \quad \text{where} \quad x = \frac{t}{T_\varphi} - n \tag{4.13}$$

where $T_\varphi = \dfrac{2\pi}{\omega}$ is the period of the periodic potential. The advantage of this measure, over a measure as the position of the kink, is that in this case all values of the phase in one period of the potential are taken into account. In particular, a change of the background is measured, which was not the case if the measure would be defined as the position of the kink.

Some first return maps are illustrated in fig. 4.21(a) as examples. At the stable side of the bifurcation $\omega > \omega_{PD}$ the return map shows one point at $I_{n+1} = I_n$ indicating that the period of the solution corresponds to the period that is chosen which is the period of the potential $T = T_\varphi$ in this case. Two points are visible on the return maps at the other side of the bifurcation $\omega < \omega_{PD}$ indicating a doubled period $2T$ of the solution. Hence, the return maps confirm the periodicity that is visible in fig. 4.20. The distance between the points in the return map increases the greater the distance between ω and ω_{PD} becomes for $\omega < \omega_{PD}$. The distance $I_{n+1} - I_n$ is therefore presented in fig. 4.21(b). The smoothly increasing distance around the bifurcation point ω_{PD} strongly indicates a supercritical period doubling bifurcation.

The period doubling bifurcations for the parameters $\Delta = 0.1$ and $\chi = 2.5$ and $\Delta = 0.8$ and $\chi = 1.0$ are investigated similarly. For the latter $\omega_{\mathrm{PD}}(A = 4) = 0.1230701468 = \omega_0 - 4.951 \times 10^{-5}$ is obtained from the continuation in `DDE-BIFTOOL`. However, the results of the DNSs suggest $\omega_{\mathrm{PD}}(A = 4) = 0.1231201468 = \omega_0 + 4.9 \times 10^{-7}$. Both values differ

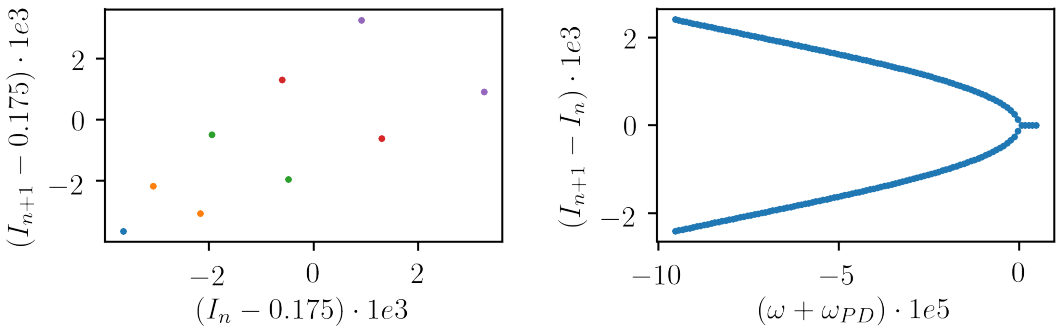

(a) examples of the first return map

(b) differences in the first return map

Figure 4.21: (a) First return map of the last 50 calculated periods at (blue) $\omega \approx \omega_{\mathrm{PD}}(A = 4) + 0.4 \times 10^{-5}$, (yellow) $\omega \approx \omega_{\mathrm{PD}}(A = 4) - 1.6 \times 10^{-5}$, (green) $\omega \approx \omega_{\mathrm{PD}}(A = 4) - 4.1 \times 10^{-5}$, (red) $\omega \approx \omega_{\mathrm{PD}}(A = 4) - 6.7 \times 10^{-5}$ and (purple) $\omega \approx \omega_{\mathrm{PD}}(A = 4) - 9.1 \times 10^{-5}$. (b) Difference $I_{n+1} - I_n$ between the points in the return maps of the last 20 periods. The results are obtained from direct numerics close to the period doubling bifurcation at $\omega_{\mathrm{PD}}(A = 4) = 0.1232953648 = \omega_0 - 2.8163 \times 10^{-4}$ for the parameter set: $\Delta = 0.9$, $\chi = 1.0$, $\psi = 0$, $\tau = 50$, $\epsilon = 1 \times 10^{-7}$ and $A = 4$. The measure I_n is defined in eq. (4.13).

by 5×10^{-5} which is assumed to be an numerical inaccuracy. The results of the DNSs are displayed in fig. 4.22. The same conclusions as for the previous period doubling bifurcation at $\Delta = 0.9$ and $\chi = 1.0$ apply. Again, a supercritical bifurcation is detected. Figure 4.23 shows the outcome of the analysis of the period doubling bifurcation at $\Delta = 0.8$ and $\chi = 1.0$. The supercritical period doubling bifurcation is found at $\omega_{\mathrm{PD}}(A = 4) = 0.1240126821 = \omega_0 - 7.441 \times 10^{-5}$. Additionally, to the period-1 and period-2 orbits, each at one side of that bifurcation, period-4 orbits and further orbits are detected in the first return map as it is presented in fig. 4.23(a). Figure 4.23(b) indicates a route to chaos via period doubling. The supercritical period doubling bifurcation which corresponds to the transition between period-2 and period-4 orbits is clearly visible around $\omega \approx \omega_{\mathrm{PD}}(A = 4) - 5 \times 10^{-5}$. It seems like further supercritical period doubling bifurcations occur for decreasing ω until a chaotic window is reached. The co-moving reference frame of the last round trips of the examples shown in the return map in fig. 4.23(a) are illustrated in fig. 4.24. The period-2 and period-4 orbits can be identified. For values of $\omega \lesssim \omega_{\mathrm{PD}}(A = 4) - 7 \times 10^{-5}$ lower than the values for the chaotic window, stable solutions of period-1 are detected again as before the first period doubling bifurcation at ω_{PD}. Note that this solution is not obtained in the further continuation in ω of the branch of periodic solutions at $A = 4$ in `DDE-BIFTOOL`, because the results of DNSs might have fallen on another attractor and `DDE-BIFTOOL` have not.

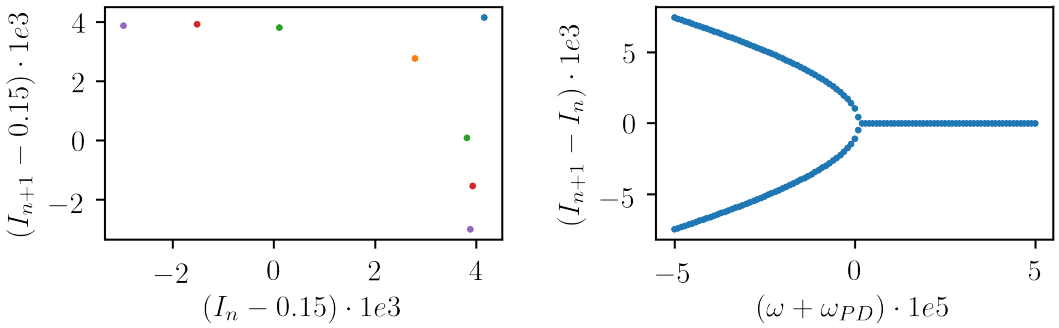

(a) examples of the first return map **(b)** differences in the first return map

Figure 4.22: (a) First return map of the last 50 calculated periods at (blue) $\omega \approx \omega_{\mathrm{PD}}(A = 4) + 1.2 \times 10^{-5}$, (yellow) $\omega \approx \omega_{\mathrm{PD}}(A = 4) + 0.2 \times 10^{-5}$, (green) $\omega \approx \omega_{\mathrm{PD}}(A = 4) - 1.3 \times 10^{-5}$, (red) $\omega \approx \omega_{\mathrm{PD}}(A = 4) - 2.8 \times 10^{-5}$ and (purple) $\omega \approx \omega_{\mathrm{PD}}(A = 4) - 4.3 \times 10^{-5}$. (b) Difference $I_{n+1} - I_n$ between the points in the return maps of the last 20 periods. The results are obtained from direct numerics close to the period doubling bifurcation at $\omega_{\mathrm{PD}}(A = 4) = 0.1231201468 = \omega_0 + 4.9 \times 10^{-7}$ for the parameter set: $\Delta = 0.8$, $\chi = 1.0$, $\psi = 0$, $\tau = 50$, $\epsilon = 1 \times 10^{-8}$ and $A = 4$. The measure I_n is defined in eq. (4.13).

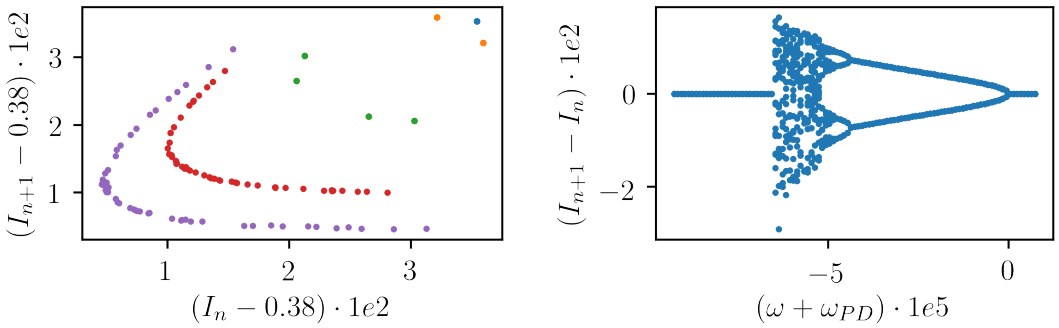

(a) examples of the first return map **(b)** differences in the first return map

Figure 4.23: (a) First return map of the last 50 calculated periods at (blue) $\omega \approx \omega_{\mathrm{PD}}(A = 4) + 0.2 \times 10^{-5}$, (yellow) $\omega \approx \omega_{\mathrm{PD}}(A = 4) - 1.8 \times 10^{-5}$, (green) $\omega \approx \omega_{\mathrm{PD}}(A = 4) - 4.8 \times 10^{-5}$, (red) $\omega \approx \omega_{\mathrm{PD}}(A = 4) - 5.8 \times 10^{-5}$ and (purple) $\omega \approx \omega_{\mathrm{PD}}(A = 4) - 6.3 \times 10^{-5}$. (b) Difference $I_{n+1} - I_n$ between the points in the return maps of the last 20 periods. The results are obtained from direct numerics close to the period doubling bifurcation at $\omega_{\mathrm{PD}}(A = 4) = 0.1240126821 = \omega_0 - 7.441 \times 10^{-5}$ for the parameter set: $\Delta = 0.1$, $\chi = 1.0$, $\psi = 0$, $\tau = 50$, $\epsilon = 1 \times 10^{-8}$ and $A = 4$. The measure I_n is defined in eq. (4.13).

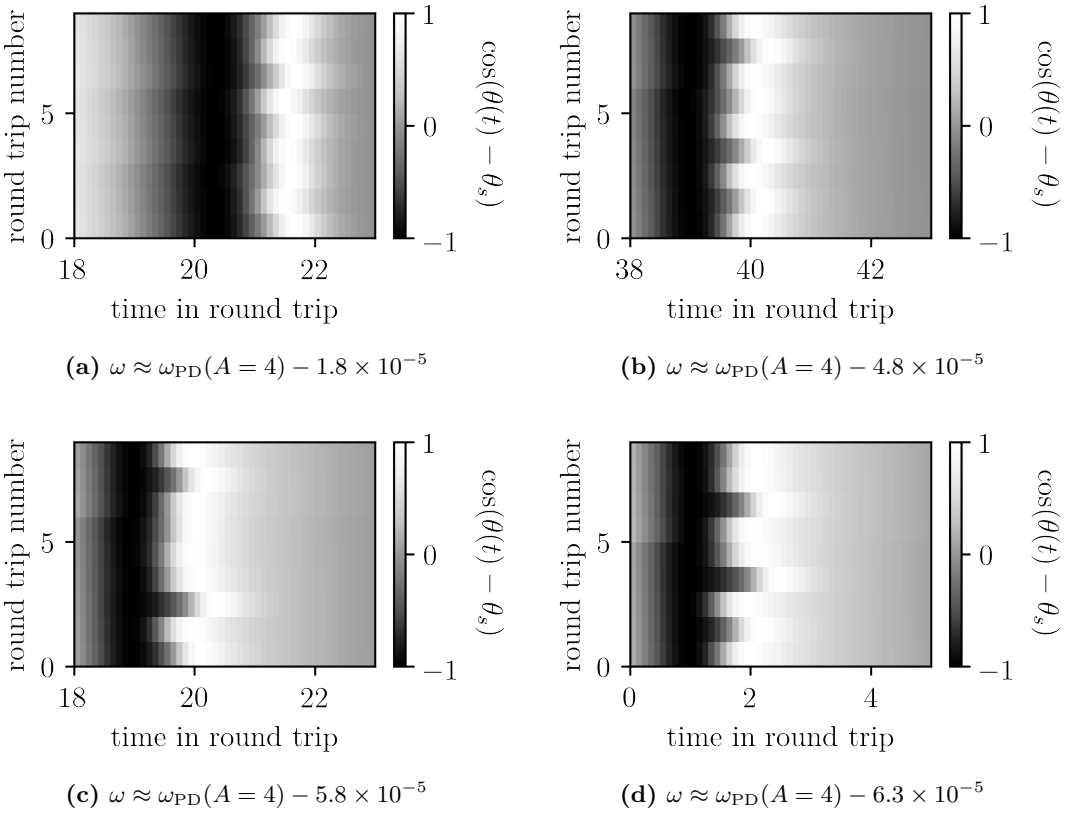

(a) $\omega \approx \omega_{\mathrm{PD}}(A = 4) - 1.8 \times 10^{-5}$

(b) $\omega \approx \omega_{\mathrm{PD}}(A = 4) - 4.8 \times 10^{-5}$

(c) $\omega \approx \omega_{\mathrm{PD}}(A = 4) - 5.8 \times 10^{-5}$

(d) $\omega \approx \omega_{\mathrm{PD}}(A = 4) - 6.3 \times 10^{-5}$

Figure 4.24: Part of last round trips of long time DNSs for an example of (a) period-2 and (b) period-4 orbits and (c) and (d) examples of orbits closer to the chaotic window on the route of period doubling. The frequencies are given with respect period doubling bifurcation at $\omega_{\mathrm{PD}}(A = 4) = 0.1232953648 = \omega_0 - 2.8163 \times 10^{-4}$ for the parameter set: $\Delta = 0.9$, $\chi = 1.0$, $\psi = 0$, $\tau = 50$, $\epsilon = 1 \times 10^{-7}$ and $A = 4$. The same examples as in the return map in fig. 4.23 (a) are chosen.

Table 4.2: Overview of the properties of the different Arnold tongues at $\chi = 1.0$, $\psi = 0$ and $\tau = 50$ which are shown in fig. 4.25. The width $w(A)$ which is defined in eq. (4.12) is determined at $A = \frac{\pi}{4}$ and $A = 4$. ω_0 corresponds to the point where the fold bifurcations meet at $A = 0$. The distance d between the stable and unstable quasi-steady-state is also given. Additionally the minimal value of the amplitude $A_{\mathrm{PD}_{\mathrm{min}}}$ for which the period doubling bifurcation can be found and the corresponding frequency $\omega_{\mathrm{PD}}(A_{\mathrm{PD}_{\mathrm{min}}})$ are determined.

Δ	ω_0	$w(A = \frac{\pi}{4})$	$w(A = 4)$	$d[\pi]$	$A_{\mathrm{PD}_{\mathrm{min}}}$	$\omega_{\mathrm{PD}}(A_{\mathrm{PD}_{\mathrm{min}}})$
0.90	0.12357699	3.06×10^{-4}	8.67×10^{-4}	0.29	1.13	$-2.10 \times 10^{-4} + \omega_0$
0.85	0.12335316	3.01×10^{-4}	1.58×10^{-3}	0.35	0.41	$-7.79 \times 10^{-5} + \omega_0$
0.80	0.12311966	3.10×10^{-4}	1.83×10^{-3}	0.41	0.26	$4.99 \times 10^{-5} + \omega_0$

4.5.3. Arnold Tongues at $\chi = 1.0$

Figure 4.15(j) indicates that the period doubling bifurcation exists for values of low amplitude $A < 0.5$. This corresponds to the approximately maximal amplitude which can be produced in experiments. Hence, the low amplitude region is especially interesting. Figure 4.15(i,j) indicates the dependency of the position of the period doubling bifurcation on Δ. The lower the detuning Δ the lower the frequencies ω with respect to the corresponding ω_0 where the period doubling bifurcation is found. Therefore, Δ is an important parameter in order to shift the period doubling bifurcation inside the Arnold tongue such that it reaches the low amplitude region $A < 0.5$.

The Arnold tongues at $\Delta = 0.9$, $\Delta = 0.85$ and $\Delta = 0.8$ are illustrated in fig. 4.25. The corresponding parameters are given in table 4.2. The overall structure of the three tongues is very similar. The widths of the tongues are identical with respect to the order of magnitude, however, the width $w(A = \frac{\pi}{4})$ increases for decreasing detuning Δ. A branch of a period doubling bifurcation is detected and continued in each of the Arnold tongues. The opening of the tongues at the right side is found for $\Delta = 0.9$ and $\Delta = 0.85$. Both of the effects are discussed in detail in sections 4.5.1 and 4.5.2.

The branch of the period doubling bifurcation is obtained at different positions inside the tongue meaning that the frequencies where the bifurcation is found differs with respect to the corresponding ω_0. A good measure for the position of the period doubling bifurcation in the Arnold tongue is the frequency $\omega_{\mathrm{PD}}(A_{\mathrm{PD}_{\mathrm{min}}})$, where the branch of the period doubling bifurcations meets a fold bifurcation. This corresponds to the minimal value of the amplitude $A_{\mathrm{PD}_{\mathrm{min}}}$ for which the period doubling bifurcation is found. The frequency $\omega_{\mathrm{PD}}(A_{\mathrm{PD}_{\mathrm{min}}})$ is increasing for decreasing Δ. The minimal value of the amplitude $A_{\mathrm{PD}_{\mathrm{min}}}$ depends on the value of the amplitude at the corresponding fold bifurcation at $\omega_{\mathrm{PD}}(A_{\mathrm{PD}_{\mathrm{min}}})$. The closer $\omega_{\mathrm{PD}}(A_{\mathrm{PD}_{\mathrm{min}}})$ is to ω_0 the lower $A_{\mathrm{PD}_{\mathrm{min}}}$. All in all, the period doubling bifurcation may be detectable in experiments since $A_{\mathrm{PD}_{\mathrm{min}}}$ can be adjusted by changing the detuning Δ. Two parameter sets for which $A_{\mathrm{PD}_{\mathrm{min}}} < 0.5$ is in the low amplitude region are already illustrated in this thesis.

The opening of the Arnold tongues is observed for $\Delta = 0.9$ and $\Delta = 0.85$. The am-

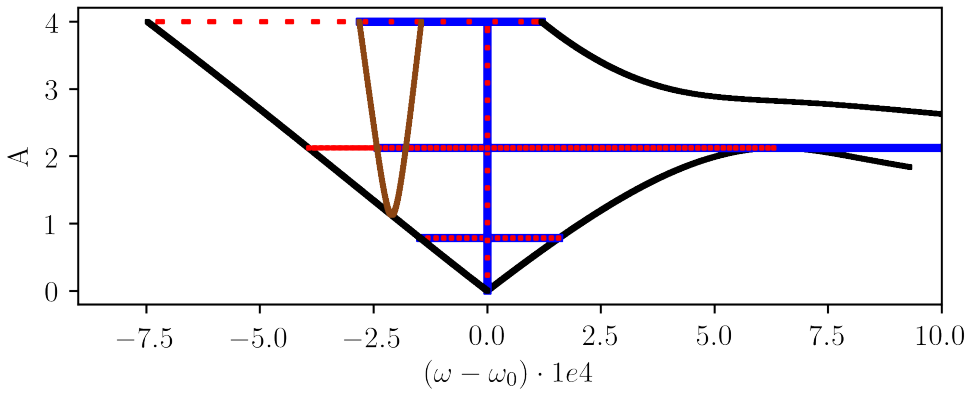

(a) $\Delta = 0.9$

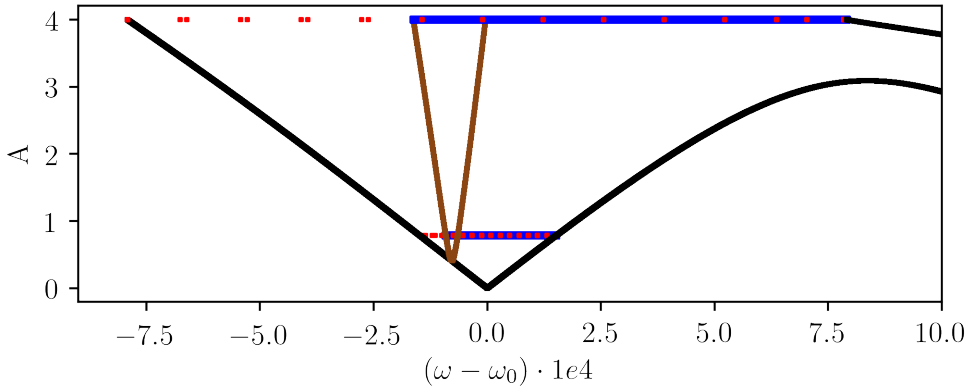

(b) $\Delta = 0.85$

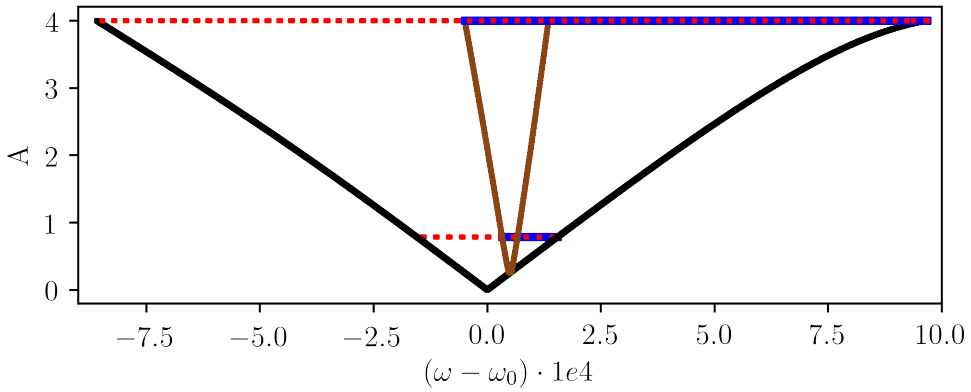

(c) $\Delta = 0.8$

Figure 4.25: Overview of Arnold tongues at different parameters at constant $\chi = 1.0$, $\psi = 0$ and $\tau = 50$. The chosen offset ω_0 for each parameter set is given in table 4.2. Black lines represent fold bifurcations of periodic orbits and brown lines period doubling bifurcations. Blue and red lines indicate periodic solutions which are stable or unstable, respectively.

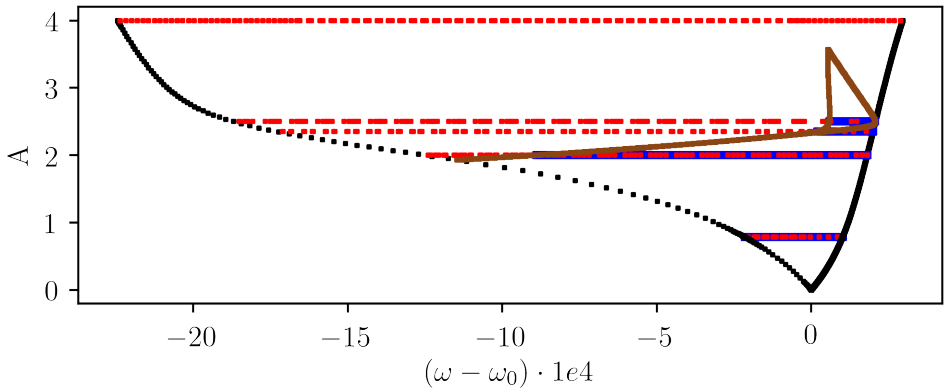

Figure 4.26: Continuation in the $A-\omega-$plane of (black) fold bifurcations of periodic solutions, (brown) period doubling bifurcations and (blue and red corresponding to their stability) periodic 1-kink-solutions continued in ω (and z_0) at $A = \frac{\pi}{4}, 2, 2.35, 2.5$ and $A = 4$ for the parameter set: $\Delta = 1.0$, $\chi = 1.0$, $\psi = \frac{\pi}{2}$ and $\tau = 50$. This parameter set is at a saddle-node and close to a Hopf bifurcation point of the steady states for the system without periodic potential. The offset $\omega_0 \approx 0.12107388$ is chosen. The widths $w(A = \frac{\pi}{4}) = 3.17 \times 10^{-4}$ and $w(A = 4) = 2.54 \times 10^{-3}$ are calculated. Moreover, $A_{\mathrm{PD}_{\mathrm{min}}} = 1.93$ and $\omega_{\mathrm{PD}}(A_{\mathrm{PD}_{\mathrm{min}}}) = -1.15 \times 10^{-3} + \omega_0$ is found.

plitude A_{hill} at which the tongue opens up is additionally dependent on the detuning Δ. A decreasing A_{hill} for decreasing feedback strength χ is already obtained previously from fig. 4.15. The amplitude A_{hill} of the opening of the tongue decreases as well for an increasing Δ as visualized in fig. 4.25. Additionally, the shape of the right fold bifurcation at $\omega_0 + \delta(A)$ indicates an open Arnold tongue for $A > 4$. Thus, Arnold tongues which are opening up in the low amplitude region might be obtained for $\Delta > 0.9$ or/and smaller $\chi < 1.0$. However, the conditions of the existence for a stable 1-kink-solution might restrict the parameters Δ and χ such that a tongue which opens up in the low amplitude region does not exist.

Additionally, the Arnold tongue is obtained for a parameter set ($\Delta = 1.0$, $\chi = 1.0$, $\psi = \frac{\pi}{2}$, $\tau = 50$) which is at an exceptional point in parameter space for the case without periodic potential because it corresponds to a saddle-node bifurcation of the steady states as given by eq. (2.55) and it is close to a Hopf bifurcation point of the steady states in the long delay limit, as given by eq. (2.59). Since the stability of the quasi-steady-states corresponds to the stability of the steady-states, this parameter set is also exceptional for the case with periodic potential as the oscillating background is at or at least close to two bifurcations. The Arnold tongue is shown in fig. 4.26. Two aspects differ significantly from all previously discussed tongues. Nevertheless, except from those the tongue is rather similar to the already presented ones. The two aspects are the branch of the period doubling bifurcation and the branch of the fold bifurcation at $\omega_0 - \delta_-(A)$. The shape of the latter results in a significant increase of $\delta_-(A)$ for a increasing amplitude

$\frac{\pi}{4} \lesssim A \lesssim 3$. Therefore, the width of the tongue $w(A)$ increases as well leading to the width $w(A = 4) = 2.54 \times 10^{-3}$.
However, the branch of the period doubling bifurcation spans over the whole range in ω of the tongue meeting the branches of the fold bifurcations at $\omega_0 - \delta_-(A \lesssim 2)$ and $\omega_0 + \delta_+(A \gtrsim 2)$. Additionally, the branch is restricted by the maximal amplitude $A_{\mathrm{PD}_{\max}} \approx 3.57$. As before, the period doubling bifurcation branch restricts the region of stable periodic 1-kink-solutions inside the Arnold tongue. In this case from both sides in ω. Hence, no stable 1-kink-solution exists for greater amplitudes than $A_{\mathrm{PD}_{\max}} \approx 3.57$ even inside the Arnold tongue of this parameter set.

4.6. 2-Kink-Solutions Inside the Periodic Potential

The behavior of a 1-kink-solution in a periodic potential of one minimum is investigated in detail in the previous sections. However, multiple kinks in one domain are observed in [Gar+17]. Especially, a stable background of six kinks inside a periodic potential of six minima, while an additional kink is hopping from one minima of the potential to the next is found. The background of N kinks in a periodic potential of N minima is essential for the presented behavior. Since the previous part studied the case for $N = 1$, the following section analyzes 2-kink-solutions in a periodic potential of two minima which corresponds to $N = 2$.
The parameters $\Delta = 0.8$, $\chi = 2.0$, $\psi = 0$ and $\tau = 50$ are used for the investigation as an example. The corresponding Arnold tongue for the case $N = 1$ where $T \approx \tau$ is illustrated in fig. 4.15(h). A potential with two minima is obtained in two different ways: Doubling the period of the solution $T \to 2T$ and doubling the frequency of the periodic potential $\omega \to 2\omega$. Both of them are leading to a doubled period of the solution with respect to the period of the potential $T = 2T_\varphi = 2\frac{2\pi}{\omega}$.
The first option is a starting point for a further research on periodic solutions and Arnold tongues around period doubling bifurcations which are discussed in section 4.5.2, because solutions, which are found to have period-2, have period-1 in the $T \to 2T$ picture. Thus, the solutions on both sides of the period doubling bifurcations might be detected and continued as periodic solutions by `DDE-BIFTOOL`. The Arnold tongue for parameter sets where a period doubling bifurcation is detected might differ from the Arnold tongue obtained for $T \to T$ which are presented in fig. 4.15. Nevertheless, those tongues without a period doubling bifurcation do not change because the phase in the first and the second half of the solution with the period $T \to 2T$ does not differ. An example is illustrated in fig. 4.27. The properties and the shape of the Arnold tongue are identical to the Arnold tongue which is shown in fig. 4.15(h). However, doubling the period of the solution $T \to 2T$ does not investigate 2-kink-solutions which are solutions containing two kinks in one time domain of approximated length $T \approx \tau$ corresponding to the definition given in the beginning of section 4.3. Therefore, it cannot be used to analyse solutions of multiple kinks in one time domain.

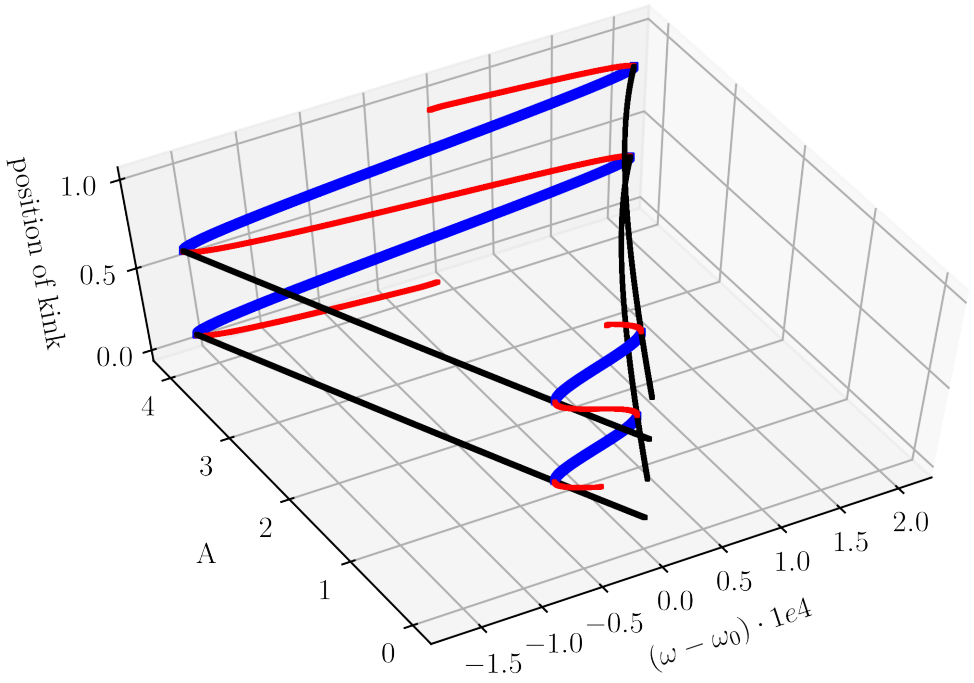

Figure 4.27: Continuation in the A-ω-position-space of (black) fold bifurcations of periodic solutions and (blue and red corresponding to their stability) in ω (and z_0) at $A = \frac{\pi}{4}$ and $A = 4$ of solutions of the period $T \to 2T$ for the parameter set: $\Delta = 0.8$, $\chi = 2.0$, $\psi = 0$ and $\tau = 50$. This leads to $T \approx 100$. The offset and all other properties are identical to the corresponding parameter set in table 4.1. Note that the axis 'position of the kink' is periodic, i.e. the positions at 0 and 1 coincide. Additionally, all branches are scattered twice in the plot due to the two kinks in the solution which leads to two positions of kinks.

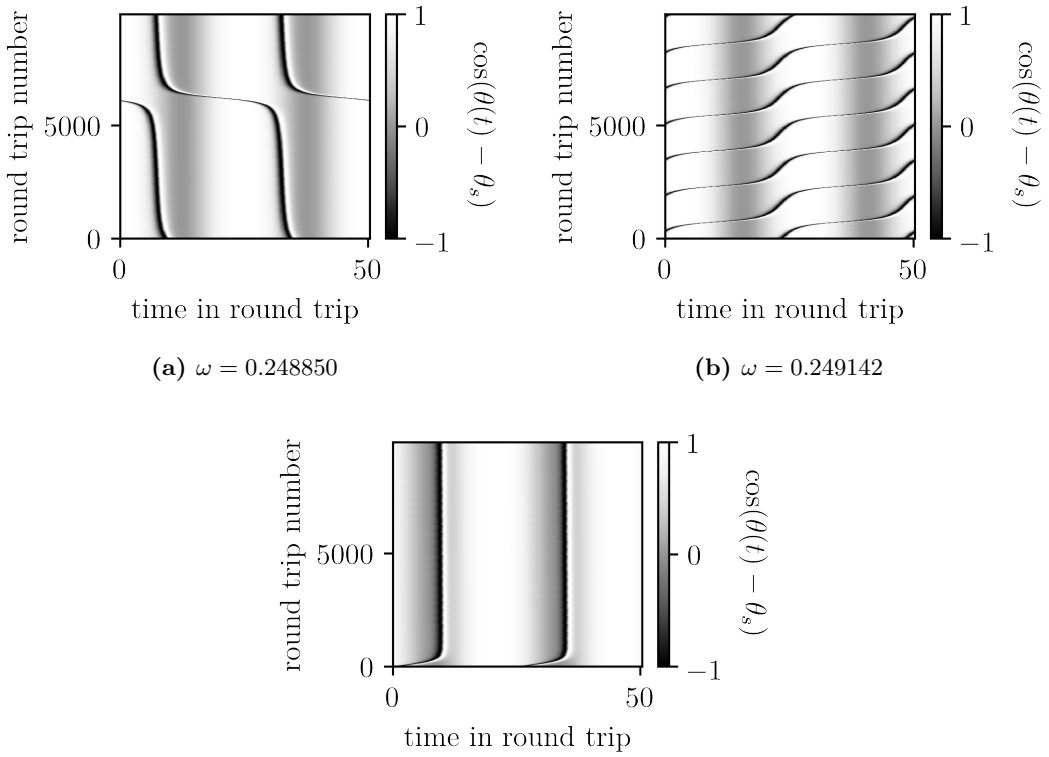

(a) $\omega = 0.248850$ **(b)** $\omega = 0.249142$

(c) $\omega = 0.249$

Figure 4.28: Results of a DNS with an initial condition which contains two 2π-shift for the parameter set: $\Delta = 0.8$, $\chi = 2.0$, $\psi = 0$, $\tau = 50$, $\epsilon = 0$ and $A = \frac{\pi}{4}$. The length of each round trip corresponds to twice the period of the periodic potential $T = 2T_\varphi$. Thus, the potential and the oscillation of the background are stationary in those figures and the position of the kink is regarded with respect to those. The kinks are travelling (a) to the left and (b) to the right from one potential minima to the next. The kinks are not trapped inside one potential minima. (c) Each kink is moving to a specific position of one minima of the potential in the beginning of the time evolution and remains at that position. Those kinks are trapped inside the potential.

The second option of doubling the frequency of the periodic potential $\omega \to 2\omega$ leads to 2-kink-solutions. Thus, it is used for the investigation of two kinks inside a potential of two minima. It is performed similarly to the study of the 1-kink-solution in section 4.4. Similar results are found.

Calculations of the time evolution of the phase via DNS are performed for different frequencies ω. Examples are illustrated in fig. 4.28. As before, two qualitative different types of solutions are observed. The kinks are travelling from one minima of the potential to the next in fig. 4.28(a,b). The LSs and the periodic potential are not synchronized. In contrast to this, each of the kinks is trapped inside one minima of the potential in fig. 4.28(c) and synchronization is observed. The behavior of the 2-kink-solution is identical to the behavior of the 1-kink-solution which is studied in section 4.4.1. Therefore, the explanations and conclusions given in that section can be extended for the case of

the 2-kink-solutions in similar parameter sets.
The branch of the periodic solutions continued in ω at $A = \frac{\pi}{4}$ is shown in fig. 4.29. In general, the figure is similar to fig. 4.11 besides the extension from a 1-kink-solution to a 2-kink-solution leading again to similar conclusions about the region of synchronization at constant amplitude as for the 1-kink-solution which are written in section 4.4.2. Moreover, the approximation of the oscillating background by the stable quasi-steady-state is still reasonable for this parameter set.
Nevertheless, a difference is found in the calculated Floquet-multipliers. At the bifurcation point of the 1-kink-solution one Floquet-multipler leaves the unit circle at 1. However, for the 2-kink-solution two Floquet-multipler leave the unit circle at 1. Nevertheless, setting up a branch of bifurcations points with `DDE-BIFTOOL` does not converge. Instead several branches of periodic solutions are continued which gives an impression of the shape of the Arnold tongue for the 2-kink-solution. Additionally, a branch of period doubling bifurcations is detected and continued. It is illustrated in fig. 4.26. The shape of the branches continued in ω indicate an opening of the Arnold tongue at its right side. Moreover, the period doubling bifurcations restricts the area of stable solutions inside the tongue. Both of the phenomena are discussed previously in sections 4.5.1 and 4.5.2, respectively. The results of the 1-kink-solution may be adapted to 2-kink-solutions.
Under the condition that the phase $\theta(t)$ is identical in the intervals $[0, \frac{1}{2}T = T_\varphi]$ and $[\frac{1}{2}T = T_\varphi, T = 2T_\varphi]$ with respect to the 2π-periodicity, the 2-kink-solutions of the period $T = 2T_\varphi \approx \tau$ may be regarded as 1-kink-solutions of the period $T = T_\varphi \approx \frac{1}{2}\tau$. The profiles illustrated in fig. 4.29 indicate the before mentioned. A further comparison of both halves of the profiles calculated by `DDE-BIFTOOL` for example by subtraction of both is not very reasonable because of the adaptive mesh which is used in `DDE-BIFTOOL`. Therefore, an interpolation between the mesh points would be necessary which would lead to numerical inaccuracies. Since the differences in the profiles are expected to be very small, a difference due to numerical reasons could not be distinguished to a difference due to an actual difference in the profile. Nevertheless, under the assumption that the phase $\theta(t)$ in both halves of the 2-kink-solutions are identical, they correspond to the 1-kink-solutions of the period $T = T_\varphi \approx \frac{1}{2}\tau$.
Therefore, the Arnold tongue for the 1-kink-solutions of the period $T = T_\varphi \approx \frac{1}{2}\tau$ is calculated and presented in fig. 4.31. The bifurcations which are the borders of this Arnold tongue are different to all previously obtained borders. The Floquet-multiplier at the branches continued in ω indicate a fold and a period doubling bifurcation at those borders of the tongue since one Floquet-multiplier leaves the unit circle at 1 and another at -1. Thus, the number of unstable Floquet-multipliers changes from 0 to 2. The continuation of the bifurcations in `DDE-BIFTOOL` shows that the branches of both kinds of bifurcations are identical in the $A - \omega-$plane. Since the Floquet-multipliers of the branch continued in ω for the 2-kink-solutions of the period $T = 2T_\varphi \approx \tau$ indicate a fold

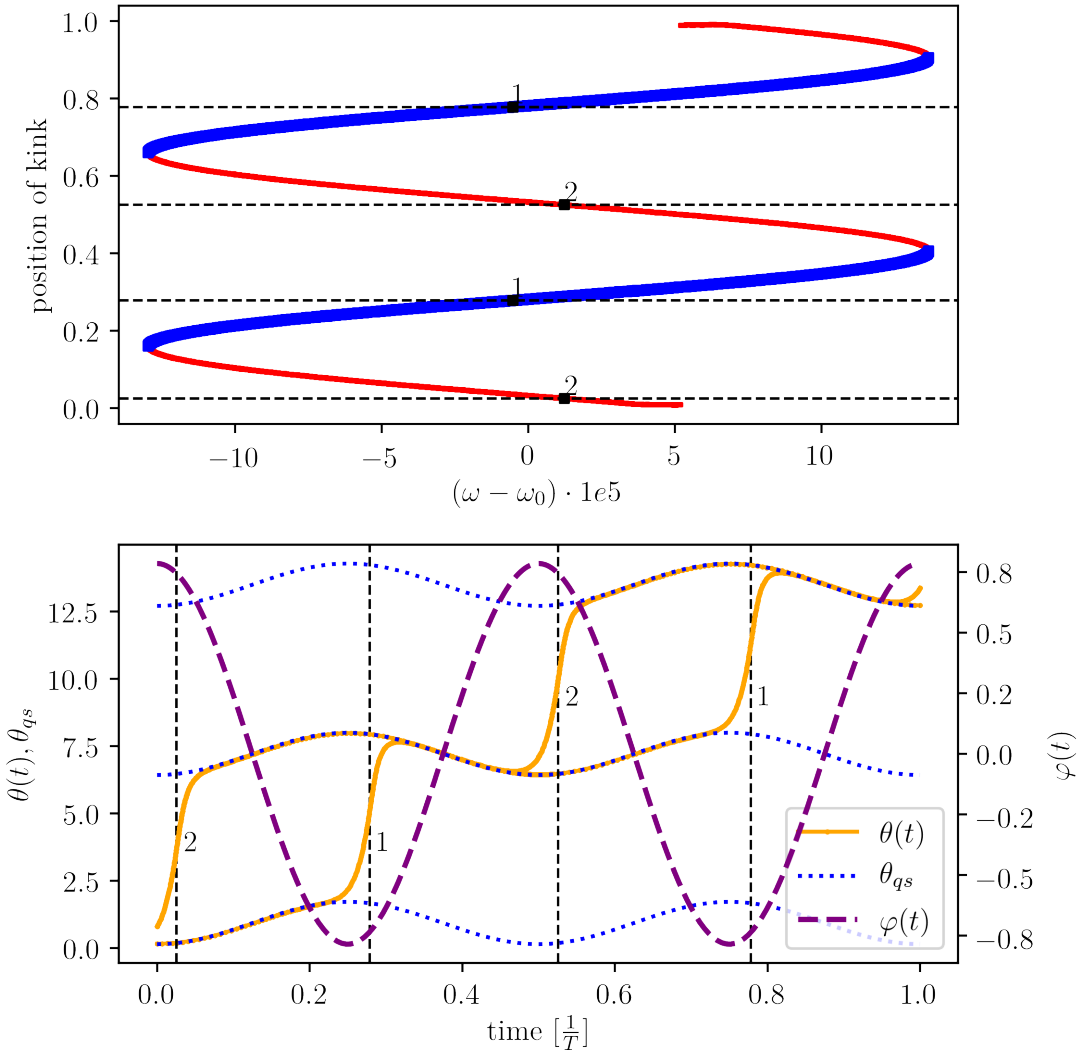

Figure 4.29: Continuation in ω (and z_0) of periodic 1-kink-solutions for the parameter set: $\Delta = 0.8$, $\chi = 2.0$, $\psi = 0$, $\tau = 50$ and $A = \frac{\pi}{4}$. The length of one period corresponds to twice the period of the periodic potential $T = 2T_\varphi$. The upper figure illustrates the position of the kinks versus the continuation parameter ω. The thin red lines correspond to an unstable and the thick blue lines to a stable solution. $\omega_0 \approx 0.2490053$ is chosen as an offset. The profiles of the phase θ of two different periodic solutions at $\omega_1 \approx 0.249$ (stable) and $\omega_2 \approx 0.24902$ (unstable) are shown in the bottom figure as examples. The dotted black lines in both figures correspond to the position of the kinks at the corresponding periodic 2-kink-solution. The periodic solution 1 corresponds to the results presented in fig. 4.28(c).

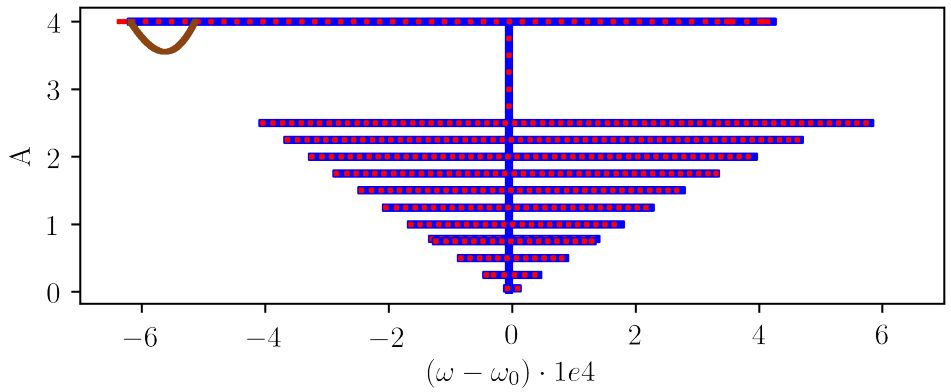

Figure 4.30: Continuation in the $A-\omega-$plane of (brown) period doubling bifurcations and (blue and red corresponding to their stability) periodic 2-kink-solutions continued in ω (and z_0) at $A = 0.05, 0.25, 0.5, 0.75, \frac{\pi}{4}, 1.0, 1.25, 1.5, 1.75, 2.0,$,$A = 2.25, 2.5$ and $A = 4$ and in A (and z_0) at $\omega = 0.249$ for the parameter set: $\Delta = 0.8$, $\chi = 2.0$, $\psi = 0$ and $\tau = 50$. The length of each round trip corresponds to twice the period of the periodic potential $T = 2T_\varphi \approx \tau$ leading to 2-kink-solutions. $\omega_0 \approx 0.2490053$ is chosen as an offset. The widths $w(A = \frac{\pi}{4}) = 2.66 \times 10^{-4}$ and $w(A = 4) = 1.06 \times 10^{-3}$ are calculated.

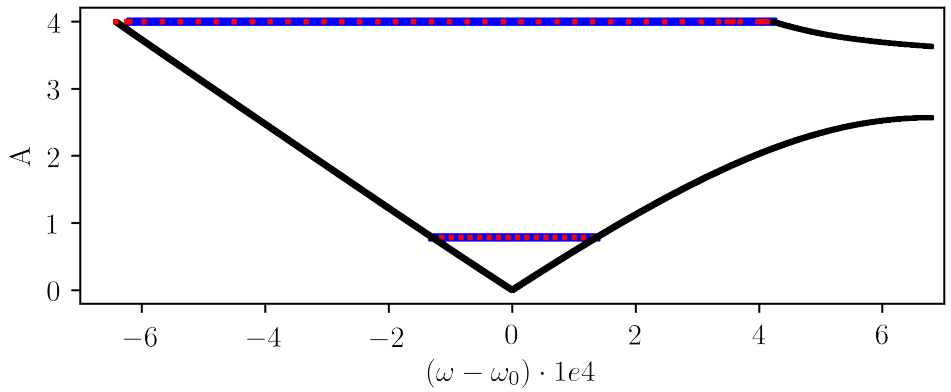

Figure 4.31: Continuation in the $A-\omega-$plane of (black) fold bifurcations of periodic solutions and (blue and red corresponding to their stability) periodic 1-kink-solutions continued in ω (and z_0) at $A = \frac{\pi}{4}$ and $A = 4$ for the parameter set: $\Delta = 0.8$, $\chi = 2.0$, $\psi = \frac{\pi}{2}$ and $\tau = 50$. The length of each round trip corresponds to once the period of the periodic potential $T = T_\varphi \approx \frac{1}{2}\tau$ leading to 1-kink-solutions. $\omega_0 \approx 0.2490053$ is chosen as an offset. The widths $w(A = \frac{\pi}{4}) = 2.66 \times 10^{-4}$ and $w(A = 4) = 1.06 \times 10^{-3}$ are calculated. Moreover, $A_{\text{hill}} \approx 2.57$ is found.

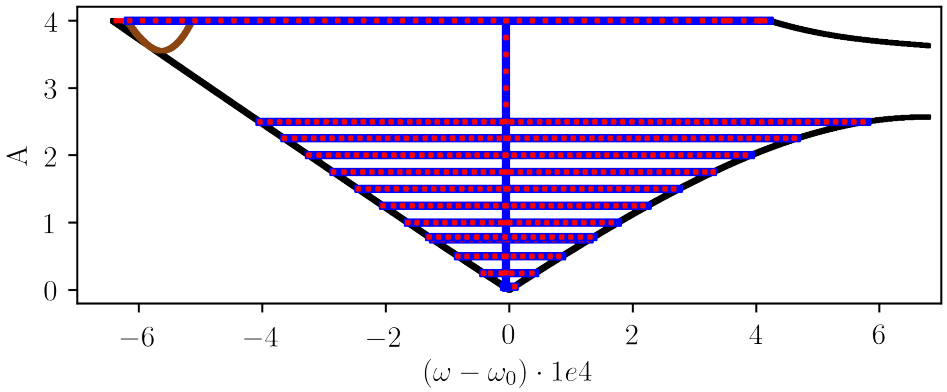

Figure 4.32: Continuation in the $A - \omega-$plane of (black) fold bifurcations of periodic 1-kinks-solutions from fig. 4.31, of (brown) period doubling bifurcations from fig. 4.30 and (blue and red corresponding to their stability) periodic 2-kink-solutions from fig. 4.30 continued in ω (and z_0) at $A = 0.05, 0.25, 0.5, 0.75, \frac{\pi}{4}, 1.0, 1.25, 1.5, 1.75, 2.0,$ $,A = 2.25, 2.5$ and $A = 4$ and in A (and z_0) at $\omega = 0.249$ for the parameter set: $\Delta = 0.8$, $\chi = 2.0$, $\psi = \frac{\pi}{2}$ and $\tau = 50$. $\omega_0 \approx 0.2490053$ is chosen as an offset. The widths $w(A = \frac{\pi}{4}) = 2.66 \times 10^{-4}$ and $w(A = 4) = 1.06 \times 10^{-3}$ are calculated. Moreover, $A_{\text{hill}} \approx 2.57$ is found.

bifurcation, the borders of the Arnold tongue are displayed via the branches of the fold bifurcations.

The shape of the Arnold tongue of the 1-kink-solutions fits very well to the branches continued for the 2-kink-solutions. To supports that point the branches of the fold bifurcations of the 1-kink-solutions are added to fig. 4.30 in fig. 4.32. This shows the assumption that the 1-kink-solutions of the period $T = T_\varphi \approx \frac{1}{2}\tau$ correspond to the obtained 2-kink-solutions of the period $T = 2T_\varphi \approx \tau$. Nevertheless, the continuation of 2-kink-solutions is a more general approach because it might lead to solutions where the phase differs between the two halves after a period doubling bifurcation. Such a solution cannot be obtained using 1-kink-solutions of the period $T = T_\varphi \approx \frac{1}{2}\tau$. The continuation of period-2 solutions after period doubling bifurcations might be a starting point for a further investigation of this topic.

All in all, the behavior of the 1-kink-solutions of period $T = T_\varphi \approx \tau$ is adapted by the 2-kink-solution of period $T = 2T_\varphi \approx \tau$. Those results fit to the stable periodic background of the multiple kink solution which is observed in [Gar+17]. N of the $N + 1$ kinks are trapped in one of the N minima of the potential. This suggests that the results of the 1-kink-solutions inside a periodic potential with one minima may be extended to N-kink-solutions inside a potential with N minima. Nevertheless, the computational cost to calculate the obtained results for solutions containing more kinks exceeds the capacity of this thesis.

5. Conclusions and Outlook

The investigation of the interactions of the LSs shows, that it is well described by the model of the EOM. The determination of the values $F_{\pm}$ through a fit of the derivative of the difference between the kinks of some, specifically selected, DNSs of the DAE improved the output obtained by DNSs of the EOM significantly compared to the results obtained through calculating $F_{\pm}$ via analytics from a solution which contains one kink, as performed in [Mun19] and [MJG20]. It is illustrated, that an assumption made in [MJG20] about the connection of a periodic solution containing one LS and two LSs is not valid for the investigated parameter set. However, this assumption is crucial for the determination of $F_{\pm}$ via analytics. Hence, the presented method to determine $F_{\pm}$ through a fit has advantages for parameter sets where periodic solutions containing two kinks do not consist of a superposition of two identical periodic solutions containing one LSs. The comparison of DNSs from the EOM to the DAE illustrates that the evolution of the distance between the LSs is well described by the DNSs of the EOM, especially for greater distances. However, a qualitatively good agreement between both kinds of simulations is also observed for smaller distances. It is found analytically, that a distance of half the period between two LSs is a distance which remains constant over round trips. Moreover, it is shown numerically, through DNSs and continuations, that this kind of solutions, in fact, exist for different values of the delay time and that they are stable in general, except if a stable solution exists with a slightly smaller distance between the kinks. In this case, they are unstable. Additionally, several branches with a constant distance between the LSs with respect to a change in the delay time are found. The difference between the kinks in these branches is well separated and smaller than half the period.

Adding a periodic potential to the DAE leads to two different kinds of solutions for the LS on a stable background. The LS is either moving from a potential minimum to the next or is trapped inside the potential and therefore synchronized with it. The borders of the phenomena of synchronization in the amplitude-frequency-plane form a not symmetrical Arnold tongue which is getting wider in the frequency for an increasing amplitude. Two solutions with different positions of the LS with respect to the potential coexist for each parameter set inside the tongue. In general, one solution is stable and the other one is unstable. Some parameter sets are found where the stable region inside the tongue is restricted by a supercritical period doubling bifurcation. The position of this bifurcation in the amplitude-frequency-plane can be controlled by the parameters for the detuning and the feedback strength. Also depending on these parameters, the Arnold tongue is opening up at higher frequencies to a relatively huge region of synchronization compared to the interval in the frequency of the tongue. Especially the period doubling bifurcation might also be observable in experiments since the obtained dependencies strongly support the existence of parameter sets which show the phenomena and which lie in the low amplitude region that might be obtainable in experiments. The

position of the kink inside the potential depends on the frequency. These results may be adapted to solutions containing multiple LSs, which fits to the experimental data which is published so far.
Therefore, the position and periodicity of the LS and the stability of the solutions may be controlled by the additional periodic potential. These properties are essential for applications in optical communication networks.
The presented method to determine $F_{\pm}$ through a fit of the derivative of the distance between the LSs obtained from the dynamics of the DAE need to be evaluated at other parameter sets. Moreover, a robust and effective method could be found to determine which DNSs of the DAE are at least necessary to obtain sufficient agreement between the DNSs of the EOM and the DNSs of the DAE. The EOM is investigated for periodic solutions containing two LSs only. However, the dynamics of solutions containing multiple kinks is of great interest, especially for applications in optical communication networks. Thus, the model could be investigated for periodic solutions containing more than two kinks. The final distances between the kinks, that are approached in such solutions, could be compared to the final distances obtained for solutions containing two LSs. Since it is shown that the position of the LSs can be controlled by a periodic potential through synchronization, the implementation of the periodic potential into the EOM is an interesting topic for future work as well.

References

[Adl46] R. Adler. "A Study of Locking Phenomena in Oscillators." In: *Proceedings of the IRE* 34.6 (1946), pp. 351–357. DOI: 10.1109/JRPROC.1946.229930.

[AG12] Eugene L. Allgower and Kurt Georg. *Numerical continuation methods: an introduction*. Vol. 13. Springer Science & Business Media, 2012. URL: https://link.springer.com/book/10.1007%2F978-3-642-61257-2.

[Bos16] Maikel M. Bosschaert. "Switching from codimension 2 bifurcations of equilibria in delay differential equations." MA thesis. 2016. URL: http://dspace.library.uu.nl/handle/1874/334792.

[Cam+16] P. Camelin, J. Javaloyes, M. Marconi, and M. Giudici. "Electrical addressing and temporal tweezing of localized pulses in passively-mode-locked semiconductor lasers." In: *Phys. Rev. A* 94 (2016), p. 063854. DOI: 10.1103/PhysRevA.94.063854.

[Cla76] Colin W. Clark. "A delayed-recruitment model of population dynamics, with an application to baleen whale populations." In: *Journal of Mathematical Biology* (1976), pp. 381–391. DOI: 10.1007/BF00275067.

[EB31] Joseph Erlanger and Edgar A. Blair. "The Irritability Changes in Nerve in Response to Subthreshold Induction Shocks, and related Phenomena including the Relatively Refractory Phase." In: *American Journal of Physiology-Legacy Content* 99.1 (1931), pp. 108–128. DOI: 10.1152/ajplegacy.1931.99.1.108.

[ELR02] K. Engelborghs, T. Luzyanina, and D. Roose. "Numerical Bifurcation Analysis of Delay Differential Equations Using DDE-BIFTOOL." In: *ACM Trans. Math. Softw.* 28.1 (2002), pp. 1–21. DOI: 10.1145/513001.513002.

[ELS01] Koen Engelborghs, Tatyana Luzyanina, and Giovanni Samaey. *DDE-Biftool v. 2.00: a Matlab package for bifurcation analysis of delay differential equations*. 2001. URL: http://www.cs.kuleuven.be/publicaties/rapporten/tw/TW330.abs.html.

[GA12] Philippe Grelu and Nail Akhmediev. "Dissipative solitons for mode-locked lasers." In: *Nature Photonics* 6 (2012), pp. 84–92. DOI: 10.1038/nphoton.2011.345.

[Gar+15] Bruno Garbin, Julien Javaloyes, Giovanna Tissoni, and Stephane Barland. "Topological solitons as addressable phase bits in a driven laser." In: *Nature Communications* 6 (2015). DOI: 10.1038/ncomms6915.

[Gar+17] B. Garbin, J. Javaloyes, G. Tissoni, and S. Barland. *Interaction mediated transport of optical localized states in a trapping potential*. 2017. arXiv: 1710.01017.

[Gur13] Svetlana V. Gurevich. "Dynamics of localized structures in reaction--diffusion systems induced by delayed feedback." In: *Phys. Rev. E* 87 (2013), p. 052922. DOI: 10.1103/PhysRevE.87.052922.

[Her13] Willy A. Hereman. *Shallow Water Waves and Solitary Waves*. 2013. arXiv: 1308.5383.

[Jan10] Sebastiaan G. Janssens. "On a normalization technique for codimension two bifurcations of equilibria of delay differential equations." MA thesis. 2010. URL: http://dspace.library.uu.nl/handle/1874/312252.

[Jau17] L. Jaurigue. *Passively Mode-Locked Semiconductor Lasers: Dynamics and Stochastic Properties in the Presence of Optical Feedback*. Springer Theses. Springer International Publishing, 2017. ISBN: 9783319588742. DOI: https://doi.org/10.1007/978-3-319-58874-2.

[Jav+16] J. Javaloyes, P. Camelin, M. Marconi, and M. Giudici. "Dynamics of Localized Structures in Systems with Broken Parity Symmetry." In: *Phys. Rev. Lett.* 116 (2016), p. 133901. DOI: 10.1103/PhysRevLett.116.133901.

[JQ13] Sun Jian-qiao and Ding Qian. *Advances in analysis and control of time-delayed dynamical systems*. World Scientific, 2013. ISBN: 978-981-4525-50-3. URL: https://doi.org/10.1142/8878.

[KD20] Pankaj Kamthan and Eusebius J. Doedel. *AUTO: Software for continuation and bifurcation problems in ordinary differential equations*. 2020. URL: http://cmvl.cs.concordia.ca/auto/.

[Kos+18] B. Kostet, M. Tlidi, F. Tabbert, T. Frohoff-Hülsmann, S. V. Gurevich, E. Averlant, R. Rojas, G. Sonnino, and K. Panajotov. "Stationary localized structures and the effect of the delayed feedback in the Brusselator model." In: *Philosophical Transactions of the Royal Society A: Mathematical, Physical and Engineering Sciences* 376.2135 (2018), p. 20170385. DOI: 10.1098/rsta.2017.0385.

[Kur75] Yoshiki Kuramoto. "Self-entrainment of a population of coupled non-linear oscillators." In: *International Symposium on Mathematical Problems in Theoretical Physics*. Ed. by Huzihiro Araki. Springer Berlin Heidelberg, 1975, pp. 420–422. ISBN: 978-3-540-37509-8. URL: https://link.springer.com/chapter/10.1007%2FBFb0013365.

[Lan73] Oscar E. Lanford. "Bifurcation of periodic solutions into invariant tori: The work of Ruelle and Takens." In: *Nonlinear Problems in the Physical Sciences and Biology*. Ed. by Ivar Stakgold, Daniel D. Joseph, and David H. Sattinger. Springer Berlin Heidelberg, 1973, pp. 159–192. ISBN: 978-3-540-38558-5. DOI: https://doi.org/10.1007/BFb0060566.

[Lep04] Teemu Leppänen. "Computational studies of pattern formation in Turing systems." PhD thesis. 2004, p. 125. ISBN: 951-22-7396-9. URL: http://urn.fi/urn:nbn:fi:tkk-004480.

[Mar18] Jared Maruskin. *Dynamical Systems and Geometric Mechanics*. De Gruyter, 2018. ISBN: 978-3-11-059780-6. DOI: https://doi.org/10.1515/9783110597806.

[Mer+04] Ehud Meron, Erez Gilad, Jost von Hardenberg, Moshe Shachak, and Yair Zarmi. "Vegetation patterns along a rainfall gradient." In: *Chaos, Solitons & Fractals* 19.2 (2004). Fractals in Geophysics, pp. 367–376. ISSN: 0960-0779. DOI: https://doi.org/10.1016/S0960-0779(03)00049-3.

[MJG20] Leon Munsberg, Julien Javaloyes, and Svetlana V. Gurevich. *Topological Localized states in the time delayed Adler model: Bifurcation analysis and interaction law*. 2020. arXiv: 2001.07556.

[Mun19] Leon Munsberg. "Topological Localized States in Excitable Delayed Systems." MA thesis. Westfälische Wilhelms-Universität Münster, 2019.

[Nie+92] F.-J. Niedernostheide, M. Arps, R. Dohmen, H. Willebrand, and H.-G. Purwins. "Spatial and Spatio-Temporal Patterns in pnpn Semiconductor Devices." In: *physica status solidi (b)* 172.1 (1992), pp. 249–266. DOI: 10.1002/pssb.2221720123.

[OM15] Henrique M. Oliveira and Luís V. Melo. "Huygens synchronization of two clocks." In: *Scientific Reports* (2015). DOI: 10.1038/srep11548.

[OP88] Gian-Luca Oppo and Antonio Politi. "Methods of Adiabatic Elimination of Variables in Simple Laser Models." In: *Instabilities and Chaos in Quantum Optics II*. Ed. by N. B. Abraham, F. T. Arecchi, and L. A. Lugiato. Springer US, 1988, pp. 363–373. ISBN: 978-1-4899-2548-0. DOI: 10.1007/978-1-4899-2548-0_23.

[Pin18] David Pines. *Elementary excitations in solids*. CRC Press, 2018. ISBN: 9780738201153. URL: https://www.routledge.com/Elementary-Excitations-In-Solids/Pines/p/book/9780738201153.

[PRK01] Arkadij Pikovskij, Michael Rosenblum, and Jürgen Kurths. *Synchronization*. Cambridge : Cambridge Univ. Pr., 2001, XIX, 411 S. Ill., graph. Darst. ISBN: 0-521-59285-2.

[Rom+16] Bruno Romeira, R. Avó, José ML Figueiredo, S. Barland, and Julien Javaloyes. "Regenerative memory in time-delayed neuromorphic photonic resonators." In: *Scientific reports* 6 (2016), p. 19510. DOI: https://doi.org/10.1038/srep19510.

[Sei+20] Thomas G. Seidel, Auro M. Perego, Julien Javaloyes, and Svetlana V. Gurevich. "Discrete light bullets in passively mode-locked semiconductor lasers." In: *Chaos: An Interdisciplinary Journal of Nonlinear Science* 30.6 (2020), p. 063102. DOI: 10.1063/5.0002989.

[Sie+14] Jan Sieber, Koen Engelborghs, Tatyana Luzyanina, Giovanni Samaey, and Dirk Roose. *DDE-Biftool Manual - Bifurcation analysis of delay differential equations*. 2014. arXiv: 1406.7144.

[Str07] S.H. Strogatz. *Nonlinear Dynamics And Chaos*. Studies in nonlinearity. Sarat Book House, 2007. ISBN: 9788187169857.

[The20] The-SciPy-community. *SciPy.org: Integrator for an ODE*. 2020. URL: https://docs.scipy.org/doc/scipy/reference/generated/scipy.integrate.odeint.html#scipy.integrate.odeint.

[Tol20] Vladimir A. Tolstykh. *Partial Differential Equations*. De Gruyter, 2020. ISBN: 978-3-11-067725-6. DOI: https://doi.org/10.1515/9783110677256.

[UWR12] Hannes Uecker, Daniel Wetzel, and Jens D. M. Rademacher. *pde2path - A Matlab package for continuation and bifurcation in 2D elliptic systems*. 2012. arXiv: 1208.3112.

[VT05] Andrei G. Vladimirov and Dmitry Turaev. "Model for passive mode locking in semiconductor lasers." In: *Phys. Rev. A* 72 (2005), p. 033808. DOI: 10.1103/PhysRevA.72.033808.

[Wag14] BI Wage. "Normal form computations for delay differential equations in DDE-BIFTOOL." MA thesis. 2014. URL: http://dspace.library.uu.nl/handle/1874/296912.

[YNU10] Sun Yi, Patrick W. Nelson, and A. Galip Ulsoy. *Time-delay systems: analysis and control using the Lambert W function*. World Scientific, 2010. ISBN: 9789814307406. URL: https://ebookcentral.proquest.com/lib/ulbmuenster/detail.action?docID=731111.

[ZA14] D. H. Zanette and S. I. Arroyo. "Synchronization of a forced self-sustained Duffing oscillator." In: *The European Physical Journal Special Topics* 223 (2014), pp. 2807–2817. DOI: 10.1140/epjst/e2014-02294-7.

A. Appendix

A.1. DNS – SIMP Scheme

A semi-implicit (SIMP) scheme of second order is used for the DNSs in this research. Hence, a detailed overview of this topic is provided. The goal is to simulate the dynamics given by eq. (2.11) with an additional noise term $\epsilon(t)$

$$\frac{dz(t)}{dt} = f\left(z(t), z_\tau(t), t\right) + \epsilon(t) \quad \text{where} \quad z_\tau(t) = z(t-\tau). \tag{A.1}$$

Therefore, the continuous dynamic is discretized in time steps of length Δt. The integration of eq. (A.1) of one time step from t_0 to $t_0 + \Delta t$ is given by

$$\int_{t_0}^{t_0+\Delta t} \frac{dz(t)}{dt} dt = z(t_0+\Delta t) - z(t_0) = I + dW \quad \text{where} \tag{A.2}$$

$$I = \int_{t_0}^{t_0+\Delta t} f\left(z(t), z_\tau(t), t\right) dt \quad \text{and} \tag{A.3}$$

$$dW = \int_{t_0}^{t_0+\Delta t} \epsilon(t) dt. \tag{A.4}$$

dW is called the differential of the Wigner process. For small time steps Δt, f is approximated by the Taylor expansion up to first order which is used for the calculation of

$$\begin{aligned} I \simeq & \int_{t_0}^{t_0+\Delta t} f\left(z(t_0), z_\tau(t_0), t_0\right) dt \\ & + \int_{t_0}^{t_0+\Delta t} \left.\frac{\partial f}{\partial z}\right|_{[z(t_0), z_\tau(t_0), t_0]} \left(z(t) - z(t_0)\right) dt \\ & + \int_{t_0}^{t_0+\Delta t} \left.\frac{\partial f}{\partial z_\tau}\right|_{[z(t_0), z_\tau(t_0), t_0]} \left(z_\tau(t) - z_\tau(t_0)\right) dt \\ & + \int_{t_0}^{t_0+\Delta t} \left.\frac{\partial f}{\partial t}\right|_{[z(t_0), z_\tau(t_0), t_0]} \left(t - t_0\right) dt. \end{aligned} \tag{A.5}$$

The structure

$$\int_{t_0}^{t_0+\Delta t} a\left(x(t) - x_0\right) dt = a \int_{t_0}^{t_0+\Delta t} x(t) dt - a x_0 \Delta t \tag{A.6}$$

with constants a and x_0 is identified in the first order terms. The integral of the observable $x(t)$ is approximated by the values at t_0 and $t_0 + \delta t$ with the Trapez-method $\int_{t_0}^{t_0+\Delta t} x(t) dt \simeq \int_{t_0}^{t_0+\Delta t} x(t_0) dt + \int_{t_0}^{t_0+\Delta t} \frac{x(t_0+\Delta t) - x(t_0)}{\Delta t} (t - t_0) dt$. Which leads to

$$\int_{t_0}^{t_0+\Delta t} a\left(x(t) - x_0\right) dt \simeq \frac{1}{2} a\left(x(t_0+\Delta t) - x(t_0)\right) \Delta t. \tag{A.7}$$

Inserting this result into eq. (A.5) gives

$$\begin{aligned} I \simeq & f\left(z(t_0), z_\tau(t_0), t_0\right) \Delta t \\ & + \frac{1}{2} \left.\frac{\partial f}{\partial z}\right|_{[z(t_0), z_\tau(t_0), t_0]} \left(z(t_0 + \Delta t) - z(t_0)\right) \Delta t \\ & + \frac{1}{2} \left.\frac{\partial f}{\partial z_\tau}\right|_{[z(t_0), z_\tau(t_0), t_0]} \left(z_\tau(t_0 + \Delta t) - z_\tau(t_0)\right) \Delta t \\ & + \frac{1}{2} \left.\frac{\partial f}{\partial t}\right|_{[z(t_0), z_\tau(t_0), t_0]} (t_0 + \Delta t - t_0) \, \Delta t. \end{aligned} \tag{A.8}$$

Hence, the whole integral in eq. (A.2) reads

$$\begin{aligned} & \left[z(t_0 + \Delta t) - z(t_0)\right] \left[1 - \frac{1}{2} \left.\frac{\partial f}{\partial z}\right|_{[z(t_0), z_\tau(t_0), t_0]} \Delta t\right] \\ & \quad \simeq \frac{1}{2} \Delta t \left[2 f\left(z(t_0), z_\tau(t_0), t_0\right) + \left.\frac{\partial f}{\partial z_\tau}\right|_{[z(t_0), z_\tau(t_0), t_0]} \left(z_\tau(t_0 + \Delta t) - z_\tau(t_0)\right) \right. \\ & \qquad \left. + \left.\frac{\partial f}{\partial t}\right|_{[z(t_0), z_\tau(t_0), t_0]} \Delta t + 2 \frac{dW}{\Delta t}\right]. \end{aligned} \tag{A.9}$$

Rearranging leads to the final result

$$\begin{aligned} z(t_0 + \Delta t) \simeq z(t_0) + & \left[2 f\left(z(t_0), z_\tau(t_0), t_0\right) + \left.\frac{\partial f}{\partial z_\tau}\right|_{[z(t_0), z_\tau(t_0), t_0]} \left(z_\tau(t_0 + \Delta t) - z_\tau(t_0)\right) \right. \\ & \left. + \Delta t \left.\frac{\partial f}{\partial t}\right|_{[z(t_0), z_\tau(t_0), t_0]} + 2 \frac{dW}{\Delta t}\right] \frac{\frac{1}{2} \Delta t}{1 - \frac{1}{2} \Delta t \left.\frac{\partial f}{\partial z}\right|_{[z(t_0), z_\tau(t_0), t_0]}}. \end{aligned} \tag{A.10}$$

For the DAE with periodic potential which is given in eq. (4.1),

$$f\left(\theta, \theta_\tau, t\right) = \Delta - \sin\left(\theta + A \cos\left(\omega t\right)\right) + \chi \sin\left(\theta_\tau - \theta - \psi\right), \tag{A.11}$$

$$\frac{\partial f}{\partial \theta} = -\cos\left(\theta + A \cos\left(\omega t\right)\right) - \chi \cos\left(\theta_\tau - \theta - \psi\right) \tag{A.12}$$

$$\frac{\partial f}{\partial \theta_\tau} = +\chi \cos\left(\theta_\tau - \theta - \psi\right), \tag{A.13}$$

$$\frac{\partial f}{\partial t} = A \omega \sin\left(\omega t\right) \cos\left(\theta + A \cos\left(\omega t\right)\right) \quad \text{and} \tag{A.14}$$

$$dW = \sqrt{\Delta t} \epsilon r \tag{A.15}$$

– where ϵ is the amplitude of the noise and $r \in [0, 1]$ is a random number – are obtained.

A.2. Declaration of Academic Integrity

Hereby, I confirm that this thesis on "Topological Localized States in a Delayed Adler Equation" is solely my own work and that I have used no sources or aids other than the ones stated. All passages in my thesis for which other sources, including electronic media, have been used, be it direct quotes or content references, have been acknowledged as such and the sources cited.

Münster, September 14, 2020

Florian Eckel

I agree to have my thesis checked in order to rule out potential similarities with other works and to have my thesis stored in a database for this purpose.

Münster, September 14, 2020

Florian Eckel